Impact response of a continuous fibre reinforced thermoplastic from a soft bodied projectile
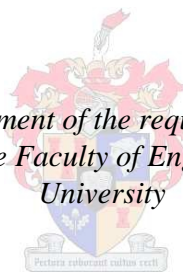
by
Arthö Otto van der Westhuizen

Thesis presented in fulfilment of the requirements for the degree of Master of Science in the Faculty of Engineering at Stellenbosch University

Supervisor: Prof Gerhard Venter

March 2013

Declaration

By submitting this thesis electronically, I declare that the entirety of the work contained therein is my own, original work, that I am the sole author thereof (save to the extent explicitly otherwise stated), that reproduction and publication thereof by Stellenbosch University will not infringe any third party rights and that I have not previously in its entirety or in part submitted it for obtaining any qualification.

Date: ....

Opsomming

Saamgestelde materiale het baie gewilde materiale in die lugvaart- en motor industrië geword as gevolg van die gewigsbesparende voordele wat dit inhou. Kostes en ander verwerkingsprobleme het tradisioneel die wydverspreide gebruik van spesifiek termoplasties-versterkte vesels in hierdie areas verhinder. Baie van die vervaardigingsprobleme (spesifiek lang siklusse) is aangespreek met die aanvang van termoplastiese matriks materiaal soos Polyphenolien Sulfied (PPS). Hierdie materiaal voldoen ook aan die lugvaart-industrie se brand-, rook- en giftigheidstandaarde.

Termoplastiese saamgestelde materiale kan byvoorbeeld gevind word op komponente in vliegtuie se binneruimtes en ook die voorste rand van die vlerke. Hierdie komponente is hoogs vatbaar vir impakskade. Die hoë sterkte en styfheid tot gewig verhoudings van saamgestelde materiale laat toe vir dun materiaal dwarssnitte. Komponente is dus kwesbaar vir uit-vlakkige impak beladings. Saamgestelde materiale kan ook intern deur hierdie beladings beskadig word en kan nie met die blote oog waargeneem kan word nie. Dit is dus nodig om die skade weens hierdie beladings tydens normale gebruik akkuraat te voorspel. Verder sal dit nuttig wees om die struktuur se gedrag te bepaal in toepassings waar byvoorbeeld passasier veiligheid krities is, soos op vliegtuig ruglenings tydens noodlandings.

In hierdie studie is die potensiële vervaardigingsvoordele van termoplastiese saamgestelde materiale gedemonstreer. Daarbenewens is 'n uit-vlakkige impak deur 'n sagte liggaam herbou in 'n laboratorium omgewing. Die primêre doelwit van hierdie studie was om die impak numeries te modelleer.

Vervaardigingsvoordele van `n vesel versterkte termoplastiese laminaat is gedemonstreer deur die vervaardiging van 'n konkawe, agt laag laminaat uit 'n vooraf gekonsolideerde geweefde doek. Die totale verwerkingstyd van die plat laminaat na 'n konkawe laminaat was minder as vyf minute. 'n Eenvoudige plat laminaat en 'n konkawe laminaat is onderwerp aan 'n lae snelheid impak deur 'n sagte projektiel. Die impak is gemodelleer deur die evaluering van drie modelleringsmetodes vir die saamgestelde paneel. Die evalueringskriteria het o.a. ingesluit of laminaat se volle gedrag suksesvol gemodelleer kon word met behulp van slegs 2D dop elemente.

Die reaksie van die saamgestelde paneel en gepaardgaande faling is met wisselende vlakke van sukses deur die drie geëvalueerde modelle voorspel. Die faling van tussen-laminêre bindings (verwys na as delaminasie) kon nie deur enige van die modelle voorspel word nie. Twee van die modelle het egter in-vlak faling met redelike akkuraatheid voorspel.

Abstract

Due to weight saving advantages composite materials have become a highly popular material in the aerospace and automotive industries. Traditionally processing difficulties and costs have been a barrier to widespread composite material use in these industries. With the advent of thermoplastic matrix materials such as Polyphenoline Sulphide (PPS) the processing difficulties (especially long cycle times) experienced with traditional thermosetting resins can be addressed while maintaining aerospace Fire-Smoke and Toxicity (FST) approval.

Thermoplastic composites can for example be found on aircraft interior components and leading edges of the wings. These areas are highly susceptible to impact damage. The high strength- and stiffness to weight ratios of composites allows for thin material cross sections. This leaves the components vulnerable to out-of-plane impact loads. Composite materials may also be damaged internally by these loads, leaving the damage undetectable through visual inspections. It may therefore be necessary to predict the amount of damage a component would sustain during normal operation. Additionally, it would be useful to predict structural response of these materials in applications where passenger safety is crucial, such as aircraft seat backrests during emergency landings.

In this study the potential processing benefits of thermoplastic composite materials were demonstrated. Additionally an out-of-plane impact from a soft bodied projectile was reconstructed in a laboratory environment. The primary objective was to numerically model the impact event.

Processing benefits of thermoplastics were demonstrated by producing a single curvature eight layered laminate from a pre-consolidated woven sheet. The total processing time from flat panel to a single curvature panel was below five minutes. A simple flat laminate and a single curvature laminate were subjected to a low velocity drop weight impact load from a soft bodied projectile. These impact events were modelled by evaluating three modelling methods for the composite panel structural response and damage evolution. Part of the evaluation criteria included whether laminate failure could be modelled successfully using only 2D shell elements.

The response of the composite panel and accompanying failure were predicted with varying levels of success by the three evaluated models. The failure of inter-laminar bonds (referred to as delamination) could not be predicted by either model. However two of the models predicted in-plane failure with reasonable accuracy.

Acknowledgements

I would like to express my gratitude towards Kjelt van Rijswijk, Aerosud, Caroline Silberbauer and the AMTS for their part in the thermoforming process.

Special thanks to Harm Albers from TenCate for the material provided.

Further, to Prof Gerhard Venter and Mr Kobus van der Westhuizen for their inputs.

Ferdi Zietsman and Martin Venter, who always had time for a cup of coffee.

Calvin Hammerse for cutting who knows how many composite samples.

Finally, but most importantly, to my parents without whom none of this would be possible.

Table of Contents

List of Tables

List of Figures

Chapter 1 Introduction

Composite materials have become more popular over the years. Composites offer many advantages over traditional metallic materials due to their attractive stiffness to weight ratios.   The aerospace and automotive industries are popular applications of these materials where fuel savings and performance benefits may be gained from using composite materials.   Manufacturers are under ever increasing pressure from emission regulations and the possible weight savings from composites are an attractive solution. As composites become cheaper to produce, the material will be used in more mainstream products where it was once reserved only for high performance applications. The automotive industry is a prime example of this.

In the past, production of composites has been very expensive and labour intensive.   Traditional thermosetting composites often required hand layup, followed by a baking process under vacuum in an autoclave. Once a component is cured it cannot be reformed by melting, and recycling of the material is limited to chopping the spent parts into pieces and using the shards for chopped strand composites.

Attempts have been made at using thermoplastics as matrix materials but in early years the application of the materials were limited by factors such as low elastic modulus, low softening temperatures and poor fibre/resin bond properties. To manufacture components from these materials however was an attractive proposition. Thermoplastic composites may be produced in large sheets/rolls and reformed by melting the matrix material and allowing sufficient pressure over a mould while allowing the composite to cool down.   Thermoplastics have indefinite shelf lives and can be re-processed to correct flaws. These advantages meant that processing times could be made much shorter and potential savings as autoclave ovens would no longer be needed.

Thermoplastic matrix materials only became a viable alternative in the last 15 years with the availability of thermoplastics such as PPS (Polyphenylene Sulfide), PEI (Polyethelineimine) and PEEK (Polyether ether ketone).   These thermoplastics addressed the previous limitations mentioned above that prohibited their use in advanced materials. Secondary benefits include excellent fire-smoke-toxicity characteristics, decreased moisture absorption, high toughness and high temperature resistance. These factors assured their use in especially the aerospace industry and are used extensively in new aircraft such as the A380 and 787 Dreamliner.

A major concern for any material used in the aerospace industry is its response to impact loads. Aircraft strike birds and other debris on runways and even during manufacture surfaces may be susceptible to tools or other foreign objects dropped

1

thereon. Aircraft interiors also take a fair amount of abuse (although impacts tend to be of low velocities), with catering trolleys for example and during emergency landings. Composites may damage internally and load bearing strength may be significantly reduced without any detectable signs on the outer surfaces of the laminate. [1]

Standard drop tests exist wherein a coupon sized laminate is subjected to a drop test load, but coupon sized laminates may behave quite differently to an entire structure when subjected to an impact load. Many impact tests use a small diameter metallic striker, targeting local effects in the material. The brittle nature of composite fibres render it susceptible to such impacts where a soft body could possibly be more representative of an actual load condition and allow greater energy absorption when engaging more material. [1]

One solution to define the structural survivability would be a rigorous structural testing program. Although this is possible, a reliable numerical approach is preferred from which to draw conclusions. The initial time investment of producing a numerical model is worthwhile the financial benefit of not having to do destructive testing on full size components. Reliable numerical models further allow for more in depth investigation as much more information on the load case is available to the engineer from which to draw conclusions. In order to assess the reliability of the models, the process should be applied and validated with simple geometries first. Once the model accuracy and surety of the model parameters have developed to a satisfactory level, the process may be applied to full scale problems (or approximations thereof).

Composite materials present a greater challenge than common metallic materials when numerical modelling is considered. When failure is considered, fibre failure, matrix failure and the failure of bonds between fibres and matrix components are possible. [2] Furthermore, composites commonly require a two way treatment of failure strength for each material direction, as compression strength is typically lower than tensile strength due to fibre buckling.

Delamination (the failure of inter-laminar bonds) of composites is also of particular concern and some promising methods to model this 3D phenomenon with 2D shell elements have emerged and will be investigated. Traditionally it was believed that delamination could only be predicted by models using solid (3D) elements as delamination is an out-of-plane failure mode. However, modelling entire components with solid elements can become computationally expensive and therefore the desire to capture all failure modes of laminates using only shell elements which are less expensive computationally. [3]

The long term goal of this research would be to successfully model the full response (including failure) of these advanced materials using shell elements (while taking account of their complexities) and using the visualization advantages of numerical modelling to enhance future products. Passenger head impacts on seat backs during emergency landings is an example of such an

application where target stiffness and failure are critical and where numerical models can (and have to advanced users) provide great aid. This project will serve as in introductory step to achieving such a goal.

In short, the project aims:

- To subject a thermoplastic composite material (selected appropriate to aircraft interiors) to a low speed impact load from a soft bodied projectile. Two geometries are to be evaluated: a simple flat panel and a single curvature laminate.
- To thermoform a single curvature panel required for impact testing.
- To evaluate methods of building a numerical model simulating the impact load with the aim to successfully model the flat laminate and then the single curvature laminate.
- Compare the models to the physical impact test.
- Evaluate the suitability of relying on 2D shell elements for both in-plane and delamination failure of composite materials.

Chapter 2 Background Information

2.1. Thermoplastic composites

Fibre reinforced composites are anisotropic by nature. This is caused by the differing strengths of the matrix material and the geometry of the fibre that reinforces it. The fibre is stiffer than the matrix material and therefore the material is stiffer in the fibre direction (warp direction) and less in the weft direction (orthogonal to the warp direction). This allows for material to be oriented in load carrying directions only, further reducing weight by decreasing the amount of excess material which does not contribute to the strength of the part.

A composite material may refer to any material which consists of more than one material. For this research composites where a polymer material is reinforced by a fibre material will be considered. Polymers may be reinforced by either chopped fibres or continuous fibres as in the case considered in this thesis document. Continuous fibres differ from chopped fibres as its name suggests: The fibre is continuous throughout the part geometry.

The polymer is referred to as the matrix material. These may be thermosetting (thermosets) or thermoplastic polymers. It is generally accepted that the role of the matrix material is to transmit loads to the fibres which reinforce it. Traditionally thermosetting matrix materials dominated the composite industry, especially in structural applications. In those early years factors such as low elastic modulus, low softening temperatures and poor fibre/resin bond properties limited the applications for thermoplastic materials.

Thermosets are produced by a non reversible chemical reaction where the matrix and hardener/catalyst is heated and allowed to cure above a curing temperature after which it is cooled to deliver a solid part. Prior to cure, thermosets are low viscosity, low molecular weight semi solids. During cure, molecular weight and viscosity of the polymer increases as covalent cross-link bonds build between polymer chains. [4]

Thermoplastics on the other hand are fully reacted high molecular weight polymers prior to processing. Herein lies the potential for faster processing times when using thermoplastic polymers as matrix material, as no time is required for the chemical reaction to complete during the curing process.

The molecular structure of a thermoplastic material differs from those of thermosets, and thus the reason for the difference in behaviour during the manufacturing process. The variations in molecular structure may be stated in simple terms as follows: Thermosets form cross-links between polymer chains

during processing whereas thermoplastic polymer chains remain unlinked. This is also why thermoplastics melt upon reheating and thermosets do not.

Careful consideration must be given to the manufacturing process of a thermoplastic composite. Thermoplastic resins are of higher viscosity than thermosets and thus require higher pressures during processing. Additionally processing temperatures for thermoplastics are higher than for thermosets which causes difficulty in finding vacuum bags that can sustain the higher processing temperatures. If the part geometry allows, using a pressing operation is more attractive than vacuum forming for this reason. [4]

Semicrystaline thermoplastics such as Polyether ether ketone (PEEK) and Polyphenolyne Sulfide (PPS) offer attractive Fire-Smoke-Toxicity characteristics which are of paramount importance to the aerospace industry. Manufacturers such as Airbus, Boeing and Fokker Aerospace are developing the materials for use as full structural components such as wing assemblies. [5] The molecular structure of thermoplastics also deliver a material that is more impact resistant and damage tolerant when compared to thermosets, although this is true to a lesser degree due to toughening techniques applied to thermosets in recent years. Thermoplastics can also be used in higher temperature environments than thermosets. PPS and PEEK may also be used in load carrying conditions for extended periods above their glass transition temperatures (T_g) without creep. The glass transition temperature (T_g) is the temperature at which the semi crystalline material starts to transform from a relatively brittle state to a flexible molten state. [4]

Thermoplastics may be reprocessed by melting after cure by simply reheating to above the melting temperature, in contrast to thermosets where the curing process is irreversible. This allows for significant advantages in joining operations. Thermoplastics are also in theory fully recyclable, as the matrix may be melted and reused in other applications. Thermosets can only be ground and used as filler material after decommissioning greatly reducing the value of the material. The reprocessing of thermoplastics also allow for the correction of faulty parts, thus reducing the amount of waste material in production.

Since thermoplastics are fully reacted prior to cure prepregs are stiff and not easily drapeable (prepregs are typically used in vacuum forming operations for complicated part geometries). This issue has been remedied by the introduction of commingled material. In this case sheets of material are used where the thermoplastic matrix fibres and reinforcement fibres are mixed at strand level. This greatly increases the drapeability of the thermoplastic material.

Raw material costs for thermoplastics are higher than those of thermosets, but this can be offset by reduced processing costs. Due to the absence of chemical reactions during processing thermoplastics require elevated temperatures for substantially less time than thermosets. Although the temperatures are higher in the case of thermoplastics cure time is in the matter of minutes, not hours.

Thermoplastics may also be heated, formed and cooled rapidly for the same reason, reducing the need for autoclaves, reducing capital costs and increasing available floor space. [4]

2.2. Composite materials: Constitutive model

Physical properties of composites are orthotropic (orthogonally anisotropic). This means that the material has varying stiffness depending on loading direction. Carbon composites are generally defined with stiffness in warp and weft directions. Warp direction usually denotes the $0°$ axis and the weft direction perpendicular to the primary fibre direction. For unidirectional (UD) lamina warp and weft direction properties will vary significantly, but less so in the case of woven fabric lamina or plies (as used in this research).

Three dimensional stresses can be related to strains by using Hooke's law:

$$\boldsymbol{\sigma} = \boldsymbol{C}\boldsymbol{\epsilon} \qquad\qquad 1$$

$$
\begin{bmatrix} \sigma_1 \\ \sigma_2 \\ \sigma_3 \\ \tau_{23} \\ \tau_{31} \\ \tau_{12} \end{bmatrix} =
\begin{bmatrix}
C_{11} & C_{12} & C_{16} & C_{14} & C_{15} & C_{16} \\
C_{12} & C_{22} & C_{26} & C_{24} & C_{25} & C_{26} \\
C_{16} & C_{16} & C_{66} & C_{34} & C_{35} & C_{36} \\
C_{41} & C_{42} & C_{43} & C_{44} & C_{45} & C_{16} \\
C_{51} & C_{52} & C_{53} & C_{45} & C_{55} & C_{56} \\
C_{61} & C_{62} & C_{63} & C_{46} & C_{65} & C_{66}
\end{bmatrix}
\begin{bmatrix} \varepsilon_1 \\ \varepsilon_2 \\ \varepsilon_3 \\ \gamma_{23} \\ \gamma_{31} \\ \gamma_{12} \end{bmatrix} \qquad\qquad 2
$$

Where $\boldsymbol{C}$ is called the elasticity tensor, $\boldsymbol{\epsilon}$ contains the strain components (ε and γ) and $\boldsymbol{\sigma}$ contains the stress components (σ and τ). Since the lamina tends to be very thin (0.31 mm in the case of this thesis) a plane stress condition is assumed (leaving $\sigma_3 = 0$, $\tau_{23} = 0$ and $\tau_{31} = 0$). Additionally, for orthotropic materials, the relation can further be reduced to (including the plane stress assumption):

$$
\begin{bmatrix} \sigma_{11} \\ \sigma_{22} \\ \tau_{12} \end{bmatrix} =
\begin{bmatrix}
C_{11} & C_{12} & 0 \\
C_{12} & C_{22} & 0 \\
0 & 0 & C_{66}
\end{bmatrix}
\begin{bmatrix} \varepsilon_{11} \\ \varepsilon_{22} \\ \gamma_{12} \end{bmatrix} \qquad\qquad 3
$$

It is common for composite layups to have the material axis at an angle to the principle axis of the geometry. The stiffness matrix must then be rotated to coincide with the working/principle axis. Laminates also consist of many layers of lamina, so the effect of each lamina, at its respective angle and thickness must be accounted for. [6] The result is:

$$\begin{bmatrix} N_x \\ N_y \\ N_{xy} \\ M_x \\ M_y \\ M_{xy} \end{bmatrix} = \begin{bmatrix} A_{11} & A_{12} & A_{16} & B_{11} & B_{12} & B_{16} \\ A_{12} & A_{22} & A_{26} & B_{12} & B_{22} & B_{26} \\ A_{16} & A_{16} & A_{66} & B_{16} & B_{26} & B_{66} \\ B_{11} & B_{12} & B_{16} & D_{11} & D_{12} & D_{16} \\ B_{12} & B_{22} & B_{26} & D_{12} & D_{22} & D_{26} \\ B_{16} & B_{26} & B_{66} & D_{16} & D_{26} & D_{66} \end{bmatrix} \begin{bmatrix} \varepsilon_x^0 \\ \varepsilon_y^0 \\ \gamma_{xy}^0 \\ \kappa_x \\ \kappa_y \\ \kappa_{xy} \end{bmatrix} \qquad 4$$

Where the extensional stiffness matrix *A* relates resultant in-plane forces *N* to in-plane strains, the bending stiffness matrix *D* relates the bending moments *M* to curvatures and the coupling matrix *B* relates forces and moments to the mid-plane strains and curvatures. For the full development refer to [6].

2.3.   Mechanics of fibre composites

2.3.1. Loading

During tensile loading in the fibre direction of the laminate, the load is predominantly carried by the fibres as they are significantly stiffer than the matrix material. During compressive loading fibres buckle easily and the matrix serves as a medium to bind the fibres during compressive loading. If loads are applied transverse to the fibre direction for UD laminates, a combination of the fibre and matrix properties contribute to the stiffness of the laminate. [7]

2.3.2. Damage

Matrix damage to a laminate has very little effect on the stiffness of a laminate during tensile loading in the fibre direction (for UD laminates), as most of the load is carried by the fibres. Undamaged fibres may however contribute to the damage of the matrix material during such loading conditions due to fibre straightening. [7]

Matrix cracks/damage severely affects the capability of the laminate to support compressive loads. In the fibre direction fibre buckling and kinking will contribute to further matrix damage. The bond area between the matrix material and the fibre is typically weaker than the constituents themselves and these bond areas serve as pathways for crack propagation. [7]

Matrix and fibre cracking creates difficulty in producing a material model which includes damage, as discussed by Schweizerhof, Műnz and Rottner. [8] In order to obtain a workable solution the following assumptions were made for damage capable constitutive models, and must be kept in mind by the user: [7]

- Stress-strain response obtained from test data is known to be highly non-linear. However, linear elasticity is assumed to hold if the state of defects

does not change. This implies that in the stress-strain space, the laminate will remain linear and all non-linear effects are attributed to damage.

- The effects of defects are treated as disk like cracks tangential and perpendicular to fibre directions. This has the effect of maintaining the orthotropic nature of the lamina throughout the damaging process.

2.3.3. Failure modes

Failure of composites may be broken into four modes. Mode 1 or the fibre rupturing mode is caused by tensile stress in the fibre direction σ_{11}. As stated, tensile loads in this direction is predominantly supported by the fibres. The strength X_t is therefore mostly fibre dependent and is a function of the fibre/matrix ratio in the laminate. Failure occurs when a group of closely packed fibres fail and debond from the matrix material, creating voids between the fibre ends. The matrix material may not have failed at the specific region, as they are capable of resisting higher strains than the fibre material. [7]

Mode 2 or the fibre kinking and buckling mode occurs when the laminate is subjected to a compressive load in the fibre direction σ_{11}. Mode 2 failure is accompanied by matrix fragmentation and is initiated by the buckling of a single fibre. The compressive strength X_c of the laminate is controlled not only by the compressive strength of its constituents but also by the shear strength and elastic stiffness of the matrix material. The material behaviour is linear below failure for stiff matrices but non-linear behaviour has been observed pre-failure for soft matrix materials. [7]

Modes 3 (tensile) and 4 (compressive) are observed by matrix cracking during transverse or shear loading of the laminate. Failure in this sense is typically controlled by the tensile and shear strengths of the matrix material. [7]

Delamination is a failure mode often encountered but is a property of laminate failure rather than of the lamina. Delamination is identified by separation of laminas and is an internal damage mechanism which severely compromises the strength of the laminate which may not be detectable without advanced scanning methods. [7]

2.4.   Failure criteria for composites

From the above discussions, it is apparent that more than one failure criteria has to be considered for composites. These can be categorized into in-plane failure criteria and delamination failure criteria.

2.4.1. In-plane failure

In-plane failure relates to the damage of composite fibres and matrices due to tensile and compressive loads as a result of pure in-plane loading or bending loads, and in-plane shear failures due to in-plane shear loads. Failure criteria may

be classified into two groups, those which treat all failure modes together and those that treat them separately.

Tsai-Wu [9] and Tsai-Hill [10] failure criteria fall into the first failure criteria group. They attempt to capture all failure modes in a single expression, as shown by the Tsai-Hill failure criteria in Equation 5:

$$\frac{\sigma_{11}^2}{X^2} - \frac{\sigma_{11}\sigma_{22}}{X^2} + \frac{\sigma_{22}^2}{Y^2} + \frac{\tau_{12}^2}{S^2} \geq 1 \qquad\qquad 5$$

Where:

σ_{11}, σ_{22} and τ_{12}:   The longitudinal, transverse and shear stresses

X, Y and S: The longitudinal, transverse and shear strength

The second category is made up of, for example, the maximum stress or strain criteria, the Hashin [11] and Chang and Chang [12] criteria. These propose separate failure modes for tension, compression, fibre and matrix failure (and combinations thereof). The 2D-Hashin criteria for instance, separate failure into four modes, which are described in Figure 1 and the equations 6 to 9 (for in-plane failure):
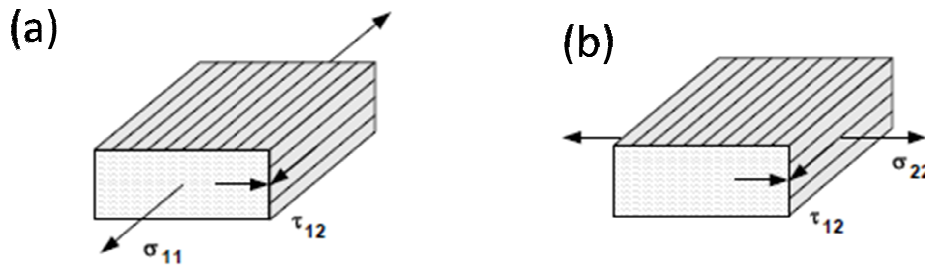
Figure 1 (a) Tensile and compressive fibre loading; (b) Tensile and compressive matrix loading

Tensile fibre failure ($\sigma_{11} > 0$)

$$\left(\frac{\sigma_{11}}{X_T}\right)^2 + \left(\frac{\tau_{12}}{S_{12}}\right)^2 = 1 \qquad\qquad 6$$

Compressive fibre failure ($\sigma_{11} < 0$)

$$\frac{|\sigma_{11}|}{X_c} = 1 \qquad\qquad 7$$

Tensile matrix failure ($\sigma_{22} > 0$)

$$\left(\frac{\sigma_{22}}{Y_T}\right)^2 + \left(\frac{\tau_{12}}{S_{12}}\right)^2 = 1 \qquad\qquad 8$$

Compressive matrix failure ($\sigma_{22} < 0$)

$$\left(\frac{\sigma_{22}}{2S_{23}}\right)^2 + \left[\left(\frac{Y_C}{2S_{23}}\right)^2 - 1\right]\frac{\sigma_{22}}{Y_c} + \left(\frac{\tau_{12}}{S_{12}}\right)^2 = 1 \qquad\qquad 9$$

The advantage of using the Hashin and Chang Chang failure theories over the original maximum stress or strain theories is that they take into consideration the inter-ply stresses and are therefore a more accurate prediction of composite strength.

2.4.2. Delamination failure

Delamination failure affects the stiffness and residual strength of a composite significantly. Several studies have been performed on this subject but the mechanisms are not yet completely understood. Energy based theories are common for delamination analysis. The Bending Strain Energy Density model [13] is based on the failure mechanism of a simply supported beam under pure bending. The normal stress term does not appear in the expression and therefore this method is convenient for two dimensional analyses.

Stress based theories are also used. The Brewer and Lagace method below (as referenced in [3]) takes into account normal and shear stresses in the laminate (Equation 11).

$$\left(\frac{\sigma_{33}}{Z_T}\right)^2 + \left(\frac{\sigma_{23}}{S_{23}}\right)^2 + \left(\frac{\sigma_{31}}{S_{31}}\right)^2 = 1 \qquad\qquad 11$$

Where σ_{31} and σ_{23} are the stresses in the 31 and 23 planes. Similarly, S_{23} and S_{31} represent the shear strengths. Z_T and σ_{33} are the strength and stress parameters in the through the thickness tensile direction for the laminate. Also, Zhang [14] used the Equations 12 and 13 to estimate the occurrence of delamination based failure.

$$\sqrt{(\tau_{13}^2 + \tau_{23}^2)} \geq Inter - laminar\ shear\ strength \qquad\qquad 12$$

$$\sigma_{peel} > Z_T \qquad\qquad 13$$

Where τ_{31} and τ_{23} are the shear stresses in the 31 and 23 directions, with σ_{peel} the peel stress. Note however how the presence of stresses in the 3 directions prohibits the easy adaption of the failure theories to two dimensional shell elements.

2.5. Finite element modelling of impact events

2.5.1. Impact damage modelling in FEA

Low to medium velocity impact damage modelling may be divided into four main categories: failure criteria approach, fracture mechanics approach, plasticity or yield surface approach and damage mechanics approach. [15]

Failure criteria approaches may be divided into two categories, one using a polynomial based failure structure such as Tsai-Wu etc., and ones separating specific damage mechanisms, referred to as progressive failure methodologies. Failure criteria approaches are however mostly restricted to static load cases. [15]

Fracture mechanics or energy based approaches are well suited to modelling the onset of matrix cracks [2] (and also delamination). Progressive failure methodologies however are not easy to implement with this technique. [2] Some proposals for modelling composite damage using plasticity theories have been proposed in [16], but these have not been widely adapted into FE codes. [2]

Damage mechanics approaches differ from fracture mechanics in that it scales the constitutive model instead of using specific cracks in the material. The damage mechanics approach was first developed by Kachanov [17] and Rabotnov [18] and was first implemented on composites by Frantziskonis [19] which has shown good results when predicting composite damage. [2]

2.5.2. Material models

LS-DYNA offers the user a myriad of choices for material models. Material models are listed in chronological order, i.e. MAT_001 being the first material model incorporated into LS-DYNA. Later (or higher number) material models are typically refined versions of earlier models. LS-DYNA in particular feature material models for composites incorporating failure criteria as discussed in the previous section, and was therefore the solver of choice. The section below briefly covers material model 54 and the evolution thereof to material model 58, some of the most recent models for composite materials.

2.5.2.1.   MAT_054-055

According to the LS-DYNA theory manual [20], these two model formulations are very close in their formulation. MAT_054 uses Chang and Chang failure criteria [12] whereas MAT_055 implements Tsai – Wu. Worthy to note from this failure criteria is the user specified parameter β, which controls the contribution of the shear strength to the Chang and Chang [12] tensile fibre failure mode as shown by Equation 14:

$$
e_f{}^2 = \left(\frac{\sigma_1}{X_t}\right)^2 + \beta\left(\frac{\tau_{12}}{S_{12}}\right) - 1 \begin{cases} \geq 0 \; failed \\ < 0 \; elastic \end{cases}
$$
14

If $\beta = 0$ the original Hashin criteria [11] is obtained for tensile fibre failure but $\beta = 1$ has been found to give superior results. The user may wish to specify strain related failure criteria, and this may be done by setting the parameters as in Table 1:

Table 1 User Specified failure parameters for MAT_054/055

Parameter	Description
DFAILT	Max strain for fibre tension
DFAILC	Max strain for fibre compression
DFAILM	Max strain for matrix
DFAILS	Max shear strain
EFFSGTRN	Effective strain

The parameters in Table 1 allows for elastic brittle or elastic plastic behaviour of the material. Figure 2 displays failure for an element in fibre tension with DFAILT set to 0 (a) and a user specified constant (b). For DFAILT the maximum stress value is maintained until a strain value as specified has been reached, after which the element fails.

The model also offers the user options to decrease the strength of an element that failed in compressive mode, or even to delete the element if the element size has a detrimental effect on the time step due to compressive deformations (and thus element size).

12
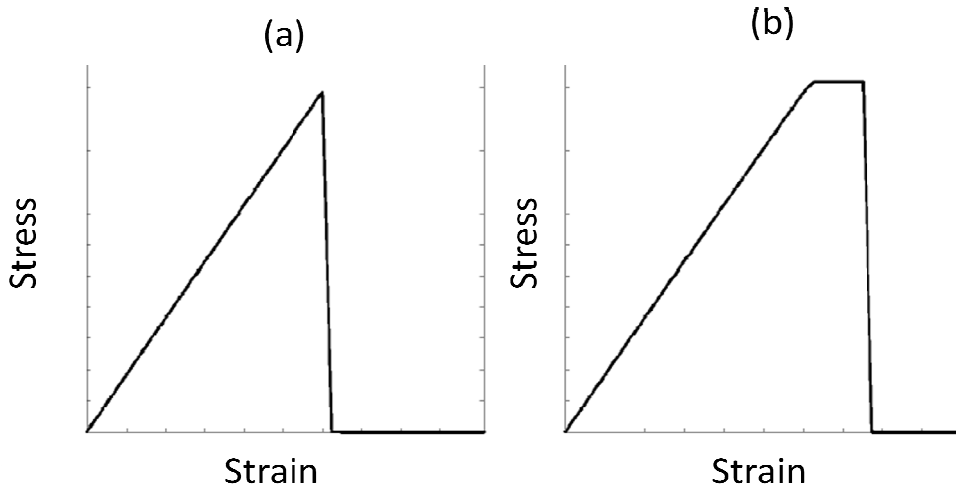
Figure 2 Elastic brittle (a) and elastic plastic (b) behaviour for MAT_054 (adapted from [8])

2.5.2.2.   MAT_058

Material model 58 will be covered in considerable detail in this section, as it was the material model of choice for this thesis. Material model 58 may be used to model composite materials with UD layers, complete laminates and woven fabrics. [20] As discussed in the previous sections, plane stress conditions are enforced for this model and therefore the model is specifically tailored for use with shell or thick shell elements.

Material model 58 uses a damage mechanics approach to model composite failure and treats damage as micro cracks introduced into the model. In order to describe how the model works a so called damage parameter must be introduced.   In classical continuum damage mechanics Kachanov stated that only undamaged areas of the material can carry load. Therefore, effective stresses $\hat{\sigma}_{ij}$ referring to the undamaged cross sectional area are considered as opposed to σ_{ij} over the total area. Effective stresses are related to true stresses by Equations 15 and 16:

$$\hat{\sigma} = M\sigma \qquad\qquad 15$$

Where: $$M = \begin{bmatrix} \dfrac{1}{1-\omega_{11}} & 0 & 0 \\[2ex] 0 & \dfrac{1}{1-\omega_{22}} & 0 \\[2ex] 0 & 0 & \dfrac{1}{1-\omega_{12}} \end{bmatrix} \qquad\qquad 16$$

Where $\omega_{i,j}$ is referred to as the damage parameter.

13

Several complications exist with such an approach, mainly the complex effect of Poisson's ratio and the change thereof due to the damage parameter $\omega_{i,j}$. A further consideration is the one sided behaviour of the physical material, i.e. damage may render the laminate useless for tensile loads, but some residual compressive strength may be maintained. Allowance for this behaviour has been made in the material model and is explained in detail by Matzenmiller et al. [7] The resulting constitutive equation (Equation 17) and allowed load range (Equation 19 and 20) for the damaged laminate which would not result in a change in damaged state is shown in the Figure 3.

$$C(\omega) = \frac{1}{D}\begin{pmatrix} (1-\omega_{11})E_1 & (1-\omega_{11})(1-\omega_{22})v_{21}E_2 & 0 \\ (1-\omega_{11})(1-\omega_{22})v_{12}E_1 & (1-\omega_{22})E_2 & 0 \\ 0 & 0 & D(1-\omega_{12})G \end{pmatrix} \quad 17$$

With

$$D = 1 - (1-\omega_{11})(1-\omega_{22})v_{12}v_{21} > 0 \qquad 18$$
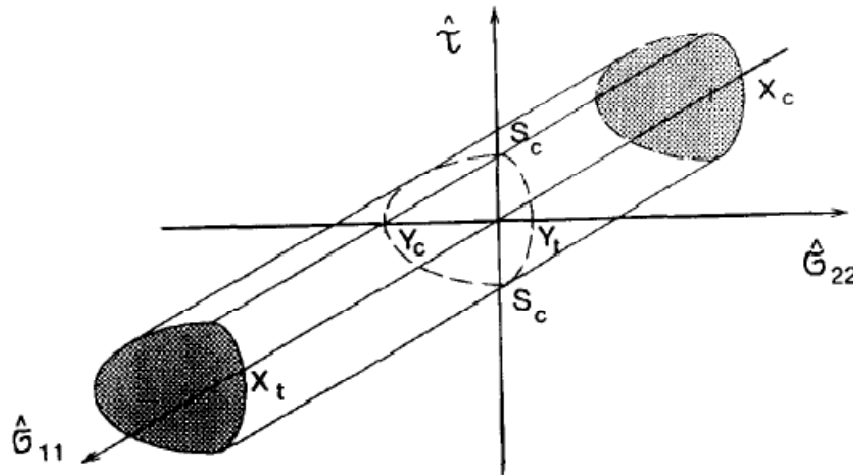
Figure 3 Load range for undamaged uni-directional fabrics in MAT_058 (from [7])

$$f_\perp = \frac{\sigma_{22}^2}{(1-\omega_{22c,t})^2 Y_{c,t}^2} + \frac{\tau^2}{(1-\omega_{12})^2 S_c^2} - r_{\perp c,t} = 0 \qquad 19$$

$$f_\| = \frac{\sigma_{11}^2}{(1-\omega_{11c,t})^2 X_{c,t}^2} - r_{\|c,t} = 0 \qquad 20$$

The f and r parameters in Equation 14 refer to the undamaged loading criteria and the threshold value of the elastic space (the relation between the yield stress and plasticity) respectively. The equations above were first postulated for uni-directional (UD) lamina and therefore required adaption for laminated fabrics (as used in this research) where there is little difference between E_1 and E_2. To account for this, two material model options have been incorporated into LS-DYNA. The smooth failure surface model is the first which assumes a failure criterion in the warp direction identical to that of the weft direction. This results in a change to the failure criterion in the 11 direction, whilst the 22 direction remains unchanged (Equation 21) and Figure 4. This method was used in this research as an interaction exists between normal and shear stresses in the damage evolution.

$$f_\| = \frac{\sigma_{11}^2}{\left(1 - \omega_{11c,t}\right)^2 X_{c,t}^2} + \frac{\tau^2}{(1 - \omega_{12})^2 S_c^2} - r_{\|c,t} = 0 \qquad 21$$
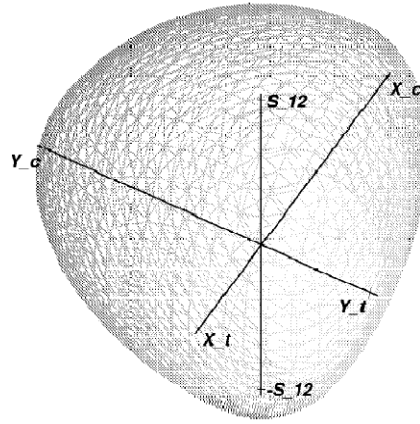
Figure 4 Undamaged stress space for smooth failure surface model MAT_058 (from [7])

The second approach decouples the failure criteria for each direction and results in the controlling relations and limits in the stress space as shown in Equation 22 – 24 and Figure 4, and may be used in an arbitrary composite.

$$f_\perp = \frac{\sigma_{22}^2}{\left(1 - \omega_{22c,t}\right)^2 Y_{c,t}^2} - r_{\perp c,t} = 0 \qquad 22$$

$$f_\| = \frac{\sigma_{11}^2}{\left(1 - \omega_{11c,t}\right)^2 X_{c,t}^2} - r_{\|c,t} = 0 \qquad 23$$

$$f_s = \frac{\tau^2}{(1 - \omega_{12})^2 X_{c,t}^2} - r_s = 0 \qquad\qquad 24$$
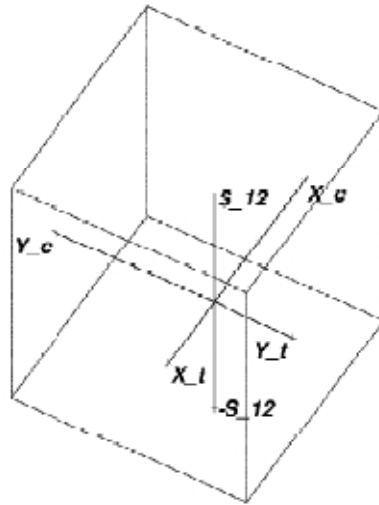
Figure 5 Stress space for uncoupled non smooth failure surface option MAT_058 (from [7])

An additional user controlled parameter is also introduced in order to reduce localization. Localization occurs when strain softening occurs once an element has reached the maximum stress value. Due to minor numerical differences between elements, some elements could potentially be unloaded while others are strained further, leading to mesh dependent solutions. To curb this, stress limiting parameters have been introduced to the model. The user specifies the minimum stress after yield, and the model will keep elements at the specified level up to failure.

The model further allows the user to account for the uncertain non-linear shear behaviour [8] of composites. The user may choose the form of a bi-linear curve for shear stress/strain behaviour as shown in Figure 6.
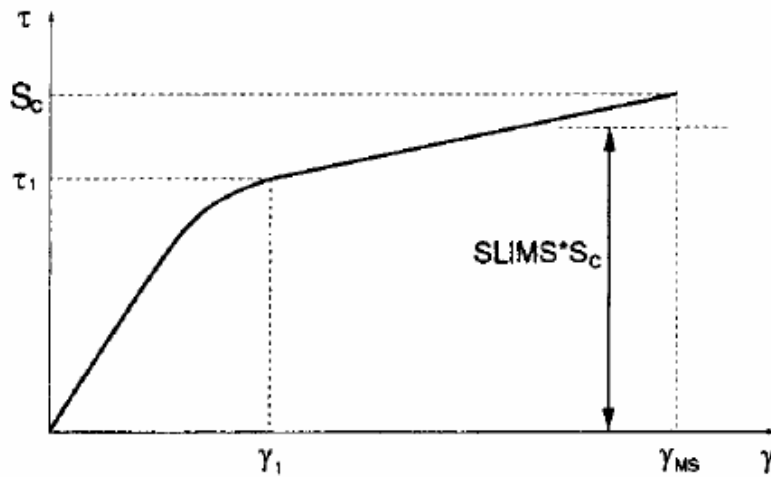
Figure 6 User defined bi linear stress strain curve for MAT_058 (from [7])

2.5.3. Modelling of multiple layers

Composites are typically used with more than a single layer in the layup. Methods for establishing a constitutive matrix for multiple layer composites are well developed. The user simply enters material parameters for single plies into the material model, specifies the material angle of each ply as well as its thickness and the constitutive equation is easily calculated. If no delamination failure is expected or if the laminate will fail under tensile loads the methods discussed above will account for failure equally well for single or multiple layer laminates. However, modelling the delamination failure of multiple layer laminates are not as simple and no single method has been identified as best. The material models above account for failure of plies within the laminate but fail to include failure due to interlaminar shear stresses.

Shell elements and the material formulations as discussed above function on plane stress assumptions. As a result, through the thickness stress components are assumed to be zero, and intuitively the reader will notice that this has an obvious negative effect when attempting to model delamination. The user is then forced to implement other methods of approximating delamination failure when using shell elements.

Three approaches have been considered in literature to capture delamination failure with shell elements. Hoof et al. [21] proposed a method by which solid elements are stacked, each layer representing a ply (Figure 7). These layers are bonded by contact definitions in the finite element code. This representation however quickly becomes computationally expensive and a natural progression of this is to use stacked shell elements. These stacked shell elements are also bonded using tied contact interfaces between plies. For both of these formulations, failure occurs when the user specified stress in the tied contact has been exceeded.

17
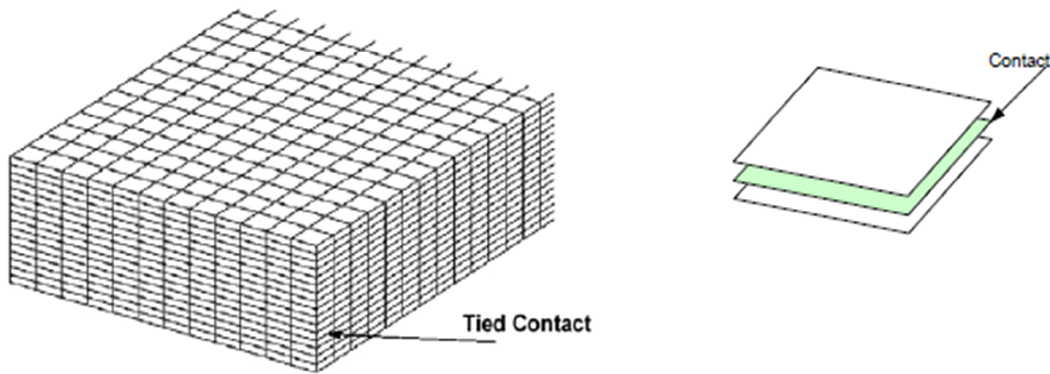
Figure 7 Stacked shell layer approach to laminate modelling [3]

A third approach has been proposed by Rajbhandari et al. [3] (from here onwards referred to as the resin model) wherein the laminate is modelled by a single layer of shell elements, but integration points have been added to the resin rich layers in between each ply (Figure 8). Delamination is achieved when the shear stress in the resin rich layers exceed that of the shear stress of the resin material. This approach serves to decrease the cost involved in computing the stacked solid and shell element techniques.
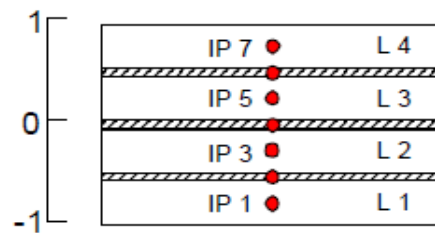
Figure 8 Laminate modelling as proposed by Rajbhandari et al. ([3]). In the image a 4 layered composite is shown with integration points for each composite layer (IP 1, 3, 5, 7) and resin layer in between.

2.5.4. Contact algorithms

LS-DYNA's capability of treating sliding contact and impact through contact algorithms has been one of its most important features [20]. Contact can include rigid or flexible bodies, edge to edge contact on shell elements and tied contacts may also be defined. Applications for these algorithms include:

- Vehicle accident and occupant safety simulation (including self contact during crumbling)
- Aircraft bird strike simulation
- Manufacturing processes such as hydro forming, metal stamping and other deep draw processes.

18

In LS-DYNA, contact entities are identified by the user. These entities are checked for contact at every computational time step. Initial penetrations are also checked before the computation starts. Contact entities may include parts which are not necessarily involved in the contact process. This allows, for example in vehicle crashworthiness simulation for all the components in the vehicle to be defined as part of a single contact entity, without the user having to know beforehand which components will contact each other.

Three distinct methods have been used to treat contact, the kinematic constraint method, the penalty method and the distributed parameter method [20]. Of these, we will mainly be concerned with the penalty method.

The penalty method places springs between penetrating nodes and the contact surface. According to the LS-DYNA theory manual [20] this method excites very little hourglassing in elements. Three implementations of the algorithm are available: The standard, the SOFT constraint and the segment based penalty formulation. The segment based formulation is designed for self contact during airbag deployment and complex contact conditions. The soft constraint penalty formulation is specifically for contact between bodies with dissimilar material properties, therefore the contact stiffness calculation and contact force update differs. This means that the standard formulation is best suited to connecting composite lamina to each other and the SOFT formulation for the contact between the projectile and the laminate.

In the standard penalty formulation interface stiffness is the same order of magnitude as the normal stiffness of the adjacent elements. A scale factor may be used to increase the contact stiffness if the user wishes to do so. The contact stiffness is determined according to Equation 25 below:

$$k_i = \frac{f_{si} K_i A_i}{\max\left(shell\ diag\right)} \qquad\qquad 25$$

Where

k_i = Interface stiffness

f_{si} = User specified scale factor (normally defaulted to 0.1)

K_i = Bulk modulus of the master surface

A_i = Interface area

max *(shell diag)* = Maximum shell diagonal distance on the master surface.

Soft materials decrease the contact stiffness and may lead to interpenetration. This can be avoided by increasing f_{si}, the interface stiffness scale factor. This however, may cause stability issues in some simulations. An alternative to this is to use the soft constraint penalty formulation. An additional stiffness calculation is performed according to Courant's criterion, which is stability based. The user activates this calculation by setting SOFT = 1 in the contact card. This contact stiffness is calculated using Equations 26 and 27.

$$k_{cs}(t) = 0.5(\text{SOFSCL})(m^*)\left(\frac{1}{\Delta t_c(t)}\right) \qquad\qquad 26$$

Where:

k_{cs} $\qquad\qquad$ = interface stiffness

m^* $\qquad\qquad$ = A function of the mass of the slave node and master nodes

Δt_c $\qquad\qquad$ = initial solution time step size.

SOFSCL $\qquad$ = User specified scale factor (default 0.1)

Then:

$$k_{SOFT = 1} = \max[k_{cs}, k_{SOFT = 0}] \qquad\qquad 27$$

2.6. Impact testing

The applications for which composite materials are typically used render them susceptible to impact damage. Composite parts may be significantly damaged by impact without the damage necessarily being recognized as significant. Laminate layers may delaminate (a desirable energy absorbing characteristic) and in doing so significantly decrease the structural integrity of the part without the damage being necessarily obvious to the naked eye. [1]

The orthotropic and sometimes brittle nature of composite materials result in a different impact response when compared with isotropic materials (such as metals), and therefore requires a separate study. Additionally composite part cross sections are typically small making them more vulnerable to impact. [1]

In general impact scenarios may be divided into two regimes, low and high speed impacts [2]. Materials behave differently in each of these regimes, and not necessarily in an intuitive manner. Low speed impacts include impacts on aircraft interiors, the area of focus for this research. Low speed impacts are commonly simulated using drop testers and coincide to tools being dropped on surfaces and other blunt instrument impacts. High speed impacts generally refer to small objects striking the material at high velocity, such as ballistic impacts. These are commonly simulated by firing test projectiles at the material by means of a propellant such as gas [2].

The difficulty in detecting internal damage on composite structures requires a fundamental understanding of the way composite structures behave during impact. For this reason much attention has been given to the study of the behaviour of composite panels to impact events [2].

2.6.1. Impact behaviour of composite panels

Experimental results have shown than composite damage may be categorized into four modes for low energy (as in this research) impact. Each mode absorbs a different amount of energy during failure, and their exact sequence is difficult to ascertain due to the short duration of the impact event. These four modes are (as shown in Figure 9): [3]

- Hertzian contact damage (localized).
- Internal delamination due to transverse shear stress/strain.
- Matrix and fibre failure due to bending strain on the impact side of the laminate.
- Fibre and matrix failure due to tensile bending strains on the non-impact side of the target composite.
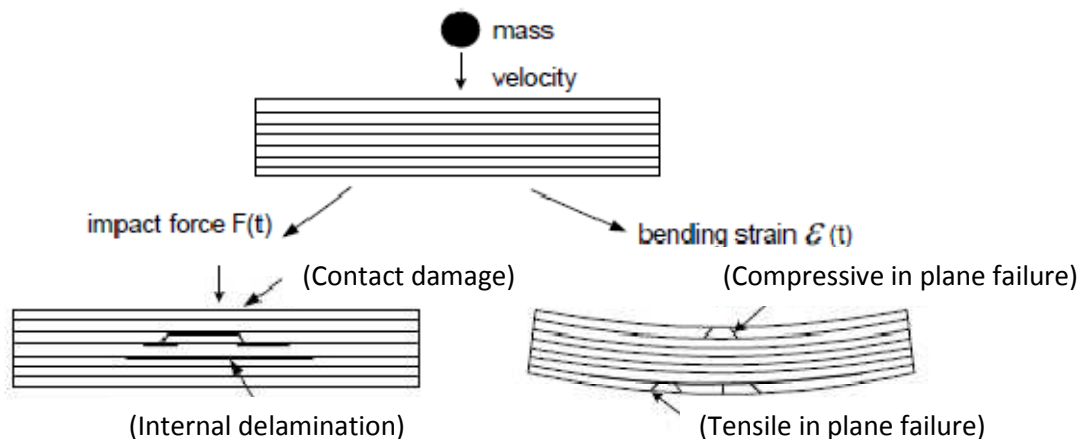

Figure 9 - Damage in composites due to out-of-plane impact (adapted from [14])

For low velocity impact, damage is initiated by matrix cracking in the laminate [4]. The damage is not caused by the compressive waves propagating back and forth through the thickness of the laminate, but instead by the physical bending displacement as a result of the impact event. In the case of thin laminates the deformation causes excessive tensile stress on the back face of the laminate causing the matrix cracks to initiate on the back surface. When considering thick laminates the shear stress at the impact location results in matrix cracking initiating at the impact face of the laminate [4].

Although the kinetic energy threshold is matrix dominated, delamination area is affected by layup and stitching. Studies have shown that no delamination occurs in UD laminates [4]. An increase of weave direction between two plies will result in an increase of interlaminar stresses leading to an increased delamination area. This may be explained by the difference in bending stiffness between laminate layers as a result of the differing fibre orientations. The variation in bending stiffness through the thickness of the laminate results in interlaminar stresses which cause delamination. Similarly the ratio of E_1/E_2 increases the delamination area in the damaged laminate, also due to variation of bending stiffness between plies.

Stitching of the laminate improves delamination resistance and decreases the delamination area for out-of-plane loads or transverse fracture with in plane loading [4]. However stitching may cause fibre damage or stress concentrations caused by resin rich pockets.

2.6.2. Factors affecting impact resistance

Projectile geometry and material have a pronounced effect on the impact result. These must be considered in addition to the kinetic energy of the projectile. [1] Heavy but slow projectiles may also posses the same kinetic energy as a high velocity lighter projectile. The projectile must be chosen so as to best represent the likely in-service impact. The Young's modulus of the projectile will have an effect on the contact stiffness of the impact and must be accounted for in contact laws. [1]

Material properties greatly affect the impact behaviour of the target laminates. The kinetic energy threshold to damage initiation is dominated by the matrix material's Young's modulus and basically independent of layup, stitching and fibre properties [4]. Properties of the fibre reinforcement only become significant at high impact energies.

In addition laminate preloads must be considered, an increase in laminate preload tends to decrease the impact energy required to total fracture. The size of the laminate must further be considered by checking transverse displacements to ensure that membrane stiffening effects did not influence the result. Thermal stresses resulting from manufacturing affect the residual stress in the laminate prior to impact and will have a significant effect on damage propagation. Thermal

stresses result for differing thermal expansion coefficients between the reinforcing fibre materials and the matrix material. [1]

Environmental effects are important to the impact performance of laminates. Temperature changes and variation in moisture content alter the material properties and in so doing also the impact behaviour of the material. [1]

2.7. Summary

This section described three methods of modelling a multi layered composite panel using shell elements. First of these (only briefly mentioned) is the standard single layer shell model. In this model formulation, the composite is modelled as a single layer of shell elements, with an integration point for each layer in the composite.   The second approach builds on the first by adding additional integration points in between the lamina for the resin material in an attempt to capture delamination events. The final method involves modelling each lamina as a separate layer of shell elements and connecting these layers by means of a contact algorithm. All three methods will be evaluated in sections to follow.

Mat_058 was selected as the material model for this study because of the advanced and progressive failure modelling of the composite material. Contact algorithms were also briefly discussed. From the discussion it is quite clear that the standard formulation of contact will be used for the inter laminar bonding whereas the SOFT formulation should be investigated for use in contact between the projectile and the laminate if stability issues at this contact interface are encountered.

For the physical impact test it was decided that a drop weight tester should be used for the low velocity impact case studied in this thesis.

Chapter 3 Impact test setup

As discussed, a composite laminate target was subjected to a low speed impact load delivered by a soft bodied projectile. This section deals with the setup of the impact test and instrumentation.

Traditionally three types of setup are considered for low speed impact testing. These are drop weight testers, cantilever impactors and pendulum type testers. [1] The decision was made to make use of a drop weight tester already available in the laboratory. A new trolley was designed to run along four vertical guide rails onto the target laminate. The trolley had to fulfil the following requirements:

- Support a soft body on the underside.
- Deliver the impact load to the centre of the laminate.
- Have a minimum secondary effect on the impact event (for example through deformation or damping the movement through friction).
- Deliver a wide range of impact energies to the target.

With the above considerations in mind, the trolley was designed to be lightweight and be supported by four Vesconite (for low friction property) wheels on the outer edges of the trolley. A FE model of an initial design was built, and material was removed at low stress locations to reduce weight. The trolley was made from 3 mm mild steel plate sections, laser cut and bent into shape (Figure 11). The payload ballast was designed to be added directly above the mount location of the rubber tip (Figure 10), to minimize stresses in the trolley structure. The trolley was hoisted on its guiderails by means of an electric winch. The trolley was fixed to the winch by means of an electromagnet, and could be released at any height above the target to a 4 m limit.

Figure 10 Rubber tip below trolley centrally mounted
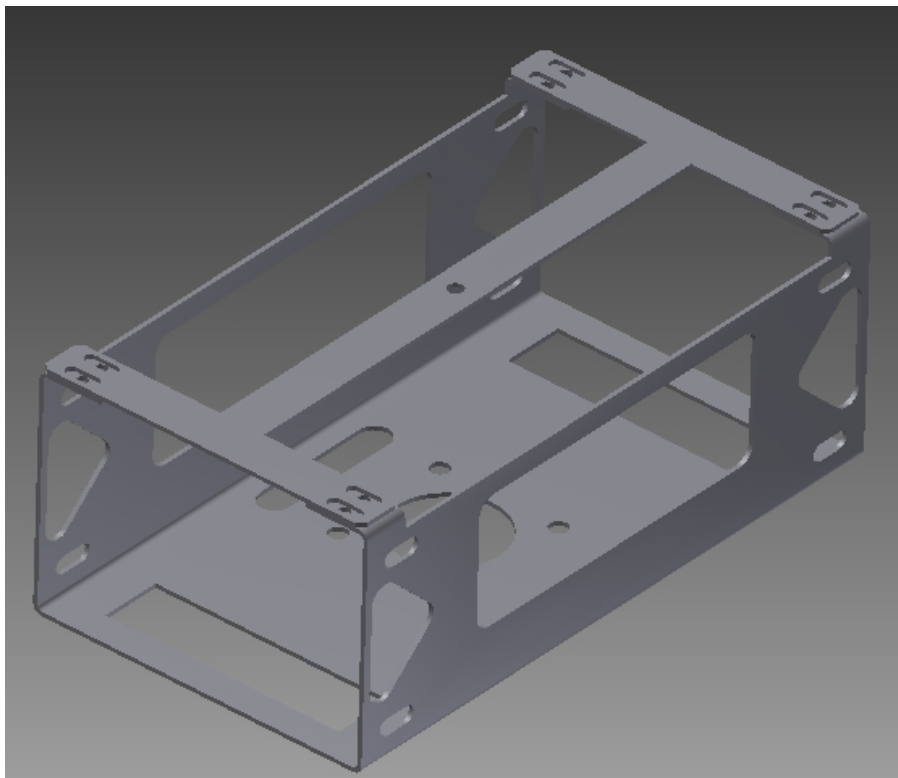
Figure 11 CAD representation of projectile trolley

The target laminate had to be supported in a manner that could be reproduced in the FE model. The support structure should have the minimum amount of uncertainty and non linearity, such as bolted connections and deformations beyond the model boundaries.

A support structure was designed using a welded frame assembly. The base of the support was a 6 mm plate with $40 \times 40 \times 3$ mm angle sections welded vertically. These angle sections lifted the mounting support of the target 60 mm from the base of the support, allowing for the bending deflection of the composite. The composite would be supported by two 10 mm flat bar sections, welded to the top of the angle sections. These flat bars were supported mid span by means of a vertical rod to assist bending stiffness (Figure 12).

The composite panel was clamped to the flat bar by means of 9 threaded bolts 30 mm apart, through a 10 mm thick steel section on the upper side. The upper steel section was designed to accept a curved panel as well. The support structure was bolted to a load cell through a $200 \times 200 \times 40$ mm steel billet, the load cell bolted to the laboratory floor. The load cell had a support radius of 200 mm, eliminating bending of the support structure to large degree.

25
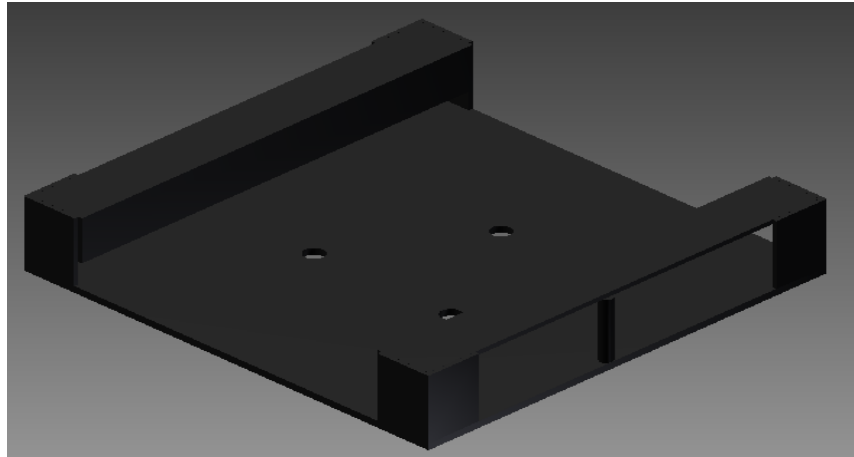
Figure 12 Composite support frame

A Quantum MX410 Data Acquisition system formed the backbone of the measurement system. Sample rate was set to 2.4 kHz, to obtain sufficient data points along the load curve.

Force measurements were made using HBM load cells. For rubber projectile characterization and initial composite panel impacts, a 10 kN S-type load cell was used. Peak loads on the composite were expected in the range of 15 – 20 kN, the decision was made to retain the 200 MN load cell even though a 20 kN load cell was available. This was done because the 200 MN load cell with its greater support radius better contained possible bending moments resulting from the impact load.

Displacement measurements were accomplished with the use of an HBM WA 100 mm LVDT (Linear Variable Differential Transducer). The LVDT was centrally mounted below the composite, extending up through the centre of the load cell and the support structure. The LVDT was attached to the centre of the composite panel with glue.

Impact velocity was measured directly before impact. Measurement was made using a proximity switch, activated by magnets on the carriage. The second magnet switches the circuit just as the PU tip touches the laminate. The switch is triggered twice during each pass, and the time to cover the distance is used to calculate the carriage velocity.

A Point Grey graphics Grasshopper high speed camera was used for visual inspection of the impact event. Maximum refresh rate of the camera was 120 Hz. The refresh rate of the camera was too slow, but still allowed for some evaluation of support structure stiffness.

Chapter 4   Rubber   impactor   modelling and testing

To review, in this thesis the behaviour of a composite material when subjected to an impact load from a soft bodied projectile is under consideration. This section deals with the analysis of the soft bodied projectile.

4.1. Material selection and properties

Traditionally, composite impact tests are performed with hard penetrator tips to determine delamination energy, or gelatine birds for high speed impacts aimed at simulating bird strikes. [1] For this project the aim was to evaluate the behaviour of an out-of-plane impact to a composite panel delivered by a deformable projectile. A material that was easy to make and could survive several impacts without failure was required. Polyurethane is reasonably inexpensive, could easily be attained and moulded and was therefore selected as rubber material.

The PU rubber component was moulded into a half sphere of diameter 160 mm, with a 15 mm thick cylindrical base diameter of 210 mm. The base allowed for a clamping area through which the rubber could be clamped onto the projectile carriage. The rubber was specified to have a shore hardness of 60, similar to that of a vehicle tire.

It is possible to determine the modulus of rubber from the shore hardness rating [22]. It was however deemed necessary to determine the required modulus experimentally due to the uncertainty of material composition due to the moulding process (process constituents were added by hand). A rubber moulding of well defined dimensions would be compressed uni-axially at two different deformation rates to determine a compression modulus and strain rate dependence.

The rubber was moulded into a cylindrical form, diameter 50 mm and length 45 mm. The rubber was compressed at low speed (0.5 mm/s to 2 mm/s) to obtain an effective Young's value for the material. The sample was held at maximum test displacement value to observe whether a change in load occurred.

Due to concerns of the damping characteristics of the material, dynamic tests with predetermined test speeds were also performed on the test sample. Tests were performed at 6 mm/s and 60 mm/s to observe the change in stiffness. Samples were cycled in different strain regions to determine whether the material could be approximated by a linear material model. As can be seen from Figure 13 below, the sample proved to be slightly less compliant at 60 mm/s than at 6 mm/s, but not significantly so (raw data is available in Appendix A). Assuming a single value for the stiffness of the rubber was deemed adequate and within the tolerance of the

solution. The average of the compression data gave a Young's modulus E (for the single axis compression) of 8.4 MPa for dynamic tests and 8 MPa for static tests. This corresponds to a shear modulus (G) of 2.8 MPa as for elastomers $E = 3G$. [22] The obtained value deviates from the Young's modulus that can be calculated from the shore hardness value of 60 using Gent's Equation [23]:

$$E(\text{MPa}) = \frac{0.0981(56 + 7.66s)}{0.137505(254 - 2.54s)} \qquad 28$$

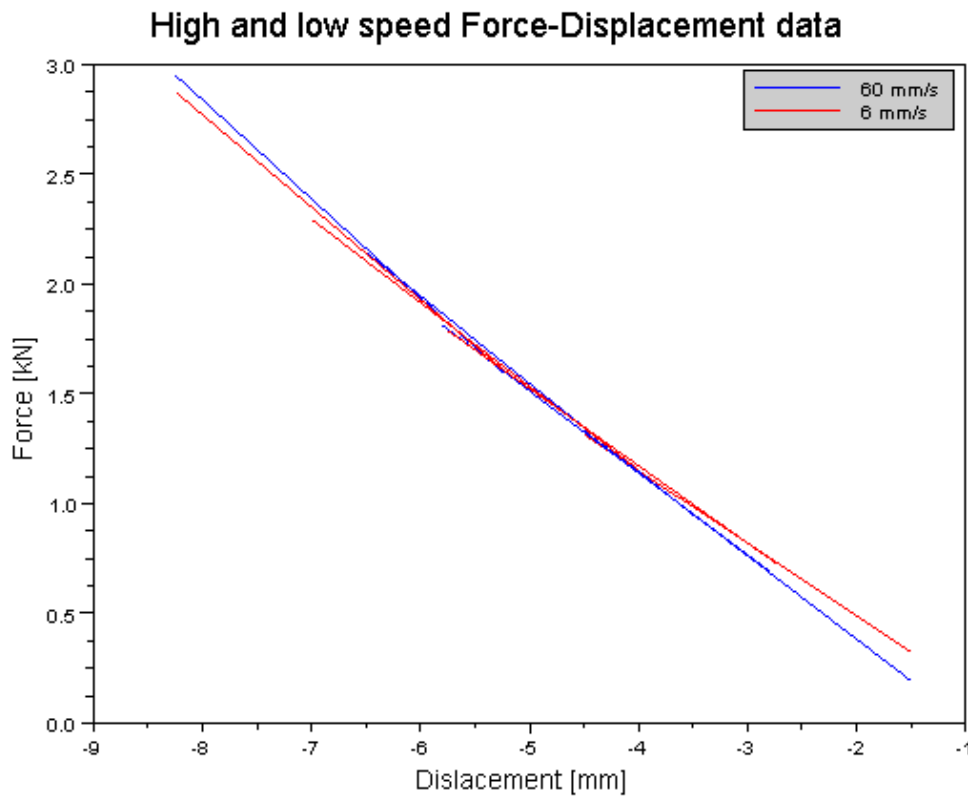Where s refers to the shore hardness.

Figure 13 Rubber test data for 6 mm/s and 60 mm/s

4.2. Impactor modelling

Although modelling the rubber itself was not a main aim of this thesis, it was important to have an accurate force input to the composite laminate to accurately describe the physical impact event. Rubbers are hyperelastic materials and can undergo large amounts of strain (in excess of 200%).

Ideally, the aim should be to approximate physical behaviour with as simple a model as possible. This reduces set up time and adding components to the model that increases computational time (cost) and complexity. The decision was made early on that the entire impact carriage assembly should not be modelled, and the simplest configuration should be used as a starting point. In order to avoid modelling the entire carriage assembly, initially only the rubber tip was modelled. The geometry of the rubber tip necessitated modelling with solid elements.

Of course, modelling only the rubber tip would severely underestimate the mass of the projectile, decreasing the inertia and the amount of energy delivered to the composite for a given impact velocity. There are two obvious approaches to remedy this. The first would be to simply increase the density of the rubber in the material property. The other solution is to add mass elements on the nodes of the rubber mesh. Both of these could deliver a rubber component with the same mass as the actual carriage assembly and with modification to the rubber property, deliver an input load approximating the actual load delivered to the target laminate.

An impact event in the initial configuration with a rigid target was evaluated. The initial results showed that this representation (with the rubber alone) was inadequate. The rubber itself is too compliant and unable to support the weight of itself during impact. The outer edges of the impactor would fold over the rest of the component and in so doing increase the contact time of the impact event. The outer edges also oscillated about their rest position leading to an inaccurate representation of the impact event.

An alternative approach was then considered. The projectile was split into two parts, but sharing common nodes at the interface, shown in Figure 14. No contact algorithm between the two was therefore necessary. The half spherical end of the rubber component was kept as a soft body impact tip, whilst a stiff metallic like material property was assigned to the base component. The aim of this was to keep the soft rubber at the contact interface, but with the required mass and stiffness provided by the base. Because the rubber component was rigidly mounted around its base in the physical impact test (as shown in Figure 10), minimal deformation was expected in the base region and therefore the initial stiffness value of the metallic component was viewed as arbitrary and could be changed to increase the accuracy of the obtained load curve when compared to the physical test result.

Initial stiffness and density values of the two components were assigned as Steel and Polyurethane rubber respectively. The metallic impactor base material property was assigned to MAT_001 (Elastic) and that of the base was assigned to a MAT_007 (Continuum rubber) property entry.
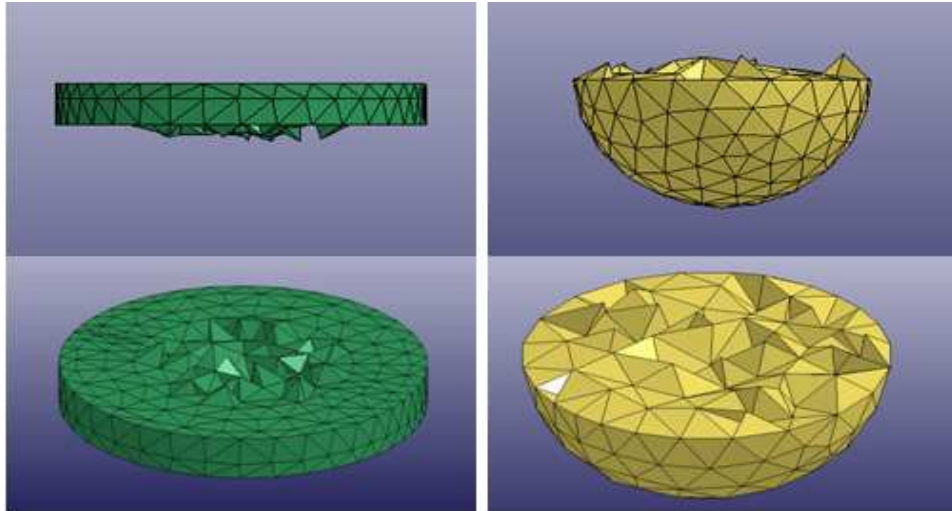
Figure 14 Illustration of the split rubber component

The Continuum rubber model was studied by Blatz and Ko [24]. The second Piola-Kirchhoff stress is given by Equation 29.

$$S_{ij} = G\left(V^{-1}C_{ij} - V^{\frac{1}{1-2v}}\delta_{ij}\right)$$ 29

Where *G* is the shear modulus, *V* is the relative volume, *v* is Poisson's ratio, δ_{ij} is the Kronecker delta and C_{ij} is the right Cauchy-Green strain given by Equation 30.

$$C_{ij} = \frac{\partial x_k}{\partial X_i}\frac{\partial x_k}{\partial X_j}$$ 30

Where the partial derivative terms refer to the change of relative position of two points x_k and the total deformation X_i and X_j in large deformation theory. For full development the reader can refer to [24]. The values used for the material card in LS-DYNA are listed in Table 2.

Table 2 Keyword input paramaters for MAT_007

Variable	Value selected	Signficance
MID	Unique ID	Unique material ID
RO	1550	Density of material in kg/m3
G	3.6×10^6 MPa	Shear modulus. See text Section 4.3.
REF	0	User can select reference geometry to initialize the stress tensor. 0 for off, 1 for on.

30

4.3. Evaluation of impactor model suitability

In order to validate the above approach tests were performed with the rubber projectile impacting a rigid metallic billet target mounted to a load cell. The test was performed at a range of drop heights and trolley weights. Weight and impact velocity was increased to a point where the rubber strain was in excess of what was expected during impact with the composite panel. In addition, a further constraint was added so that the mass of the carriage assembly in the model resembles that of the actual carriage assembly for each test.

The surface finish on the billet was smooth which ensured that it mounted flush to the load cell as well as providing a clean target surface for the projectile (a coarse surface would increase uncertainties in term of friction effects. The billet was centrally mounted to the load cell, which in turn was mounted to the building floor. The target was therefore assumed rigid, as very little deformation would be present on the billet/building floor in comparison with that of the projectile.

Both peak load and impact duration were important parameters to record during this test. Additionally, high speed camera footage was also recorded. These results could then be compared with the results obtained from the numerical analysis of the rubber projectile on a rigid target.

The physical test result was used as a baseline and the numerical result was then compared. The density of the rubber tip was initially set to the material value as in Table 2 to keep inertial properties at the contact interface as accurate as possible. Initially the shear modulus of the rubber was set to 2.8 MPa from test data. However, a slightly stiffer shear modulus of 3.6 MPa was chosen as it gave more accurate results over a wider load range when physical and numerical results were compared. The density of the metallic component was fixed (the total mass of the projectile was required to be the same), and a stiffness was found to represent the load curve as accurately as possible. As previously discussed, using a material stiffness equal to the rubber stiffness resulted in a impactor that was excessively compliant. For this reason, as a starting point, MAT_001 (Isotropic) was used and a arbitrary stiffness was assigned to the base part of the projectile. The assumption was made that due to the way the rubber was mounted most of the impact energy was absorbed in the tip, with low deformation in the rest of the body.

Peak forces and contact durations were compared, and the stiffness of the base component was used as calibration parameter. Higher stiffness would result in shorter contact duration and higher peak loads. This may be explained by the fact that the impact in this case may be viewed as conservative, and therefore the same amount of energy is absorbed regardless of the deformation (heat energy is not considered in the simulation). A stiffness value for the base of 200 GPa was found to work well for the discussed calibration parameters.

Figure 15 and Figure 16 display best case, worst case and a possible modified model stiffness (0.3 MPa) impact force for both the physical test result and the Dyna calculation. A density/stiffness combination was found to work well for the lower end of the impact force magnitude but over estimated impact load for the more severe impacts. The stiffness of the rubber could be reduced, the motivation being that the tetrahedral elements may be computationally too stiff, especially at higher levels of deformation. Using a 10 node tetrahedral proposes an alternate solution, as they are not as susceptible to such extreme volumetric locking as the 4 node elements. [20] The calculation for the decreased stiffness is displayed by the green curve in the second figure, with the blue the original stiffness. The modified stiffness however was not used in subsequent sections of the report in order to keep the amount of variables between model runs as low as possible.
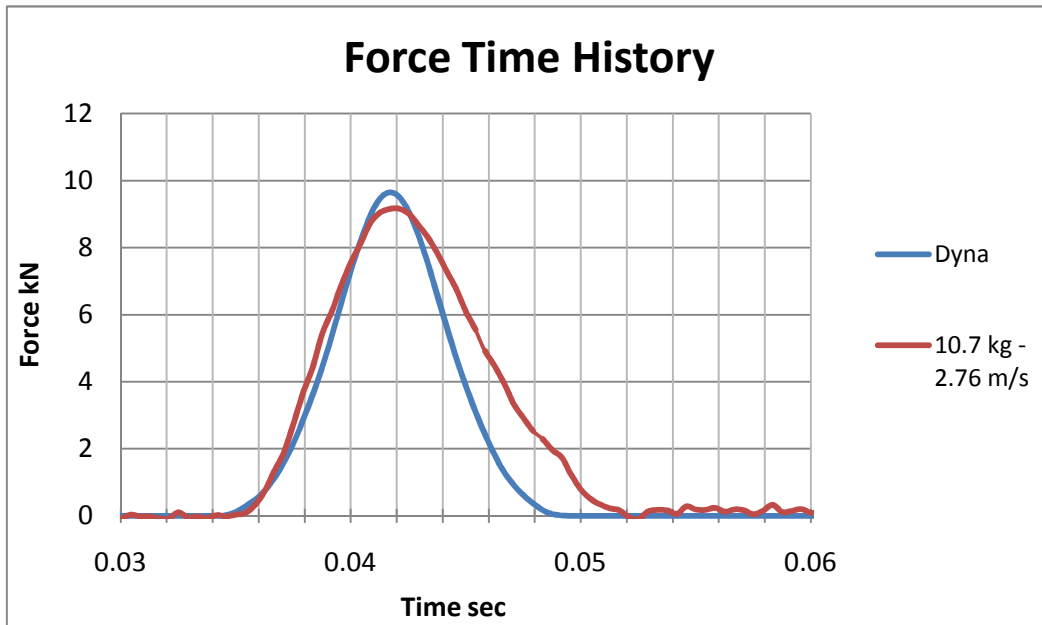

Figure 15 Best case fit for rigid target impact

32
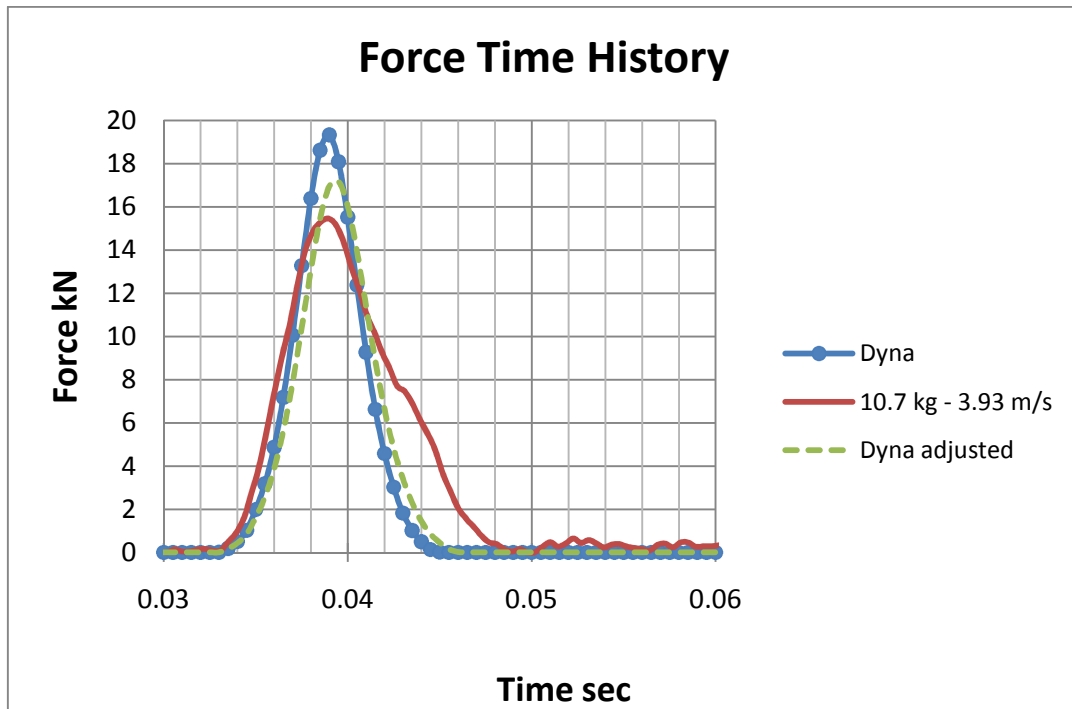
Figure 16 Worst case fit and adjusted curve for rigid target loading

When the curves are compared, notably the loading sections of the curves show better correlation. During the unloading phase, the physical model unloads at a lower rate than its loading rate. This could possibly be attributed to the deformation of the trolley to which the rubber is. The trolley inertia affects the load rate and the base plate of the trolley is not completely rigid. The base plate of the trolley acts as a spring between the load and the mass, causing a time delay in the acceleration of the trolley/projectile. The numerical model loads and unloads at the same rate, resulting in shorter contact duration. This has the effect of a higher peak load than in the physical case in order to absorb the same amount of energy.

No amount of change to the base component stiffness could remedy the problem, and a more comprehensive study of the rubber component modelling is required to solve the problem. Values for the stiffness of the base (200 GPa) where used that gave the best possible correlation.

33

Chapter 5 Composite panel forming

To demonstrate the relative ease with which thermoplastic composites can be manufactured, a panel with single curvature was produced. This panel could also be evaluated for impact response. A brief report of the forming process follows in this section.

The material used was donated by Ten Cate® for research purposes. The material was from the CETEX line of thermoplastic composites. Ten Cate® CETEX is available with glass fibres and carbon fibres, in this case the carbon fibre model was used. The carbon fibres are continuous and are used to reinforce a Polyphenolyne Sulfide (PPS) matrix. The material samples were 2.48 mm thick, with $(0,45,-45,90)_s$ ply orientation. Single layers of the material are 0-90° weaves, and the lamina are therefore quasi-isotropic. Full material details can be found in Appendix C.

Material is procured in flat sheet format, and for flat panel testing simply required cutting to size. Curved panels were desired for two main reasons, to determine the effect of panel curvature on panel strength and investigate the claimed ease of the manufacturing process. According to theory, laminates had to be heated to above softening temperature to allow the resin to flow and simply be pressed into the desired shape using a suitable mould.

For the purpose of pre heating the part, the consolidated panel was placed in a grid of exposed heater elements. The panel was the moved using a pneumatically actuated rail system over a distance of approximately 2 meters to the mould area. The part was supported by a brass plate between the rails, painted black on the bottom side (for heat absorption) and polished on the other (Figure 18). The moulds were installed on a hydraulic press (Figure 17 and Figure 19), which lifted the sample from the rails and allowed it to be compressed between the mould platens. When the part had cooled sufficiently, it could be removed from the mould. The temperature of the IR heating elements and mould platens could be evaluated using thermocouples.

Parameters that were experimented with included the following:

- Laminate time and temperature in IR heater: Temperature and heating time had to be carefully controlled during the initial heating and cool down periods. The laminate temperature had to be higher than the softening temperature of the PPS matrix to enable resin flow and subsequent successful forming of the laminate. If the part was excessively heated in the radiation (IR) heater, the resin would burn which could be identified

by a burning odour. Additionally, if the part was kept in the IR heater too long, the resin would flow away from the laminate edges, affecting the resin content of the final part. Because the upper section of the part was visible, resin flow could easily be observed (as a discoloration of the part), and the time the part spent in the IR heater was determined empirically. Thermocouples in the upper IR heating element were also significantly higher than those on the bottom element even though the elements were controlled by a common set point. The reason for this was believed to be the convection flow of hot air from the lower element to the top element and radiation from the polished part side of the brass support.

- Press time and temperature: The mould platens were also heated to control the cooling rate of the resin material. If the resin material cooled down too quickly, an aesthetically displeasing brown discolouration was observed on the (ideally white) resin material. The effect thereof on the mechanical integrity of the component is unknown however. The brown discolouration can be attributed to oxidation of the resin material.

- Platen alignment: In order to obtain the best possible part finish and uniform pressure distribution, the mould and die had to be aligned as perfectly as possible.

After several experimentation runs, satisfactory results were obtained from the cycle as described in Table 3.

Table 3 Heating times and temperatures for most satisfactory samples

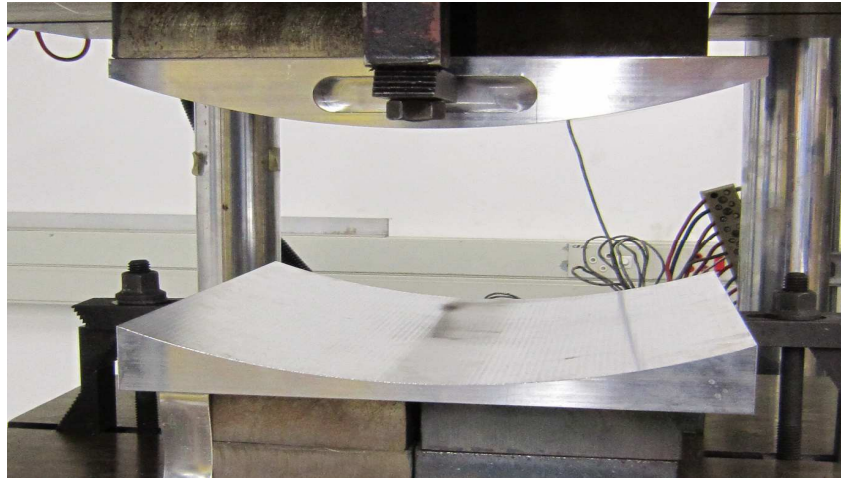|			
Heater	Temp top element	270	°C
	Temp bottom element	185	
	Time	02:45	min
Press	Top Platen	164	°C
	Bottom Platen	170	
	Time	02:00	min

35

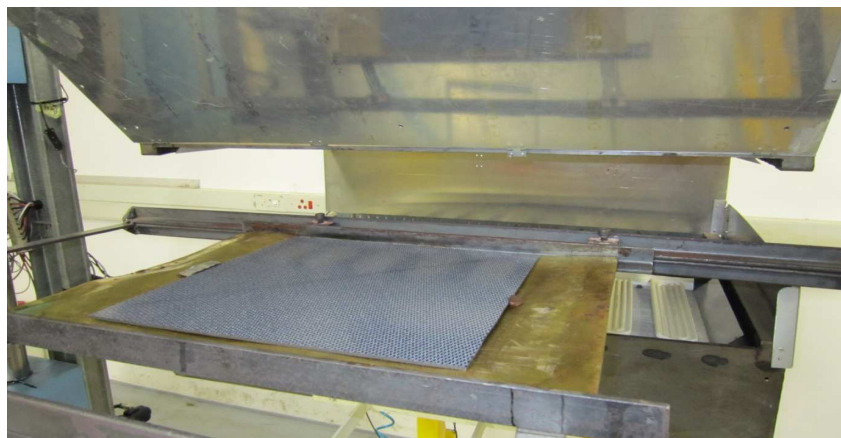Figure 17 Heated press platens and mould

Figure 18 Flat panel on brass plate in IR heater before pressing operation

Figure 19 IR heater and press over view

36

Chapter 6   Laminate modelling procedure

The main aim of the thesis was to model the impact event, to the setup described above, using shell elements for the composite laminate. LS-Prepost was used to create a keyword file for LS-DYNA, the solver used for the simulation. In this section, the process regarding the modelling procedure will be discussed.

6.1. Standard model

The first model formulation evaluated was a standard single layer shell model. A shell material property was created with a composite material property assigned to it. The user specifies that the shell property is assigned to a composite material by setting ICOMP = 1 (flag for composite material theory) in the SECTION_SHELL input card. A number of layers can be specified by means of the NIP (Number of Integration Points, eight, one for each layer, in this case) parameter, along with a material ply angle for each integration point.

The standard model was used to evaluate the support condition and friction values at the contact interface. The standard model was also used as comparison to other model formulations as well as the physical test results.

6.1.1.   Material model selection

As discussed in detail in the literature section, MAT_058 was selected for modelling of the composite panel. MAT_058 was specifically designed for laminated composites, allowing modelling of failure events.

Material values obtained from the supplier (available in Appendix C) were input into the solver card, including tensile and compressive modulus, Poisson's ratio and in plane failure stress and strain. The failure surface option FS was selected to suit laminated composite fabrics (there are other options available specifically to suit UD laminates). Material ply orientation was set for each layer, and an integration layer for each layer added in the CONTROL_SHELL keyword, to extract stress/strain information for each laminate layer.

6.1.2.   Model support condition

It was quite clear from the start that the composite alone could not be modelled without the support structure, but the question remained whether modelling the entire support could be avoided. Boundary conditions are particularly difficult to approximate even with seemingly simple models. Often assumptions have to be made about the boundary conditions, and the effect thereof on the model.

To revisit, the composite panel is clamped to its mild steel base support frame. The base support frame is mounted to a 180 x 180 x75 mm mild steel billet which in turn is mounted on the load cell. The sides on which the composite panel are mounted are elevated 60 mm from the base to allow for the deformation of the composite during impact.

A certain amount of energy would be absorbed during impact. If the projectile was assigned a kinetic energy (in the case of the model) of 100 Joule, 100 Joule would have to be absorbed by the composite and the structure that supports it. For a condition where no failure occurred and damping was not considered, after contact the 100 Joules of energy would be divided into kinetic energy for the projectile and a small amount of internal energy in the composite and its supports due to vibrations resulting from impact.

Keeping in mind that the amount of energy in the system is kept constant and that the energy exchange is between the projectile, the composite and its supports we can make some conclusions about the effects of the support condition. More deformation in the composite and its supports (the target) would result in longer contact duration and lower peak forces because:

$$W = Fs \hspace{4cm} 31$$

Where:

W = Work performed by the projectile on the target.

F = The contact force.

s = The distance (deformation) of which the force F acted.

Therefore, support conditions on the composite that are not compliant enough (such as a fully fixed constraint on the composite edges) would lead to a result with a peak load that over estimates the stiffness of test condition (and hence the force), over shorter contact duration.

For the above reason, even though the composite panel is clamped into its support frame, to assume a simple clamped condition for the composite panel would be incorrect. The base support itself deforms and allowance for this has to be made in the model.

Three boundary conditions were selected for evaluation (Figure 20). The first was a full translational constraint on the nodes where the composite target was supported by its mounting structure. The second included the upper pedestal supports of the support frame, of which their supports were fully constrained for translations. The third constraint condition included the full support structure, with nodes in contact with the load cell mounting interface constrained. The three

conditions subjected to an arbitrary load with peak load mid plane stress states are displayed in Figure 20.
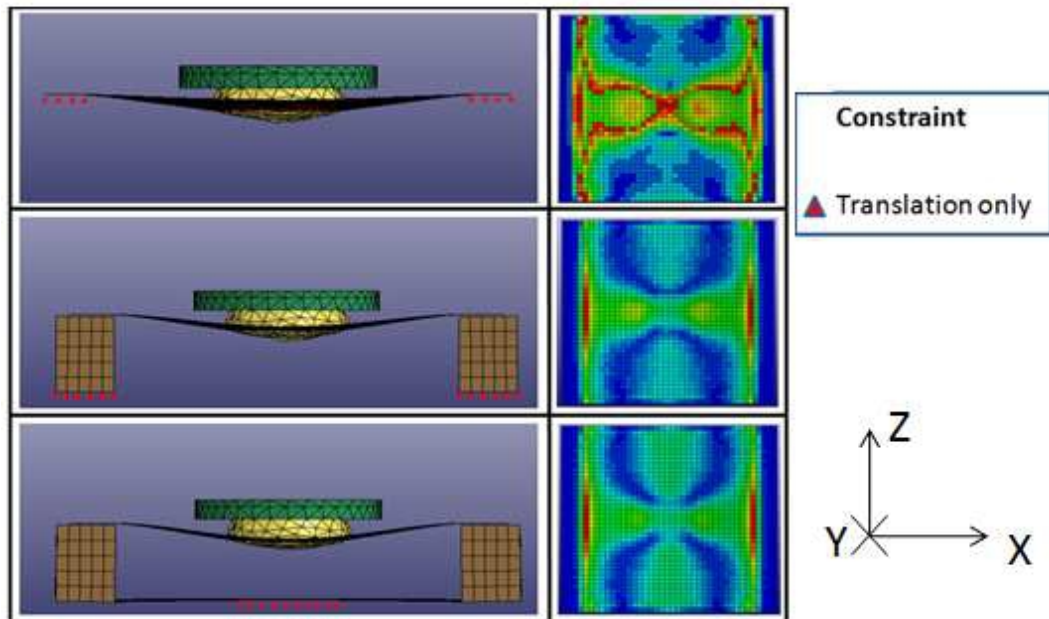

Figure 20 Comparison of constraint methods and combined stress plots. The axis indication refers to images on the left

The result from the arbitrary load condition is plotted in Figure 21. The pedestal support curve is slightly lower in magnitude than the rigid support due to the added compliance of the added supports. The full support condition however reacts with a marked decrease in peak force level and increase in contact duration. The reader must keep in mind that the areas under these curves are all the same, and that the peak load and contact duration are interdependent.
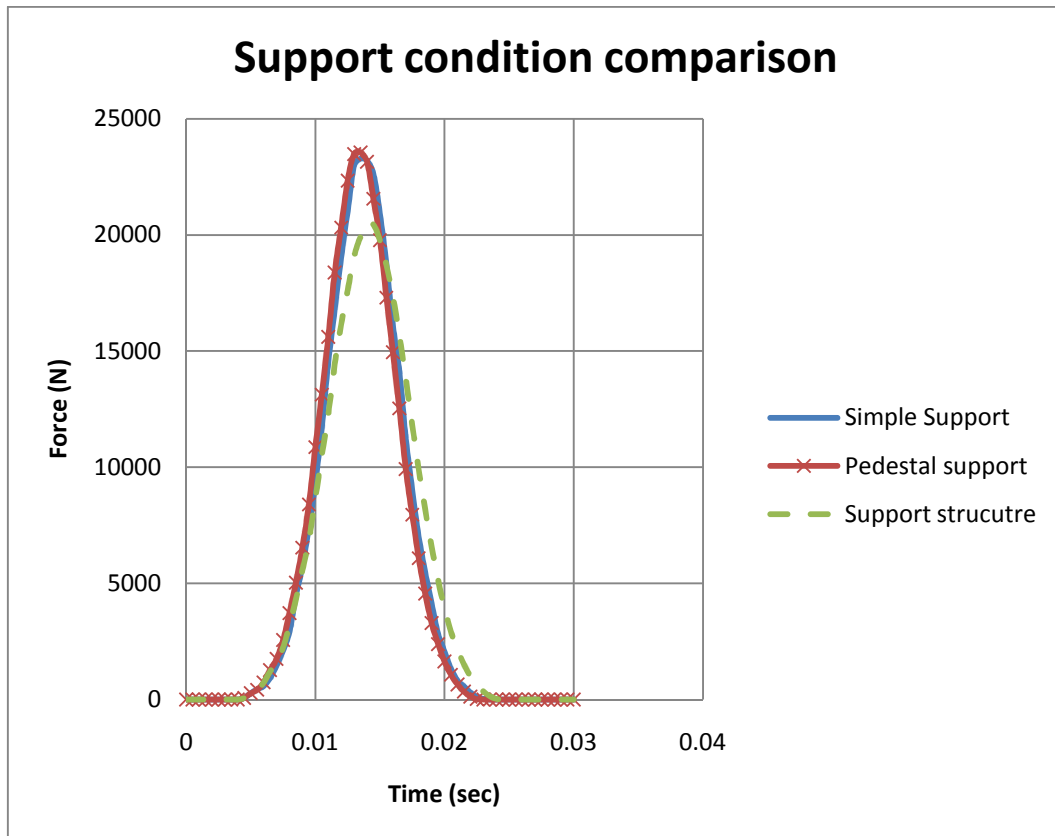
Figure 21 Comparison of support condition for an arbitrary impact load

High speed camera footage confirmed the need for the fourth boundary constraint condition. The deformation of the target base panel was apparent when the footage was reviewed (Figure 22), notable from the inward deflection of the upright supports. Although the deformation amplitude is small (especially compared to that of the composite), it had a significant effect on the shape of the obtained load curve. Therefore, the entire target base support was included in the FE model, with the steel billet assumed to be a rigid connection to the load cell (ground).

The target base support was constrained for all translations at load cell interface bolt locations, and for z (vertical) translation only in the region where the support base rests on the steel billet. This is not an ideal approximation of the reality, as this prevents z movement in both up and down direction whereas physically this is only the case for the downward direction (increasing the bending stiffness of the base plate). However, the stiffness of the base plate and the close proximity of the mounting holes meant that the region outside the supported area had a much greater effect on the overall behaviour of the support structure.
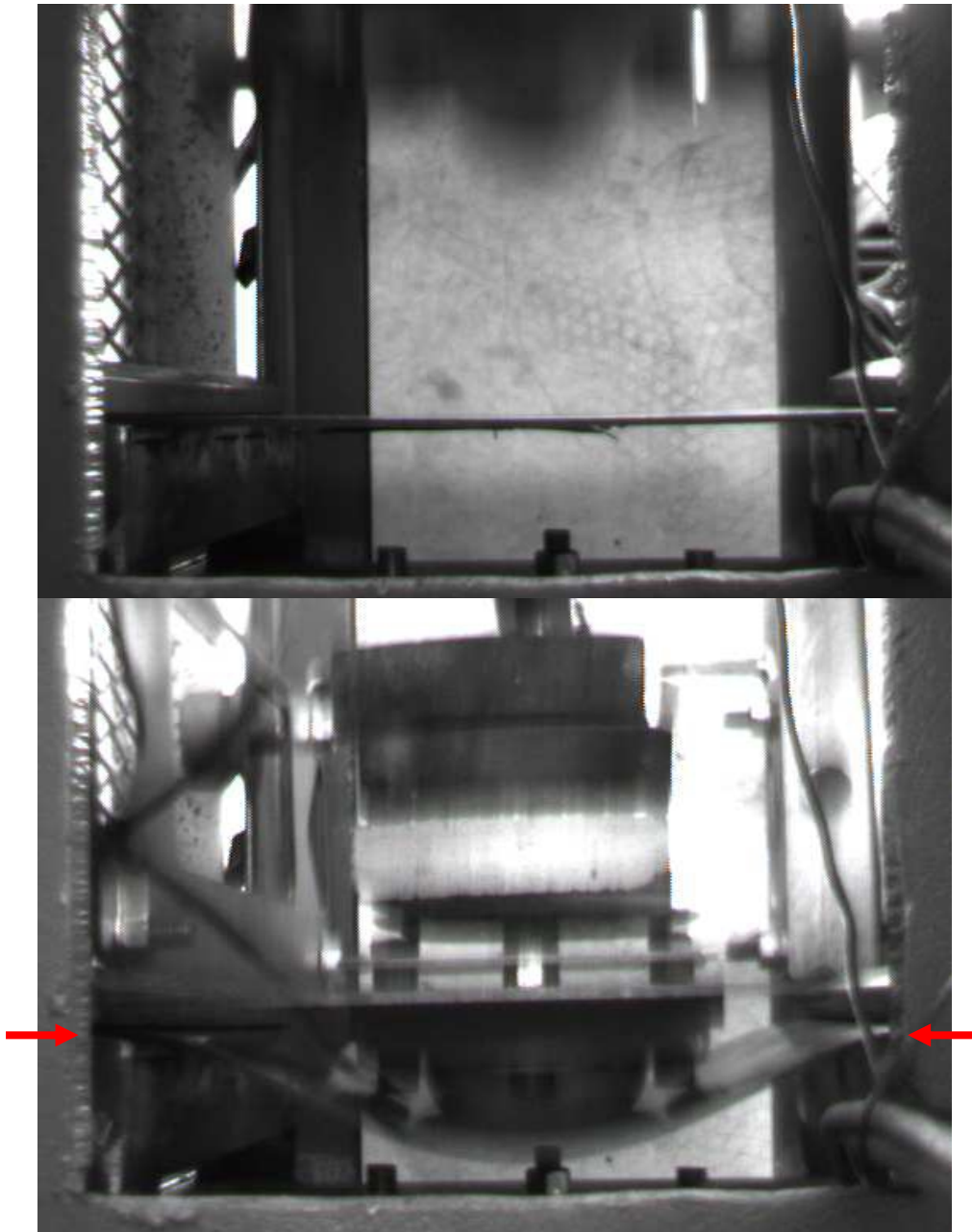
Figure 22 High speed camera footage of high load (240 J) impact. Note deformation of support structure at mounting interface at the arrow locations.

Another area where boundary conditions had a significant effect was the area in which the composite panel was clamped to the support frame. Mounting bolts were spaced 30 mm apart (giving 9 per side), and the composite was clamped to the frame through 15 mm thick steel sections. In this region the assumption was made that the composite is fully constrained to the frame (i.e. no slip between the composite and the frame) in the clamping area. This again was only an approximation of the physical interface, but the lack of witness marks after several tests suggest that this method was appropriate. This was achieved by

41

using the CONSTRAINED_NODES option in LS-DYNA, which couples nodes for specified degrees of freedom. In this case the nodes on the composite were coupled to those of the support base for translational degrees of freedom x, y and z. After reviewing initial results however, the amount of nodes constrained were re-evaluated and decreased by one row of nodes. This served to further improve the accuracy of the simulation, decreasing the amplitude while simultaneously increasing the duration of the impact event.

6.1.3.   Parameters at contact interface

The first parameter affecting the contact area between the projectile and the target is the detection and response algorithm used at the contact interface. In terms of the contact detection, the application is not extremely challenging for the software to handle, as the penetration components and sides can be determined beforehand. Any of the many available contact algorithms would be suitable for this purpose, but NODE_TO_SURFACE contact was chosen for this application.

Friction values at the contact interface could be specified in the contact card. Friction sensitivity in the model was evaluated by running upper and lower bound friction runs. The upper bound was run at both static and dynamic friction coefficients set to 1. The lower bound friction run was done with friction disabled in the contact algorithm. The results revealed that friction does not have a severe effect on the model with regards to the impact area. In Figure 23 it can be seen that the vertical displacement of the centre node on the laminate in not affected by much, and the same is true for the impact force observed in Figure 24. All model results reported therefore have friction disabled in the keyword. In addition, contact damping was also investigated and found to have no detectable effect on the simulation results of interest.

Friction sensitivity
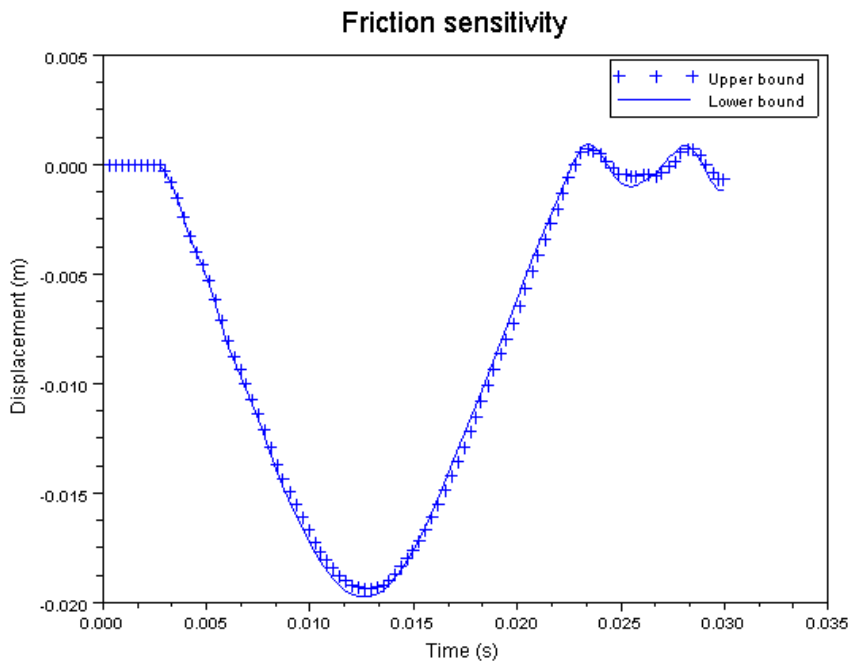

Figure 23 Displacement comparison of upper bound and lower bound friction runs compared an arbitrary load case

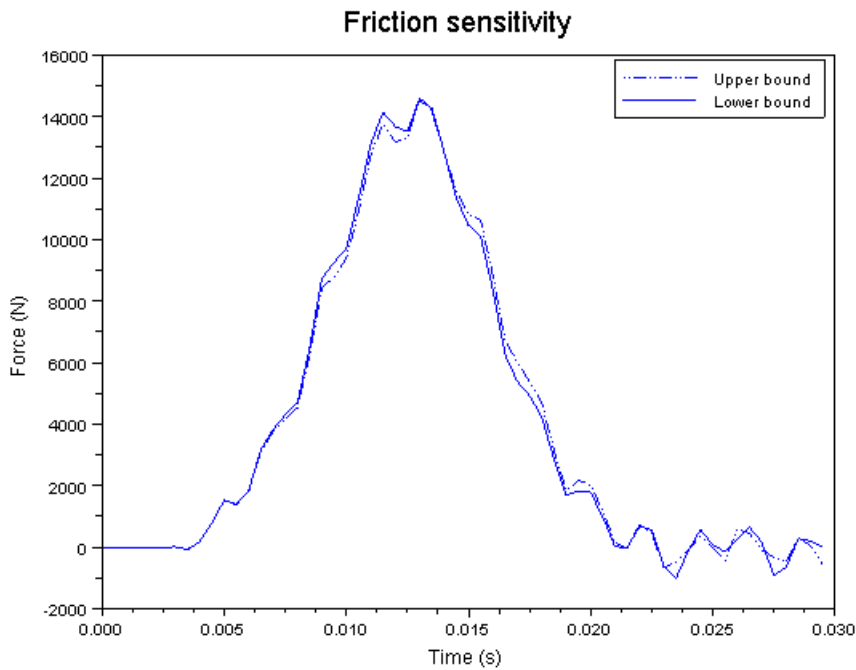**Friction sensitivity**

Figure 24 Force comparison for upeer and lower bound friction settings at arbitrary impact load

43

6.2. Stacked shell layer approach to modelling the laminate

The second model formulation to be evaluated was the multi-layer representation. For the stacked shell simulation the primary model principle remained the same. A soft body projectile was released onto a deformable composite target supported by a structure approximating the physical test structure.

A critical difference between the two model representations is the fact that the composite laminate is in this case represented by a shell element laminate. Each lamina in the panel is represented by a separate shell layer (Figure 25). The shell layers are connected by using a contact algorithm between the layers

After careful consideration of which of the available contact algorithms to use between the shell layers, the decision was made to use CONTACT_TIEBREAK_SURFACE_TO_SURFACE. The main reason for this was that the rotational freedom of the shell elements could be tied to each other, an option not available in many of the other tied contacts. Not being able to tie the rotational degrees of freedom to one another is acceptable for contact between solid elements but not so in this case as shell elements are used. Shell layers were connected in a staggered format, i.e. layer 1 to 2, 2 to 3, 3 to 4 and so on. Physically, shell layers were offset from one another by the laminate thickness of 0.31 mm and assigned thickness as such in the shell property keyword. Shell definition also no longer required eight through the thickness integration points, and the default value of 3 integration points (upper, mid and lower surface) was reinstated.
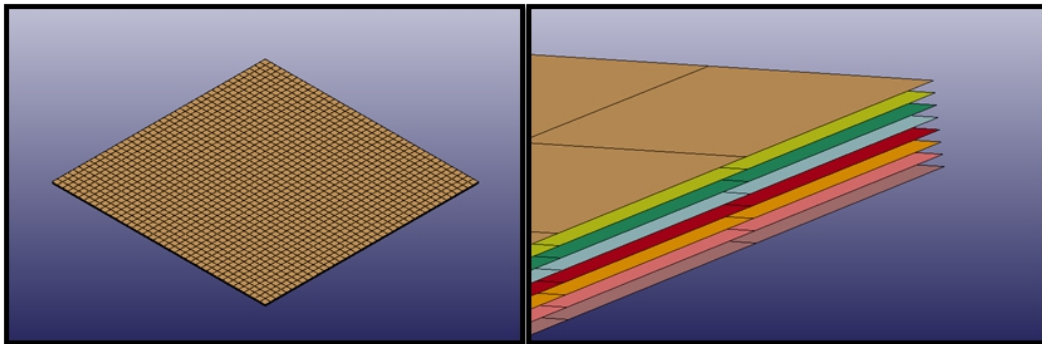

Figure 25 Representation of stacked shell layer modelling approach

In effect this changes the composite shell definition, with eight through the thickness integration points, to eight shell definitions with three integration points. Because the laminate was symmetric in this case only four unique shell definitions were required. The material axis was aligned in the shell property definition as before, so the first layer at 0°, second at 45 ° and so on.

Using this model representation gives the user control over two parameters not controllable otherwise. The user is able to control the interlaminar stiffness and the failure stress between the two laminas. This has great benefits when

attempting to simulate delamination of composite panels. An added difficulty in this format however is how LS-DYNA handles the shear behaviour between the laminate layers. Sliding motion (shear) can either be completely prohibited between adjacent nodes (leading to an overly stiff laminate) or can be controlled by friction parameters.

To evaluate the effect of friction on the contact between the laminate layers, runs were compared with a high value of static and dynamic friction. For the high friction evaluation, a number of 1 was assigned to the static friction and dynamic friction. As seen in Figure 27 for a high load of 240 Joule impact the effect of the friction on the centre node displacement and constraint force is not significant. This load case was used for comparison as it was the highest evaluated load and would have the maximum displacements and therefore the highest level of friction dependence (if any).

The higher friction coefficient did however have a small effect on the laminate stresses. When stresses in local axis directions (0° and 90°) a higher stress level was found for the higher friction value. The stress patterns remained the same. For the peak stress on the top layer of the composite in the 0° direction for instance, as in Figure 26, a 2% higher maximum stress was recorded. For this reason the high friction values were maintained in the model to obtain a more conservative result.

An appropriate value for the friction value had to be selected otherwise the shear stiffness would not be representative of the physical laminate. The effect of the friction coefficient on the stresses was evaluated by doing a sensitivity analysis. The decision was made to use a coefficient value of 1 to prevent sliding in areas where the normal force between the layers was low. This parameter could be evaluated better with the help of a stress measurement on the laminate and should be considered in future research.

The maximum friction force was limited by the VC value on the contact card as in Equation 32. This value was recommended by the LS-DYNA keyword manual [25] and is of the same order as the shear strength.

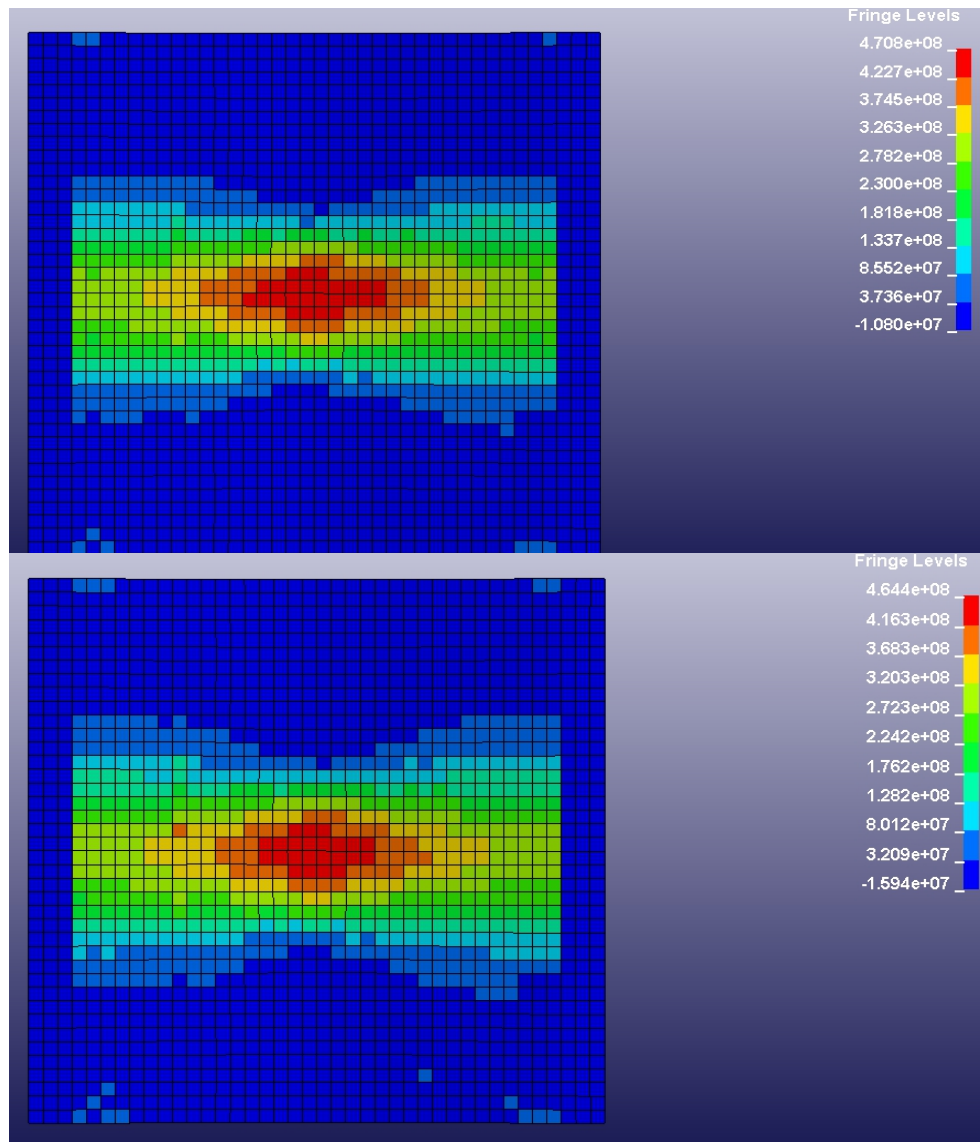$$VC = \frac{\tau_{yield}}{\sqrt{3}} \qquad\qquad 32$$

Figure 26 Comparison of fibre stresses for friction settings. The top figure is for the high friction setting

A further option that was evaluated was to use the AUTOMATIC_SURFACE_TO_SURFACE_TIEBREAK contact option. The same parameters applied to the contact definition as before, but tangential motion could be prohibited completely until either NFLS (failure in tensile mode) or SFLS (failure in shear) failure values were reached. Surprisingly the same result was obtained as runs performed with TIEBREAK_SURFACE_TO_SURFACE without friction enforced. The implication thereof is that the relative motion between layers are not properly prohibited, or the tied interface is not functioning properly (not tying nodes). To evaluate whether the tied interface was functioning correctly, nodal forces in the composite were evaluated to determine whether tension forces were present in the contact event. Tension forces were found in the contact history (refer to Figure 28 for a plot of selected nodes) suggesting that the

46

nodes were tied. The reason for the relative nodal displacements for the automatic contact was therefore unknown, and the decision was made to use the TIEBREAK_SURFACE_TO_SURFACE option.
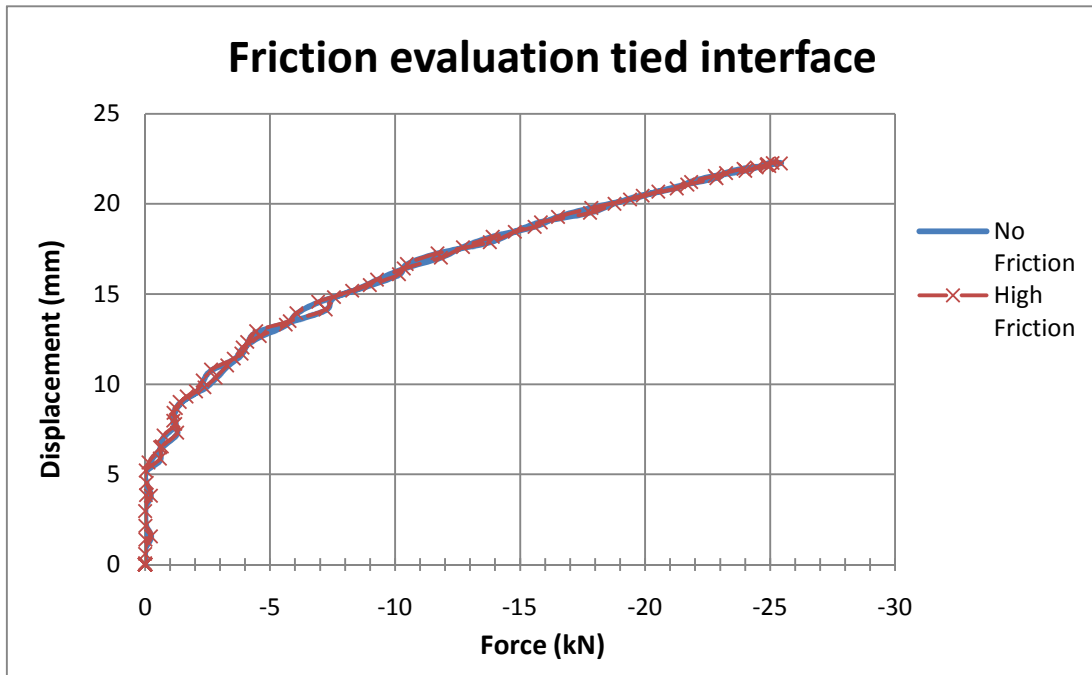

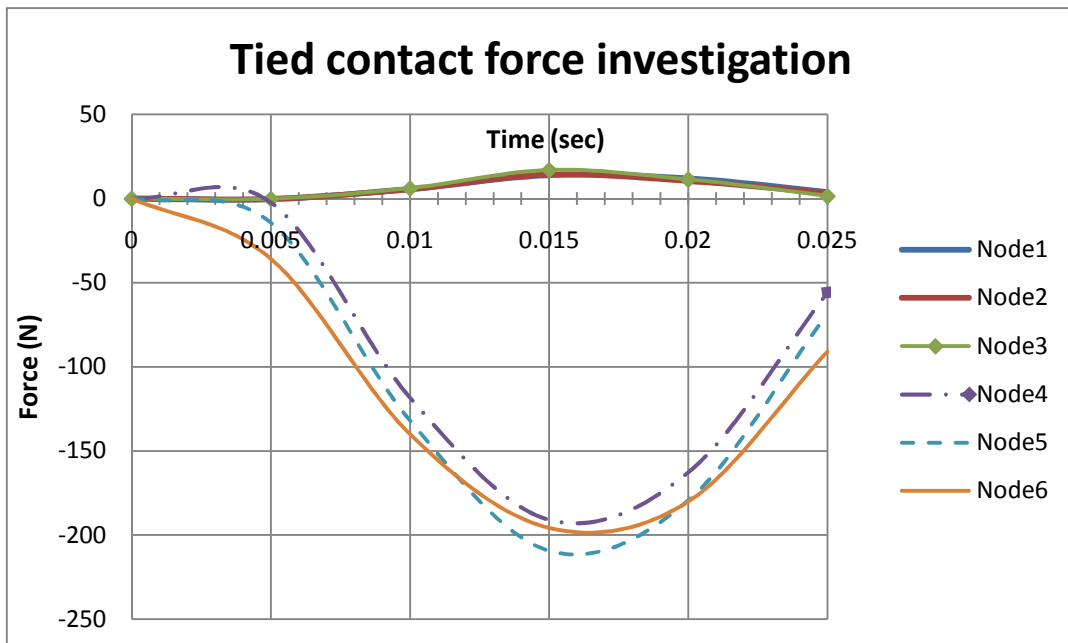Figure 27 High and low tied interface friction comparison

Figure 28 Comparison of nodal forces for tied interface contact. Note that positive and negative nodal forces are present.

47

For the model considered, the interlaminar stiffness and tensile failure stress was determined from the resin tensile strength and stiffness. The shear strength was also derived from the resin properties. The failure stress for both tensile and shear properties may be input directly into the contact keyword (NFLS and SFLS parameters respectively). These values are available from the material specification sheet in Appendix C. Failure of the tied contacts is controlled by the following Equations 33 and 34. When these are compared to the failure conditions discussed in section 2.4 it is found that the shear failure in this instance corresponds to the 2D-Hashin criteria for tensile matrix failure (Equation 9) and the tension failure corresponds to the Equation proposed by Zhang [14] for peeling failure (Equation 13).

$$Shear: \quad \left(\frac{|\sigma_s|}{NFLS}\right)^2 + \left(\frac{|\sigma_n|}{SFLS}\right)^2 \geq 1 \qquad\qquad 33$$

$$Tension: \quad \left(\frac{|\sigma_s|}{NFLS}\right)^2 \geq 1 \qquad\qquad 34$$

Where σ_s and σ_n are the shear and normal stresses respectively

In order to adjust the interlaminar bonding (in this case the tied contact) stiffness, the SFS and SFM parameters can be adjusted on the contact card. LS-DYNA can compute a default value for this parameter, but it is stability driven and may not represent the stiffness within the laminate accurately. The contact stiffness is calculated by the Equation 25, repeated from section 2.5.4 for convenience below. From the equation it can clearly be seen that the stiffness is stability driven, as the stiffness is mesh dependant and therefore coupled to the time step of the solution. If however the mesh is kept to a square quadrilateral element (easily done in this case), the stiffness is always scaled by a constant factor of 0.5 due to Pythagoras rule. The contact stiffness in this case, therefore, is not mesh dependant.

$$k_i = \frac{f_{si} K_i A_i}{Max \ (shell \ diag)} \qquad\qquad 35$$

One may also specify whether LS-DYNA should use the master or slave side to determine the contact stiffness. In this case it can be either without consequence, as the master and slave sides are identical. Consider the model with the following credentials per lamina and the resulting k_i and target k_i values as listed in Table 4.

Table 4 List of model parameters with resulting and target contact stiffness values

Property	Value	Unit	Property	Value	Unit
Laminate length	0.3	m	**Max (Shell diag)**	4.24×10^{-4}	m
Laminate width	0.3	m	**Tensile modulus**	3.80×10^{9}	Pa
No. Elements	1600	#	**Distance between lamina**	3.10×10^{-4}	m
f_{si} (default)	0.1		**ki**	3.50×10^{5}	Nm^{-1}
Ki	2.60×10^{10}	Pa	**Target ki**	6.90×10^{8}	Nm^{-1}
Ai	5.60×10^{5}	m^{2}	**Target f_{si}**	1971.4	

Target k_i was calculated by viewing the contact algorithm as a set of linear springs connecting nodes as described in [20].

$$Target\ k_i = \frac{E_{Resin} A_{Element}}{Distance\ between\ lamina} \qquad 36$$

From the Table 4 it is apparent that the default value assigned by LS-DYNA for the contact stiffness underestimates the physical value. This may be adjusted by using f_{si}, the user specified scaling component for contact stiffness. When scaling the contact stiffness value, one must be mindful of creating model instabilities.

In order to achieve the target contact stiffness the user scale level (f_{si}) should be set to almost 2000. However, any attempts at increasing the contact stiffness by any meaningful amount (one order of magnitude or more) resulted in immediate model instability. Increasing f_{si} by an order of magnitude caused the laminate to explode without any load applied thereon. A screenshot of the first plot time step (set to 2 milliseconds) is shown in Figure 29.

In an attempt to address the problem, the time step was scaled down. It was found that the time step had to be scaled so far down that the solution was no longer practical. Increasing f_{si} to 20 on only one layer required a TSSFAC = 0.02. TSSFAC is a user controlled parameter that specifies how the software computed time step should be scaled. Using this value of TSSFAC with the current mesh configuration delivers a time step in the order of 1 millisecond, without significantly improving the accuracy of the simulation. Attempts at changing contact thicknesses and physical distance between the layers were also

unsuccessful. The result was that the default value of 0.1 for the user controlled value was used.
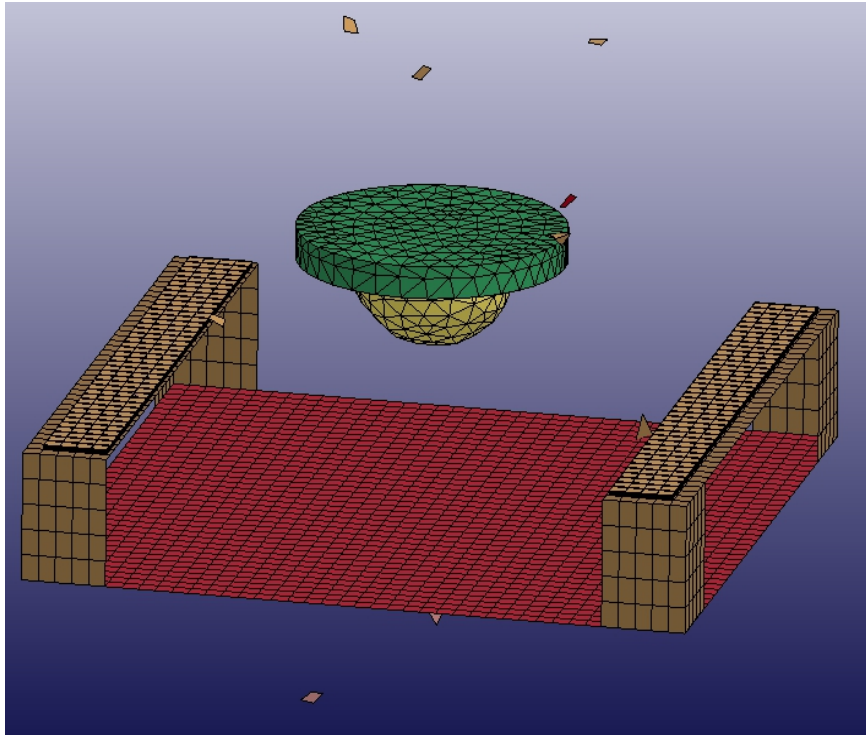

Figure 29 Result at first time step of increased contact stiffness between shell layers

6.3. Added integration point approach to modelling the laminate

A third approach to modelling the composite panel was taken. Rajbhandari et al. proposed a method whereby a single shell layer was used to model the composite panel, as in the single layer approach, with added integration points which act as resin rich layers between each layer of composite fabric (Figure 30).

This approach aims to capture delamination failure within a reasonable accuracy with significantly less processing time when compared to the stacked shell approach discussed in the section above. The model therefore aims to combine the advantages of the single shell layer representation such as simple setup and quick processing with the (potential) added accuracy of the stacked shell approach. The major limitation of the method in this regard however is the lack of a normal force component within the elements. [3]
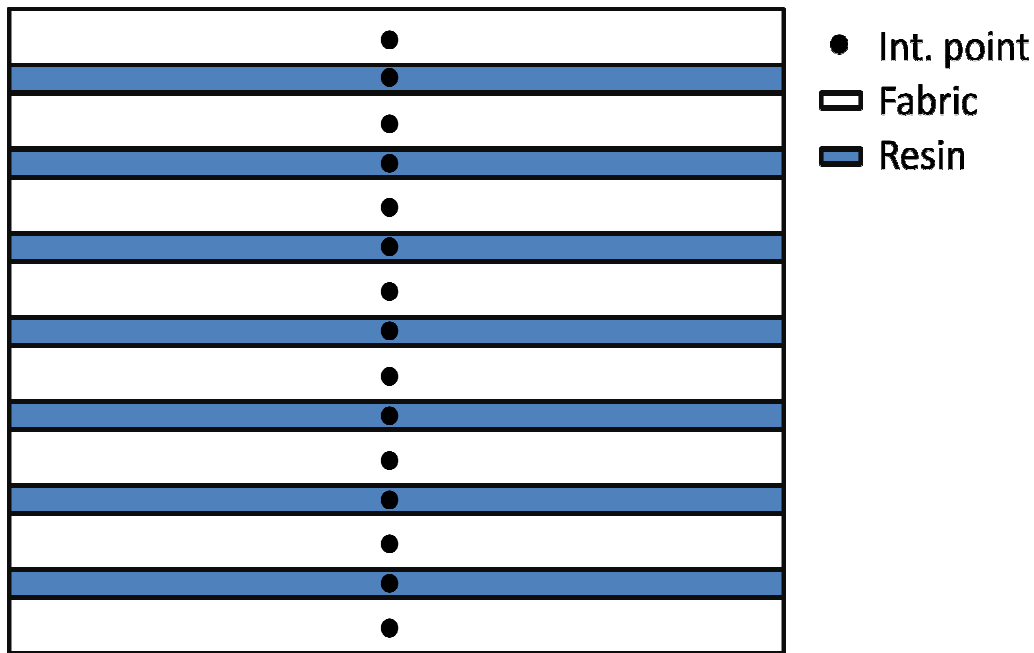
Figure 30 Methodology behind Rajbhandari et al's approach to modelling laminates

6.3.1. Key variations

In order to add these resin rich integration points to the existing model requires some key changes to the model keyword file. The contact algorithm and boundary conditions are unchanged. The shell definition however, is changed completely. The material and section properties are no longer assigned by using the SECTION_SHELL card, but rather by using the PART_COMPOSITE card.

The part is defined by assigning integration points with a material property, thickness and material orientation. MID1, THICK1 and B1 where used for the composite fabric and MID2, THICK2 and B2 where used for the resin layer.

An additional variable requiring consideration in this model is the thickness of the resin layer. The total thickness of a cured layer is 2.48 mm. The thickness of the fabric was set to 2.46 mm and that of the resin to 0.02 mm initially and was investigated at a later stage.

6.3.2. Eigen value extraction

In an effort to validate the material thickness assigned to fabric and resin integration points, an Eigen value extraction was performed. The thickness of the fabric and resin were varied but always so that the total thickness of the laminate (sum of fabric plus resin) was kept constant at 2.48 mm.

Whilst performing this investigation an interesting phenomena was encountered. The stiffness of the laminate varied considerably with variation in resin

percentage, but not in an intuitive manner as seen in Table 5 and Figure 31. Take not that for this comparison the accelerometer mass is not included.

Table 5 Fundamental frequency of laminate calculated by eigenvalue extraction with varying levels of resin content

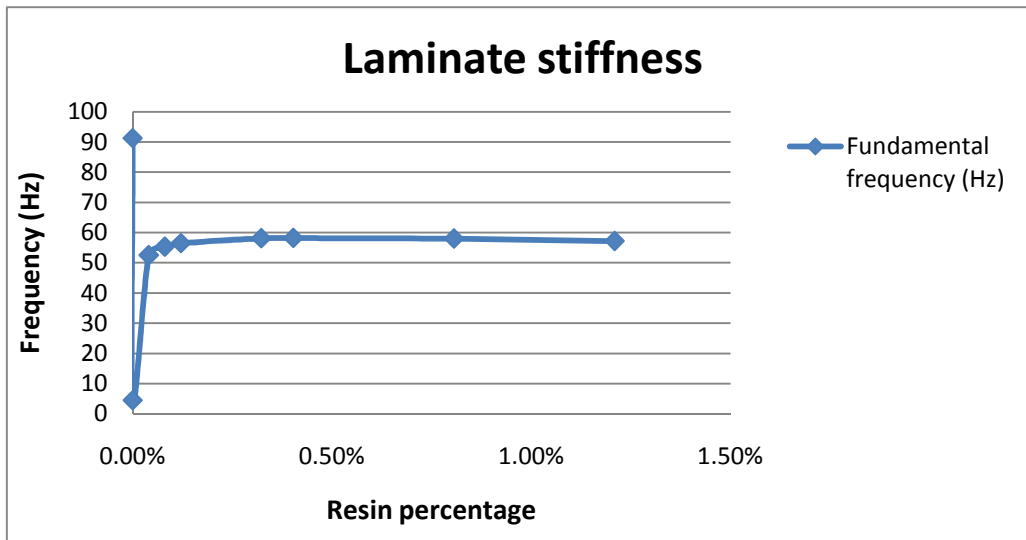| Resin thickness	As Percentage	Fundamental frequency (Hz)
0	0.00%	91.2
1.00E-06	0.04%	52.5
2.00E-06	0.08%	55.3
3.00E-06	0.12%	56.5
8.00E-06	0.32%	58.1
1.00E-05	0.40%	58.2
2.00E-05	0.81%	58
3.00E-05	1.21%	57.2

Figure 31 Graphical demonstration of Table 5

From a resin percentage of 0.5 % upwards, as expected the stiffness of the laminate decreases as the resin percentage increases. The resin is significantly more compliant than the resin impregnated fabric and therefore increasing the percentage thereof will have a detrimental effect on stiffness. However, when decreasing the resin percentage from 0.5 % the stiffness of the laminate also decreases. The decrease in stiffness accelerates as the resin percentage is further decreased. A point of discontinuity is reached near a resin percentage of 0, where

the laminate fundamental frequency (and therefore the stiffness) returns to the value as obtained by the conventional shell method.

The reason for this is believed to be numerical accuracy and round off errors. This however was not reflected in the explicit analysis. A recommendation for further clarification on the phenomenon is to perform the same simulation with the units reconfigured to millimetres.

6.4. Initial comparison of model formulations

When comparing the model results for an arbitrary load case as in Figure 32, notably the two single element layer models deliver the same result (as in the ideal condition) and the stacked shell delivers a slightly stiffer result. This may be explained by comparing the effect of the boundary condition imposed by the constrained nodes on the stacked shell model. The constrained top surface nodes increase the bending stiffness relative to the constrained mid plane nodes of the single layer models. This increase in bending stiffness has the effect of increasing the peak load while shortening the contact duration.
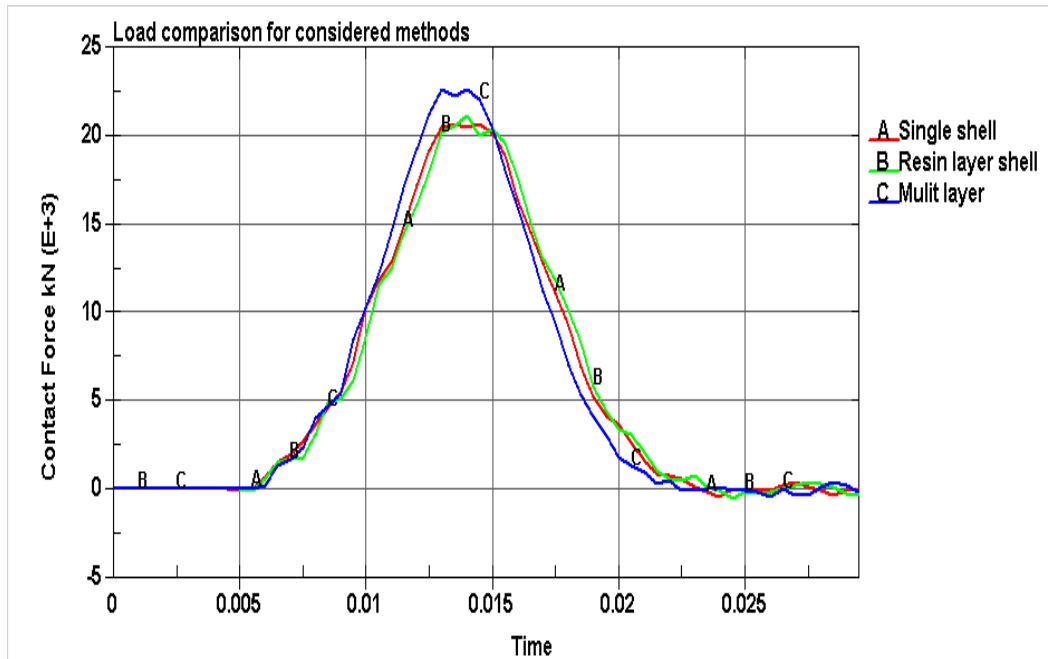

Figure 32 Initial comparison of three model formulations

Chapter 7   Drop test results

The target laminate was impact loaded with various velocity and weight combinations. Velocity and weight values were chosen so that an overlap existed between combinations for the same impact energy value. This was done to determine whether impact response load was purely energy driven, or whether different results are obtained for low mass/high velocity and high mass/low velocity. Impact weights varied from 6.4 kg to 24.5 kg and impact velocities from 2.7 m/s to 4.4 m/s. Laminates were therefore subjected to impact energies from 24 – 240 Joules (Figure 33,
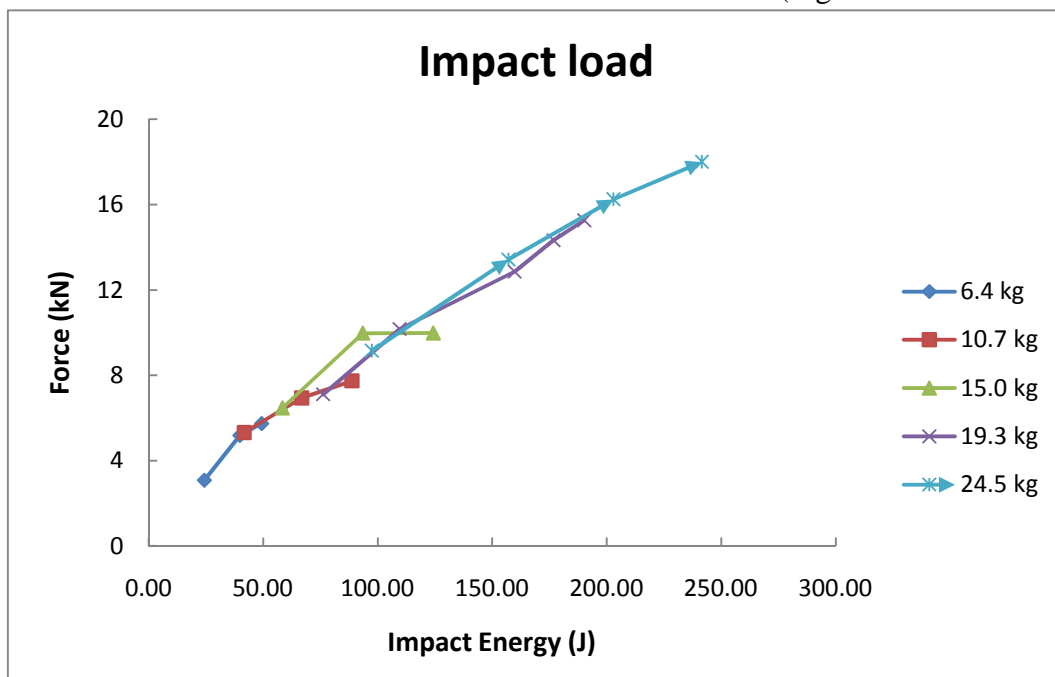

Figure 34 and Figure 35).

In Appendix B raw test data is displayed on charts for impacts on target laminates. As expected, when impact energy (impact load) increases, the peak force and displacement amplitudes increase for all load cases. However, contact duration decreases for increased impact energies with the same mass loading, as shown in Figure 33 below. Increasing the mass of the carriage while maintaining the energy level increases the contact duration while the peak force and displacement stay largely the same. This holds true because the energy (work) is a function of the force applied over distance. Therefore for a higher velocity/lower mass the acceleration must be higher to obtain the same force (according to Newton's second law).

54

While investigating the force displacement graphs (Figure 63 in Appendix B), for higher loads a gradient change is noted near the peak load section of the impact event. The force increases while the centre point downward displacement of the laminate remains virtually constant. This may be attributed to two factors. The first is the increased membrane effect produced by the laminate. As the centre of the laminate is displaced downward by the bending action caused by the transverse impact, the laminate is stretched by an increasing amount. As the laminate centre is displaced further, the ratio of in plane stretch versus vertical displacement does not increase linearly and results in the load increasing at a higher rate than the displacement. A second factor contributing to this is that as the load increases, an ever larger area of the rubber contact point is engaged in the contact. This spreads the load over the laminate surface and moves the load closer to the supported edges, in effect stiffening the laminate response to the impact event. This is evident also from the force time history with increasing load. Another observation that may be made is the smoother load curve for higher loads.   At low loading the force time history in particular displays several oscillations on the load curve and becomes more damped as the load is increased.

Peak impact load and displacement increase almost linearly up to the point discussed in the paragraph above, regardless of energy configuration (high mass/low speed and vice versa). Test data also proved to be reproducible, with identical drop heights producing very nearly the same peak loads and displacements. The shape of the load curve replicates very nearly after each drop test.
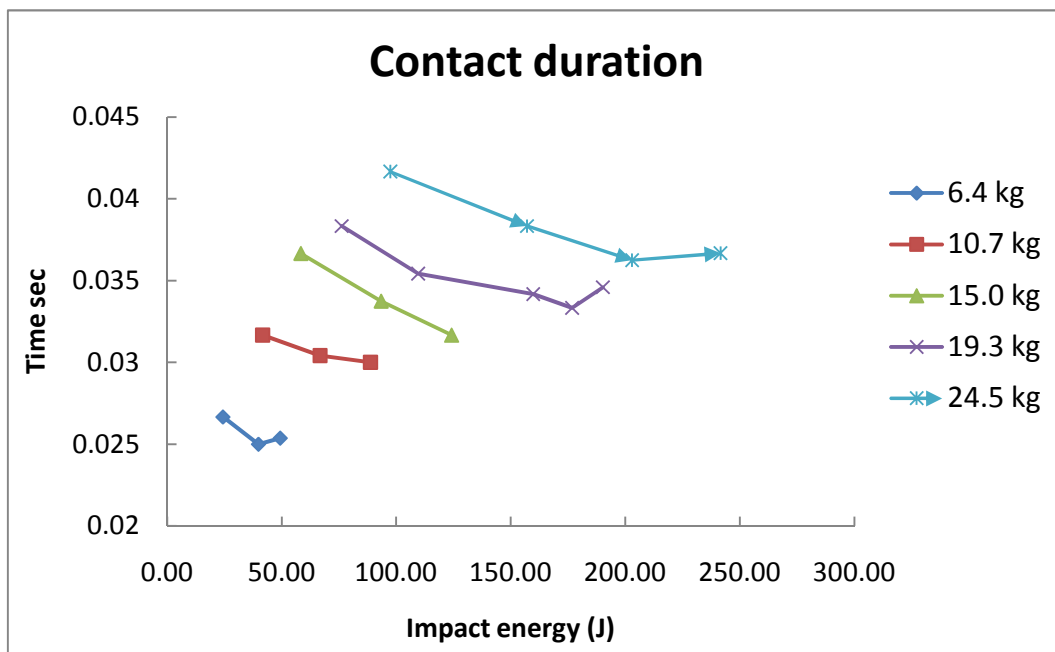

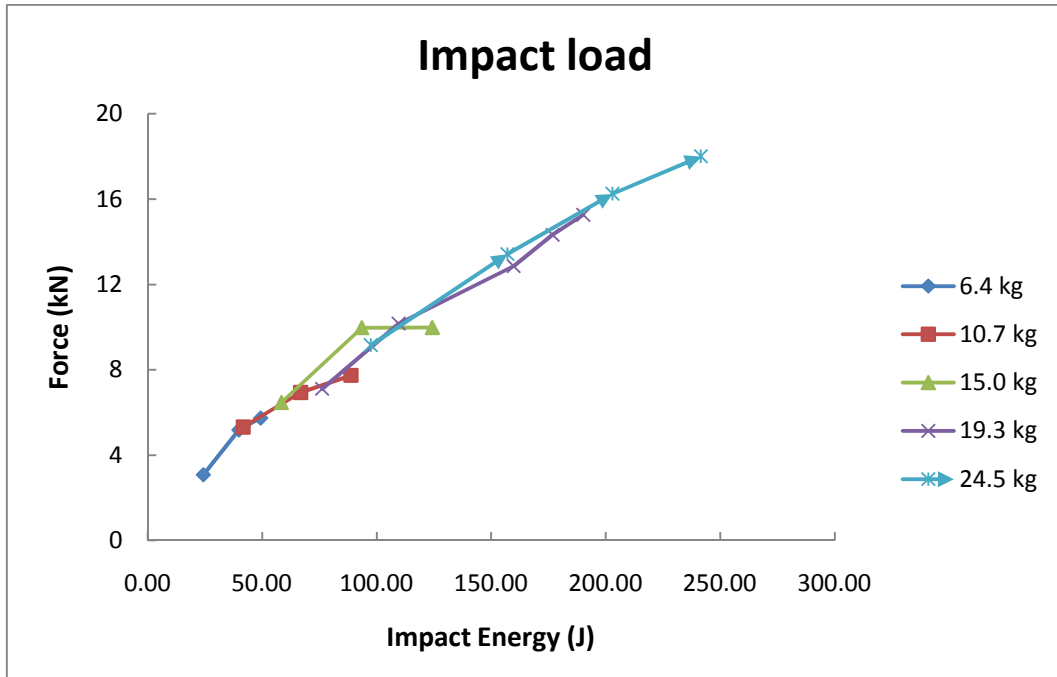Figure 33 Impact duration for combination of impact energies

55

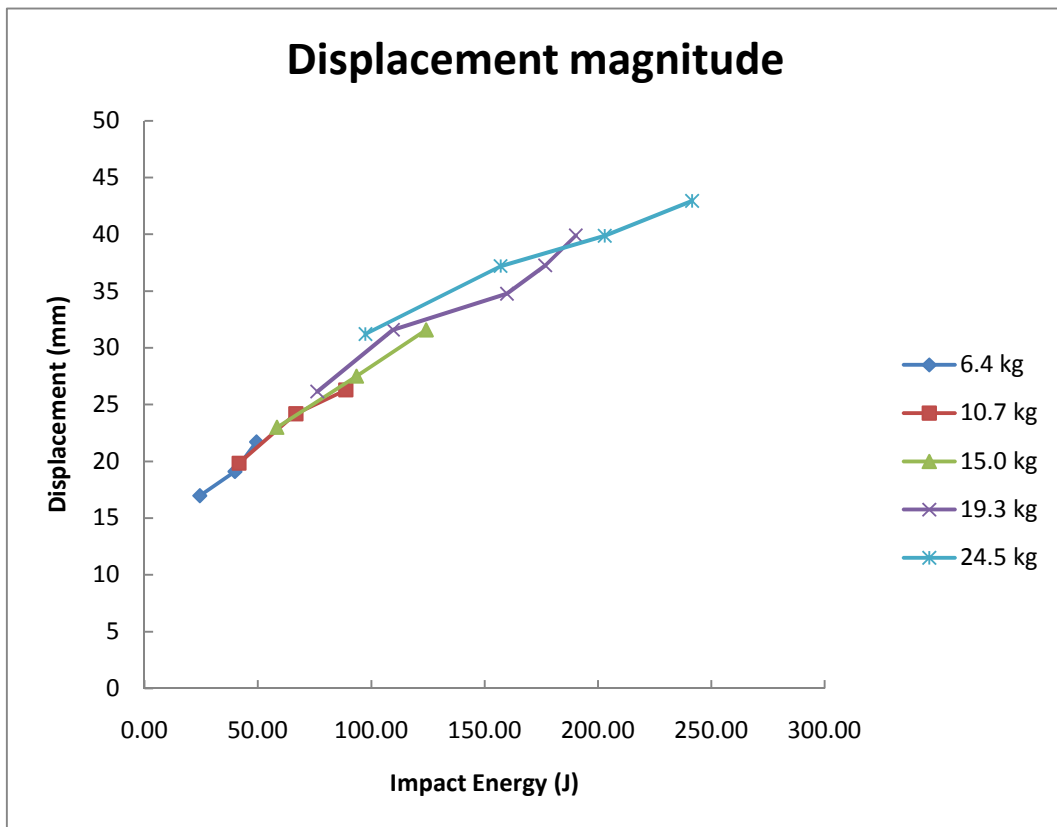Figure 34 Peak load for combination of impact energies

Figure 35 Peak displacement for combination of impact energies

Chapter 8 Correlation

In this section a comparison between each of the model formulations covered in Chapter 2 and the physical test result from Chapter 7 will be performed.

As mentioned in Chapter 3 the impact weights varied between 6.4 kg to 24.5 kg. Table 6 lists the density combination used for the rubber component to simulate the projectile assembly.

Table 6 Projectile model parameter details for the range of impact weights

Component					
Base			Tip		Combined
Volume	Density	Weight	Density	Weight	Weight
	33052.5	6.2304			6.4
	55864.2	10.5304			10.7
0.00019	78675.9	14.8304	1550	0.1696	15
	101488	19.1304			19.3
	129074	24.3304			24.5

It can be shown for all tests that, as in Figure 36 and Figure 37 below, for similar projectile loads (or inertial characteristics), the model (both numerically and physically) follows the same load curve. For this reason only maximum load cases are compared, as it may be assumed that the same comments are relevant to lower load cases not reported.
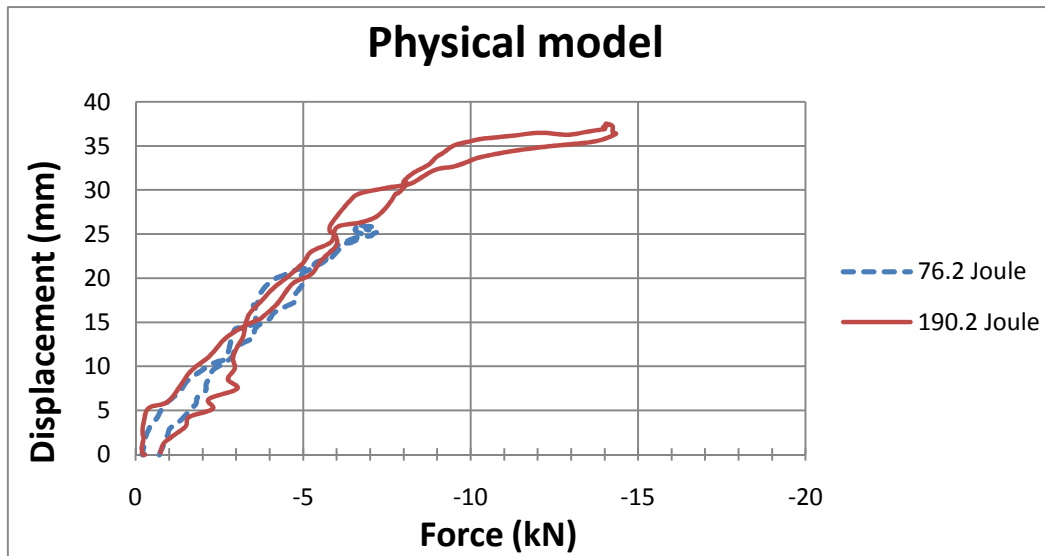

Figure 36 Comparison of impact response of a high and low energy physical impact event
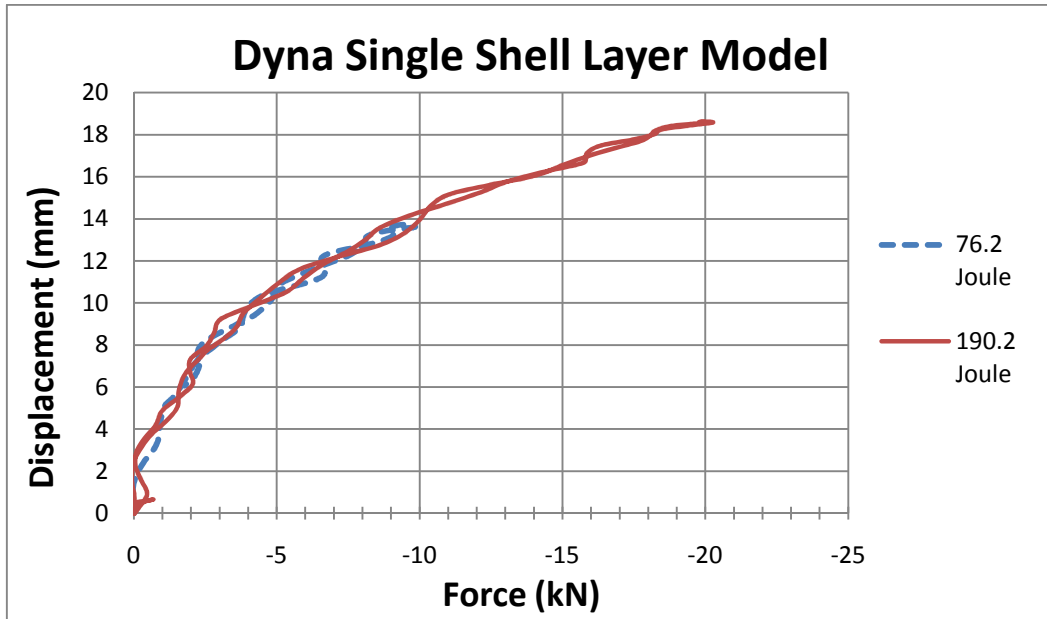
Figure 37 Comparison of impact response of a high and low energy numerical impact event

A summary of the results are displayed in the bar charts below (Figure 38, Figure 39 and Figure 40). For all charts, it can be discerned that the peak loads estimated by the models are too high, the centre displacements too low and the contact duration too short. The variance in result increases with an increase in applied load. Peak loads are overestimated by between 20 – 27 %, peak displacements underestimated by 50 % and contact durations underestimated by 35 – 40 %.
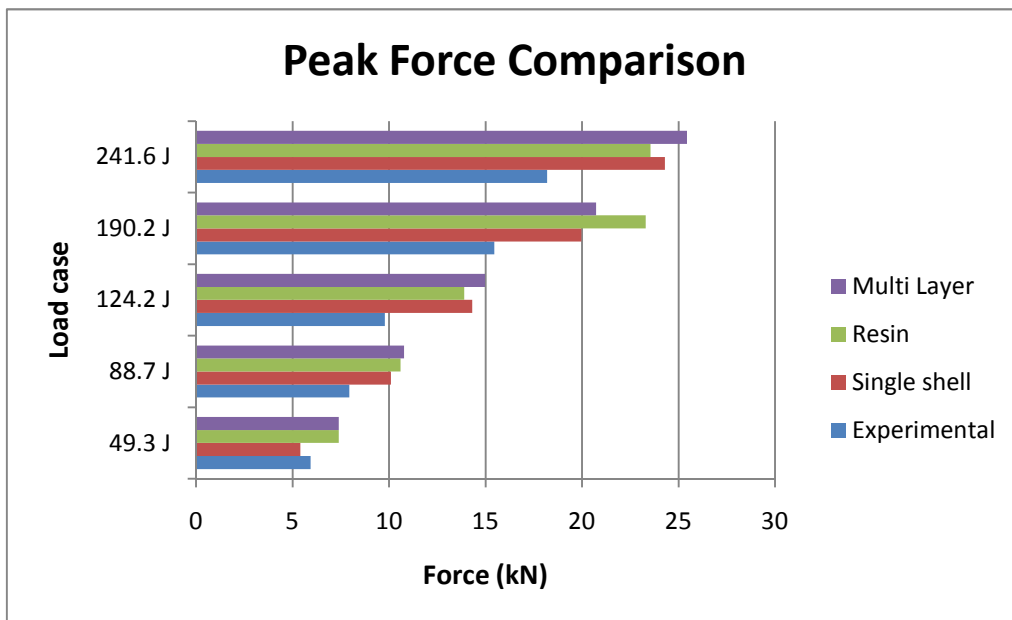

Figure 38 Peak load comparison of all model formulations to physical event for select impact energies
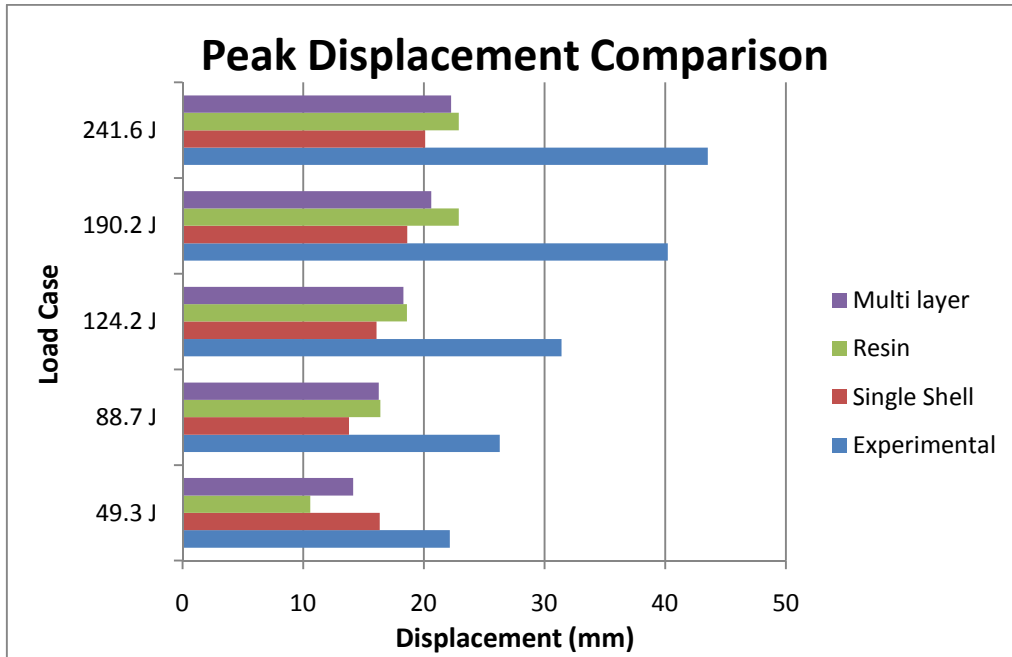
58

Figure 39 Peak displacement comparison of all model formulations to physical event for select impact energies
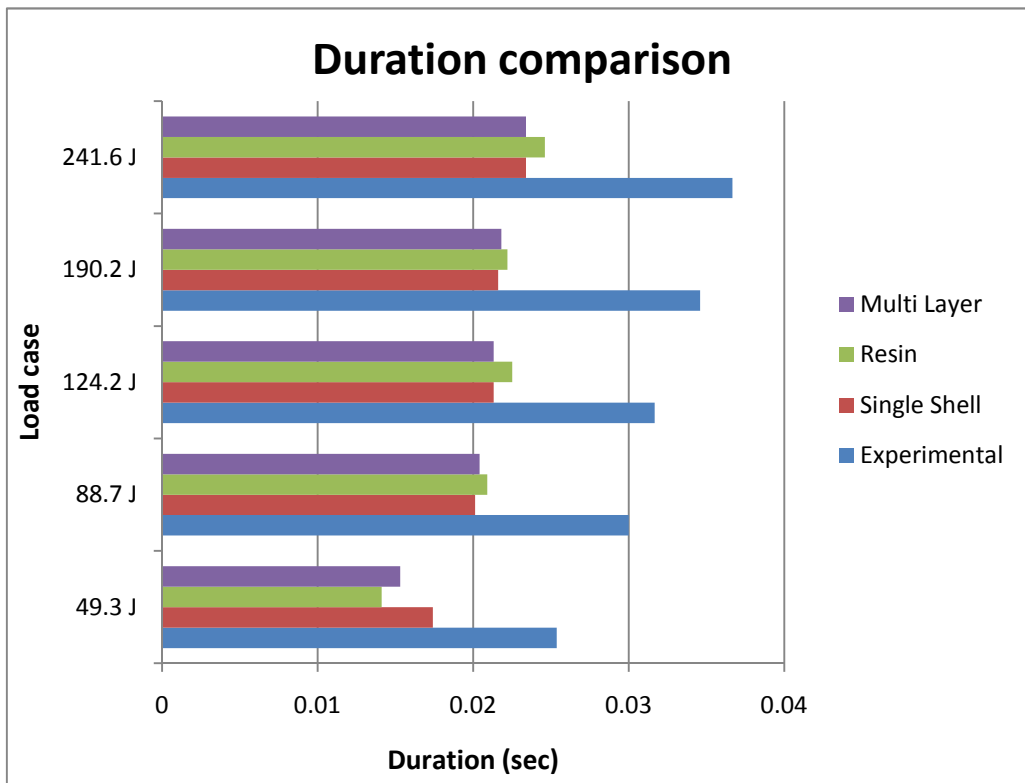

Figure 40 Impact duration comparison of all model formulations to physical event for select impact energies

59

In Figure 41 the energy absorption over impact event duration is displayed. In the case displayed the projectile velocity was 4.44 m/s and the projectile mass was 19.3 kg or 190 J impact. The integration of the experimental data was obtained by simple integration of load cell and displacement data.

The deformation energy in the rubber projectile was not measured, but may be determined when it is considered that the total energy in the system must remain constant. The difference between the input energy and the deformation energy in the composite and its support indicates the amount of deformation energy dissipated in the rubber.

When reviewing the curve from the experimental data, it can be seen that the total energy calculated exceeds the input energy delivered to the projectile. This can be attributed to integration of noise on the measurement signal, and the integration error due to the triangular integration scheme. However, it may be concluded that most of the kinetic energy available was converted into deformation energy in the composite panel and its support structure, while very little has been converted to the deformation of the rubber projectile (although the actual value is unknown).

Numerical energy data was obtained from combining internal energy values of the composite and its support structure. When reviewing the figures it is clear that all the model formulations absorb the same amount of energy in the composite, but too much energy is absorbed by the soft body in the numerical model.
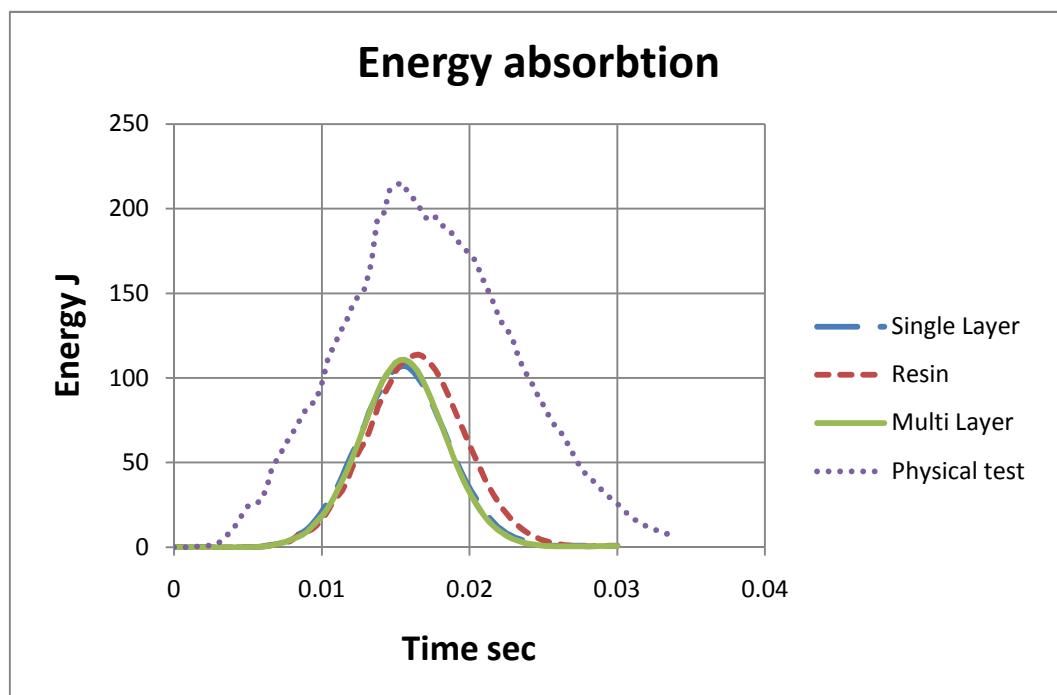

Figure 41 Eneregy absorbtion in the laminate and its support for the numerical models

8.1. Material tests

8.1.1. Composite materials

In an effort to find explanations for discrepancies between the FE model and the numerical data, material tests were performed on composite samples. Samples were cut to 250 mm in length and 20 mm width. These dimensions provide for a tensile segment of 150 mm with 50 mm between the grips in the load frame. Initial tests showed that the samples required instrumentation with an extensometer, as deformation in load frame grips/load cell was excessive and corrupted the measurement.

Remembering that the material is supplied as a layup, the tensile data had to be compared to a calculation for effective modulus in the material 0° (and 90° due to quasi isotropic nature of the weave) direction. The constitutive relationship can be written in short hand form (from Equation 4) as in Equation 37: [6]

$$\begin{bmatrix} N \\ M \end{bmatrix} = \begin{bmatrix} A & B \\ B & D \end{bmatrix} \begin{bmatrix} \varepsilon^0 \\ \kappa \end{bmatrix} \qquad\qquad 37$$

It can be shown that for a symmetrical laminate the effective in-plane longitudinal modulus E_x is given by Equation 38. [6]

$$E_x = \frac{\sigma_x}{\varepsilon_x^0} = \frac{N_x/h}{A_{11}^* N_x} = \frac{1}{h A_{11}^*} \qquad\qquad 38$$

Using Equation 38 and the material datasheets supplied, the in plane effective modulus values can be calculated as:

Table 7 Summary of calculated material properties from material test data

Modulus	Value (GPa)
E_x	37.8
E_y	37.8

Tensile tests (Figure 42) were performed on samples cut to the dimensions in Table 8. Test speeds were varied between 1mm/min and 50 mm/min to give an indication of material sensitivity to strain rate (Table 8). From the data it is clear that within the specified test range the material is not rate sensitive, however this does not necessarily reflect the case at impact level strain rates.

Figure 42 Tensile test setup

Table 8 Summary of tensile test parameters

	Width	Thick-ness	Gage Length	Test Speed	Peak Load	Peak Stress	Peak Strain	Modulus
No.	mm	mm	mm	mm/min	N	MPa	mm/mm	Gpa
1				1	18000	363	0.008	43.8
2				2	18000	363	0.008	43
3	20	2.48	50	4	18002	363	0.008	43.7
4				16	18005	363	0.008	43.2
5				32	18002	363	0.008	43.8
6				50	18029	364	0.008	43.4

Also noteworthy is the fact that the laminate proved to be 20% stiffer than the value calculated from manufacturer test data. Incorporating this finding into the numerical model increased the variance in result when compared to the physical test, as expected.

8.1.2. Material model verification using modal analysis

For the purpose of further composite model material validation, a modal test was done on the flat composite panel. The frequency response of a structure is determined by its mass and stiffness. The mass property of the composite panel can be accurately accounted for, but some uncertainty remained in the simulation of the composite with regards to stiffness. This was especially true for the shear stiffness of the panel. The shear stiffness in the stacked shell numerical model is

determined by the contact algorithms defined between the layers, where the contact stiffness is largely stability driven. The shear behaviour of the composite material models in LS-DYNA is also largely unknown at present (as reported in section 2.5.2.2 and Section 3.6 of [8]) and influences the model stiffness by an unknown amount. This method could also potentially be used to evaluate the resin thickness for the third model formulation.

Using piezoelectric accelerometers a modal test of the composite panel was performed. The panel was suspended by means of elastic bands, one at each corner. This method of support represents a free boundary condition as closely as possible. This is highly advantageous as this is the easiest boundary condition to simulate accurately using finite element codes.

For a start, the panel was instrumented with a single accelerometer and disturbed with a modal hammer. A single accelerometer was first used to ensure minimum influence from the added mass of the accelerometer on the frequency measurement. Using the modal hammer, vibrations died out very quickly and although good measurements were obtained, there was a concern whether enough energy was provided to excite all modes. The decision was made to add a shaker to the test setup. The accelerometer was attached to one corner of the panel, and the shaker was connected by means of super glue to the other. The corners of the panel were deemed the best place for both measurement and excitation as it was unlikely that a node point existed at the corners for the frequencies of interest (mode shapes of flat panels are well recorded in literature).

Test results from the first test did not correspond well to initial FE calculations. To serve as investigatory tool, the mode shapes of the panel were investigated. A measurement bandwidth of 400 Hz was decided upon. At least 4 modes were expected in this region, requiring at least three accelerometers per free edge of the panel to obtain an accurate depiction of the mode shape as explained in Figure 43.

Mode 1:

Mode 2:

Mode 3:

Mode 4:

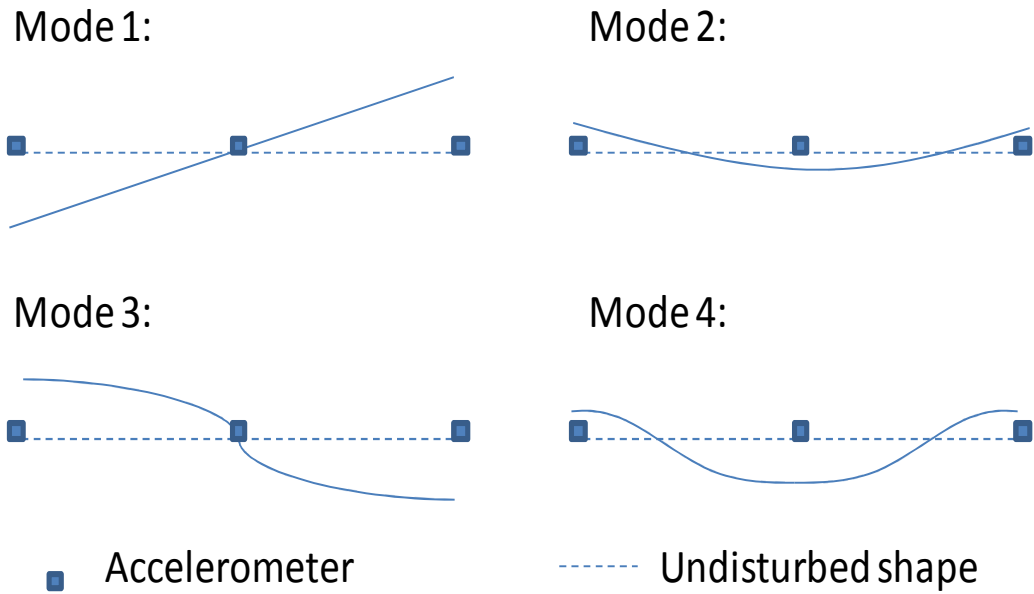◼ Accelerometer   ------ Undisturbed shape

Figure 43 Illustration of mode shapes on laminate and accelerometer positions

For this purpose the panel was instrumented with nine equi-spaced accelerometers. This would have an effect on the frequencies measured during the modal test due to the mass added by the accelerometers. Frequency shift was expected due to the mass of the additional accelerometers added for the mode shape determination. The results thereof are shown in Table 9. Each accelerometer weighed 5 grams, but the accelerometer cable mass is more difficult to account for. The cables add an undetermined amount of mass to the test piece, and they were taped down as close as possible to the composite panel to minimize the effect.

Table 9 Tabulated values from the modal test

Mode	Single accelerometer (Hz)	Nine accelerometers (Hz)
1	75	68
2	140	127
	155	143
3	195	176
		186
4	318	303

Two modal frequencies appeared very close to each other (Figure 44), and these were thought to be symmetric modes, slightly offset by the slight variance in stiffness of the composite weave in the warp and weft direction. This was confirmed upon investigation of the measured mode shapes. The measurement of mode shapes also ensured that the correct modes where compared when evaluating the numerical and physical components.
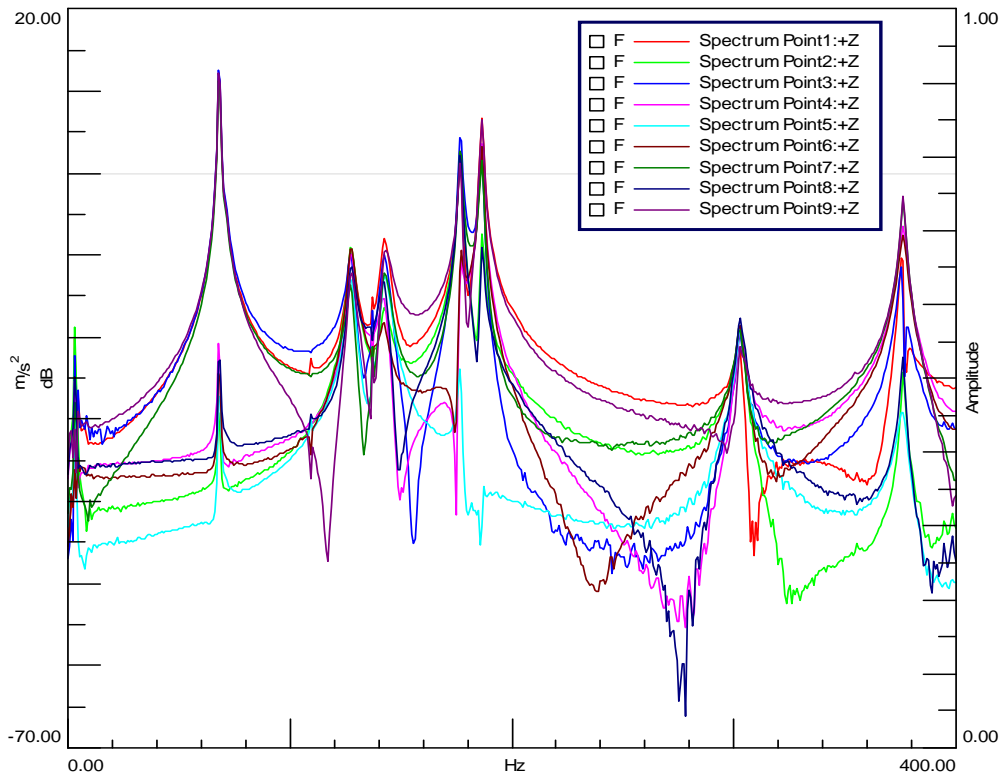

Figure 44 Result from nine accelerometer modal test

65

For the numerical model an implicit simulation and eigenvalue extraction was performed. Model setup works as per normal, but implicit analysis is activated in the control card in LS-DYNA. Some functionality is lost in LS-DYNA when switching from explicit to implicit analysis, as not all functions are supported in this mode of operation. Of specific importance was that material model 58, used in other parts of the project, was not available for implicit analysis. This was however not a cause for concern, as the composite models all use the same constitutive model, only varying in post failure behaviour. Since this was a modal simulation the post failure response of the material was not of interest. Therefore, for the modal test, material model 22 was selected as it was one of the composite models available for implicit analysis.

Initial model setup made use of a decreased amount of elements and were in the single layer format. Element formulation was single integration point elements. This delivered inaccurate results, with several 'mathematical' modes caused by out-of-plane vibration of elements, similar to hourglassing modes (Figure 45). This was remedied by changing to fully integrated elements.
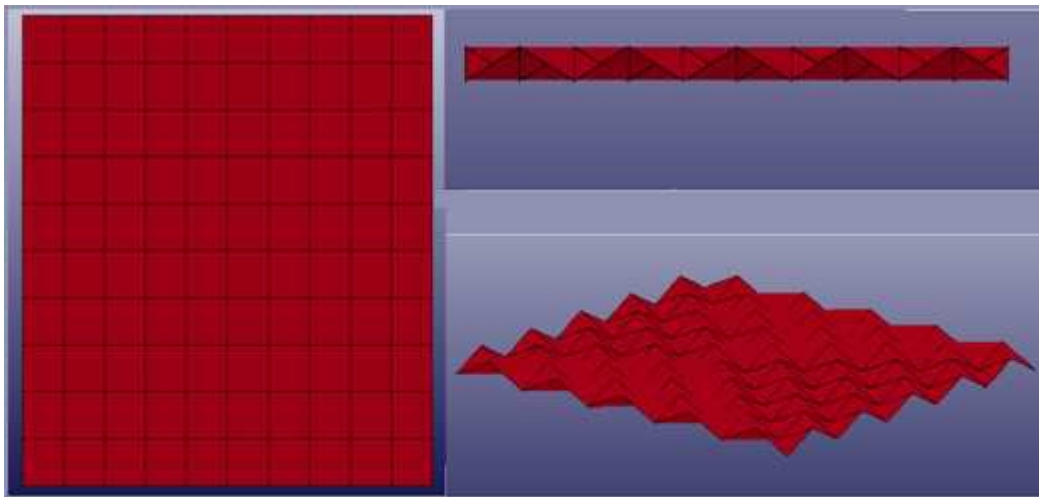

Figure 45 Numerical mode arrising from single integration elements

According to the LS-DYNA theory manual, normal (default) Belytschko-Lin-Tsay shell elements are sensitive to out-of-plane warpage of elements. Both Belytschko-Lin-Tsay and Hughes-Lui elements are reduced integration point shell elements. These elements are reduced to contain one Gauss integration point, as opposed to fully integrated 4 Gauss point integration. This makes the elements computationally less expensive, and therefore are the ones used most. However, single integration points make them susceptible to hourglassing modes.

The fully integrated shell elements were a requirement for the Eigen value extraction (as explained above), but their effect on the explicit models were unknown. The effect of the above mentioned elements were investigated in the explicit model and the results were no different in the pre failure region of the material. However, when a failure load was applied to the simulation, remaining

internal energy in the composite panel was lower when the fully integrated shell elements were used (Figure 46). Therefore, for damage modelling it must be recommended that fully integrated elements be used.
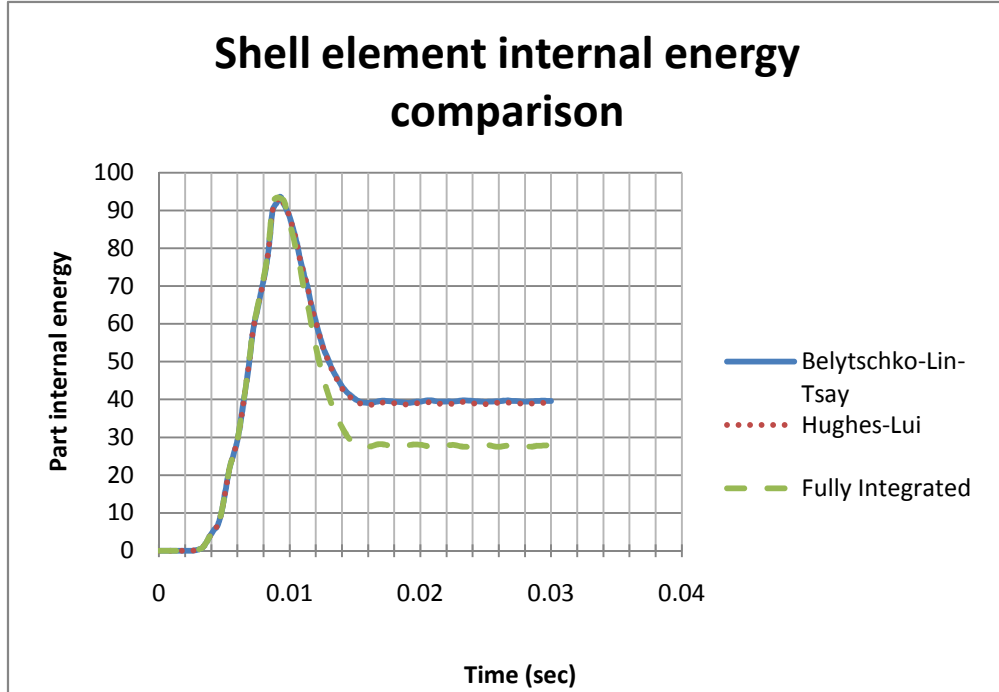

Figure 46 Part internal energy comparison for various shell element formulations

Accounting for the mass of a single accelerometer made a significant difference to the model result. Adding 5 grams (the mass of the accelerometer alone) to one corner of the model dropped the fundamental frequency by 4 Hz. It also caused symmetric modes to split further apart with regards to frequency. If we make the assumption that half of the cable weight of the accelerometer is supported by the composite, this adds another 5 grams to the mass element the fundamental frequency is lowered by another 4 Hz. Another factor affecting the accuracy of the simulation is the eccentricity of the external load applied by the accelerometer and cable combination. This may be accounted for by using the OFFSET_NODE option in LS-DYNA. The results for the single layer model are shown in the Table 10:

Table 10 Eigen value extraction results for the single layer model

Model formulation	No mass	Single accelerometer mass added (Hz)	Accelerometer and cable mass added (Hz)	Single accelerometer physical test (Hz)
Mode 1	93	89	85	75
Mode 2	108	108	108	140
				155
Mode 3	180	167	160	195
Mode 4	226	212	208	318

The numerical model proved to be too stiff in the case of the single layer shell model. This is in contrast with the material tests which show that the material stiffness should be increased from the manufacturer data. However, the model being too stiff does agree with numerical models that are too stiff when compared to the physical drop test result. The mode shapes did show good correlation for the first, second and fourth modes (Figure 47 and Figure 48).
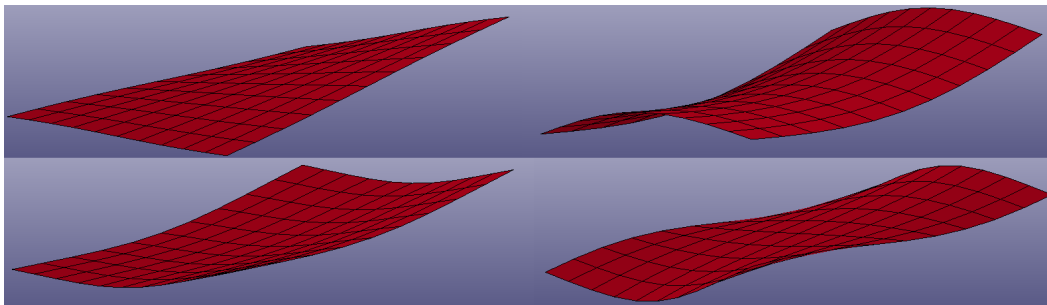

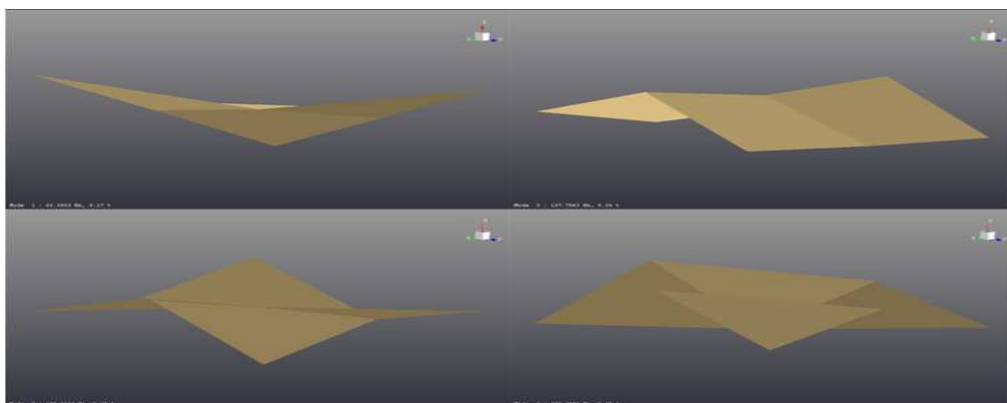Figure 47 First four mode shapes calculated numerically

Figure 48 First four structural modes obtained from the modal analysis

Difficulty was encountered when attempting an Eigen value extraction on the stacked shell model. Elements did not remain in contact regardless of changes to distances between layers (Figure 49). In an attempt to remedy the problem, contact thickness was changed, shell thickness (on the contact card), penalty stiffness and the physical offset was adjusted but without a change in result. Faulty Eigen values where then calculated as the highest stiffness in the model was that of a single layer.

The Eigen value extraction of the resin model was completed, and some details were discussed in an earlier section. The Eigen value result and comparison with the extracted modal frequencies could be very useful in this case, as the thickness of the resin can be gauged from the stiffness of the panel. However, as discussed earlier, some illogical results were obtained with variance in the resin integration point thickness.
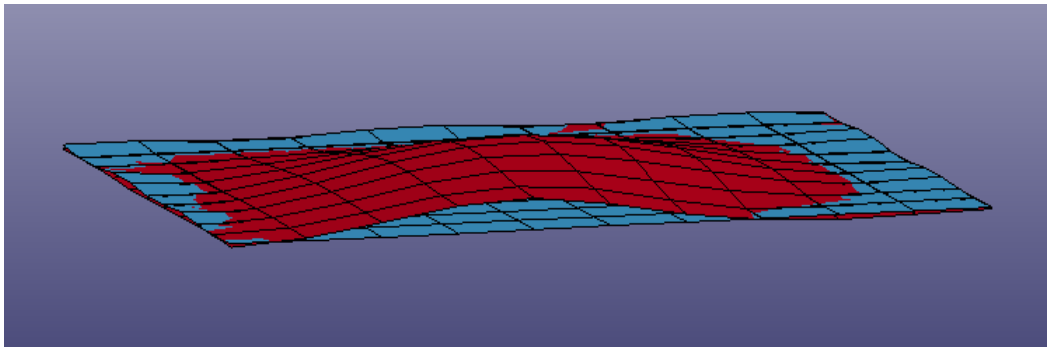

Figure 49 Tied contact failure for eigen value extraction of stacked shell model

From the single shell layer solution however, it may be concluded that the numerical model is too stiff, with factors further reaching than the shell formulation, material property and density assigned and serves to some extent to explain the variance in result between the explicit FE solution and the physical drop test.

8.2. Comparison of failure pattern

One of the advantages of using MAT_058 lies in the more advanced treatment of composite failure. The failure criteria for the failure model was discussed in detail in an earlier section, the practical application will now be reviewed.

For MAT_058, the user may select to write additional history variables to the database predominantly regarding failure parameters of the model. These parameters are listed in Table 11 and may be checked using LS PrePost.

Table 11 LS PrePost history variables for MAT_058

Var #	Significance		Var #	Significance
1	damage in fibre direction		8	total failure
2	damage in matrix direction		9	threshold failure value rs
3	damage in shear		10	local strain a-direction
4	threshold failure value r1		11	local strain b-direction
5	threshold failure value r2		12	local shear strain
6	material direction cosine		13	effective strain
7	material direction sinus			

For a laminated composite, parameter 1 refers to damage in the 0° direction and parameter 2 refers to the 90° direction (as opposed to fibre/matrix directions). The damage state of an element changes once the stress in the element falls outside the failure criteria, upon which the constitutive model is adapted as in the Equation 17 below (repeated for convenience)**:**

$$
\begin{aligned}
&C(\omega) \\
&= \frac{1}{D}\begin{pmatrix} (1-\omega_{11})E_{||} & (1-\omega_{11})(1-\omega_{22})v_{21}E_{\perp} & 0 \\ (1-\omega_{11})(1-\omega_{22})v_{12}E_{||} & (1-\omega_{22})E_{\perp} & 0 \\ 0 & 0 & D(1-\omega_{12})G \end{pmatrix}
\end{aligned}
\qquad 17
$$

The constitutive Equation is scaled because only the undamaged part of the cross section can carry load. Once the damage parameter ω reaches unity for the whole element, the element is deleted.

Damage detection on the physical composite panel was unfortunately limited to visual inspection and tap tests. Two other methods of damage detection were attempted. The first method involved radiating one side of the panel with an infrared heating element and inspecting the top side with an infrared gun in a dark room. This method was not successful regardless of heating time and the resolution of the FLIR camera was believed to be the limiting factor. The second method involved placing an array of accelerometers on the panel. The panel was then placed on a shaker instrumented with a load cell. The transfer function for each accelerometer was compared to that of a test done on an undamaged panel, but results were not clear enough to make any proper conclusions. However, both of these methods show promise with further development, with the thermography approach popular with advanced users in the industry.

Visual inspection revealed damage in two areas after high load applications (243 Joule) on the flat panel. The first area of damage was through the thickness

near the impact region o

panel and contact betwe

be reflected in the num

mid span of the panel a

top layer of the target,

the panel. The damaged

All three numerical m

mentioned load case. A

surfaces of the laminate

the damage apparent by

1 and 8 are most import
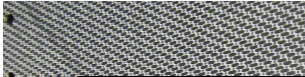

Figu

For the single layer mo

the thickness at that inte

the clamped area, where

predicted transverse fail

the physical panel, whe

pass underneath. A val

same direction as ω_2 fo

damage predicted on the

by inspection however.

Table 12 Summary of damage parameter values on top and bottom surfaces of the laminate

Model	Damage variable ω	Integration point/Composite Layer	Parameter value	Location
Single Layer	1	1	0.0013	Centre
		8	0.1957	Centre
	2	1	0.113	Outer edge
		8	0.1	Centre
	3	1	4.80E-05	Outer edge
		8	6.20E-05	Centre
Resin	1	1	3.30E-04	Outer edge
		15	0.16	Centre
	2	1	0.06	Outer edge
		15	0.09	Centre
	3	1	2.50E-05	Outer edge
		15	3.70E-05	Centre
Stacked shell	1	Top	1.80E-05	Centre
		Bottom	6.20E-04	Centre
	2	Top	0.128	Near centre
		Bottom	0.02	Near centre
	3	Top	4.80E-05	Near centre
		Bottom	8.10E-06	Near centre
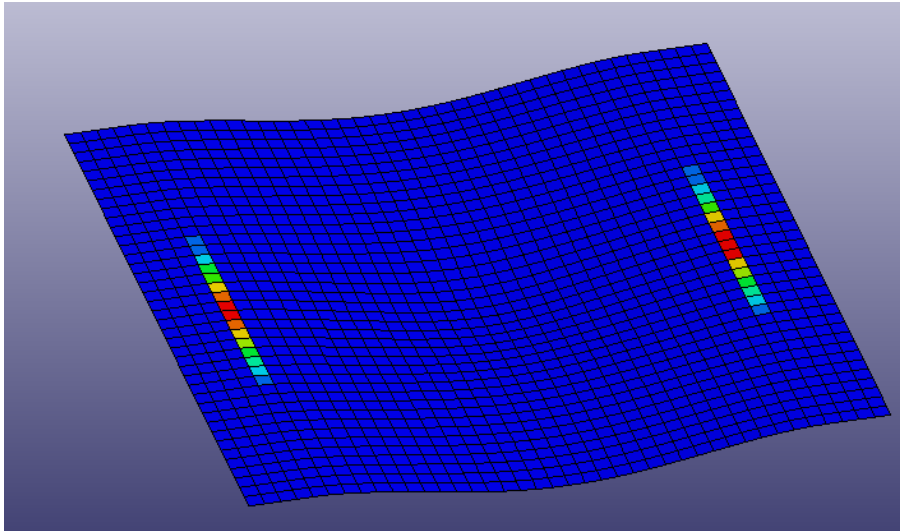
Figure 51 Damage predicted for the 22 direction, single layer model

The resin model exhibits some of the same prediction patterns as the single layer model, but the damage parameter values corresponding to the identified physical damage regions above are much lower. Higher damage parameter values are reported internally but these are difficult to validate using the current inspection techniques (Figure 52).

Figure 52 High failure parameter values reported for resin model on mid plane layers

73

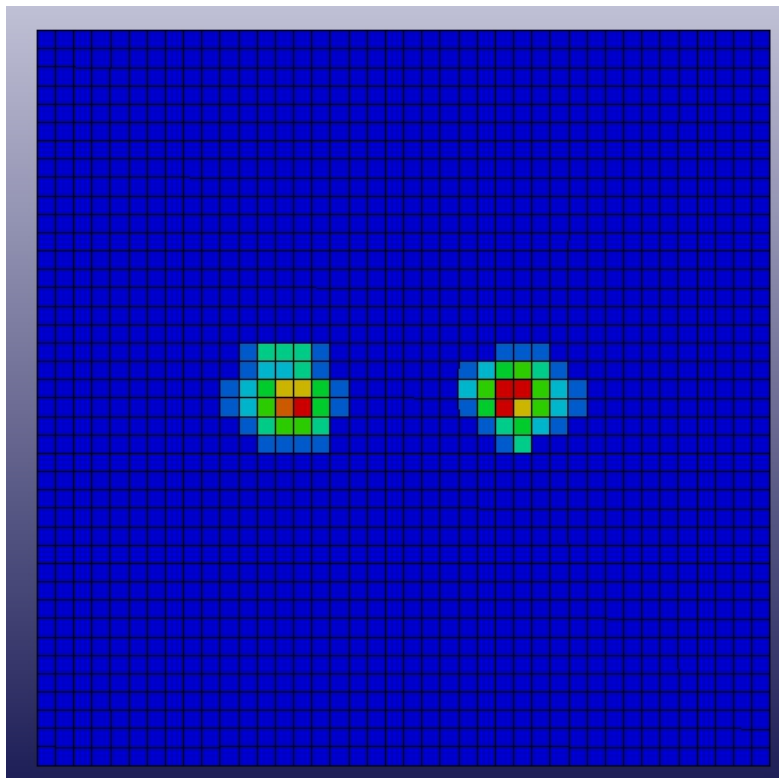Highest damage parameters for the stacked shell model were recorded in the interior region for most layers. Some results contained single elements with comparatively high levels of damage (as shown in Figure 53), believed to be caused by the contact algorithm between the layers.
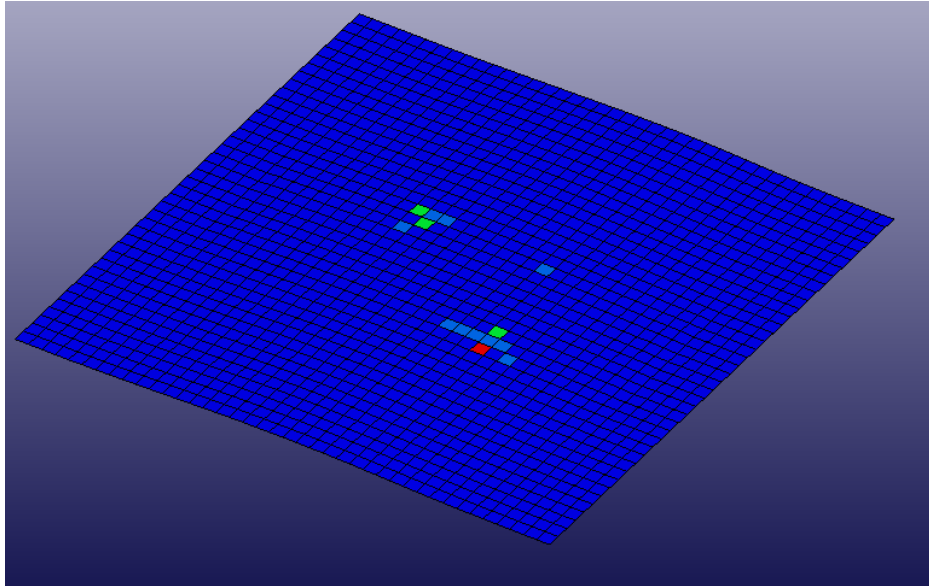

Figure 53 High damage parameters reported due to contact forces in stacked shell model

A valuable conclusion can only be drawn from a comparison of visual damage to the values predicted by the models on the upper and lower surfaces of the target laminate. In this regard the single layer model outperformed the other two model formulations. The single layer model was the only model to predict significant levels of damage to the upper outer edges of the composite panel. The reader must bear in mind that although delamination was unlikely for this load case, the single layer formulation offers no accurate method of evaluating whether delamination has occurred in the test panel. Only in plane failure phenomena can be evaluated. The case may be that the other models predict internal damage with higher accuracy, but at this stage this cannot be confirmed without more advanced detection techniques. Uncertainties with inter layer contact stiffness in the stacked shell model does not create a solid foundation for conclusions regarding delamination failure.

Chapter 9 Curved laminate

As discussed in Chapter 5 a curved laminate was produced to investigate the ease of forming the thermoplastic material. The curved laminate was also subjected to an impact test, although not a complete study as is the case with the flat laminate. The procedure is discussed in this section.

9.1. Drop test

The carriage configuration for the curved laminate was the same as for the flat panel laminate as explained in Chapter 3. There was however a change to the support structure to support the angle of the curved laminate. The adapted support assembly is shown in Figure 54.

Figure 54 Adapted support assembly for curved laminate

The position of velocity measurement was also moved up to ensure that the measurement is still taken just before impact. It was expected that the composite panel would snap through and therefore it was elected to remove the LVDT to prevent equipment damage.

9.2. Key model variations

The modelling procedure for the curved laminate was very similar to the procedure followed for the flat laminates. The geometry of the model was adapted to represent the curved target panel. An assumption was made that the geometry of the laminate and the die used in the pressing procedure was identical (and that the geometric differences did not influence the model). The geometry of

the laminate was taken directly from the drawings created for the die used in the pressing operation.

For both the single layer shell representation and the stacked shell model the radius of curvature was taken to be 400 mm (shown in Figure 55). In the case of the stacked shell model, this curved shell layer was offset 8 times (for 8 layers) by the lamina thickness (0.31 mm). Although the physical panel has a different radius of curvature on the top and bottom layers it was assumed that the effect thereof was negligible.
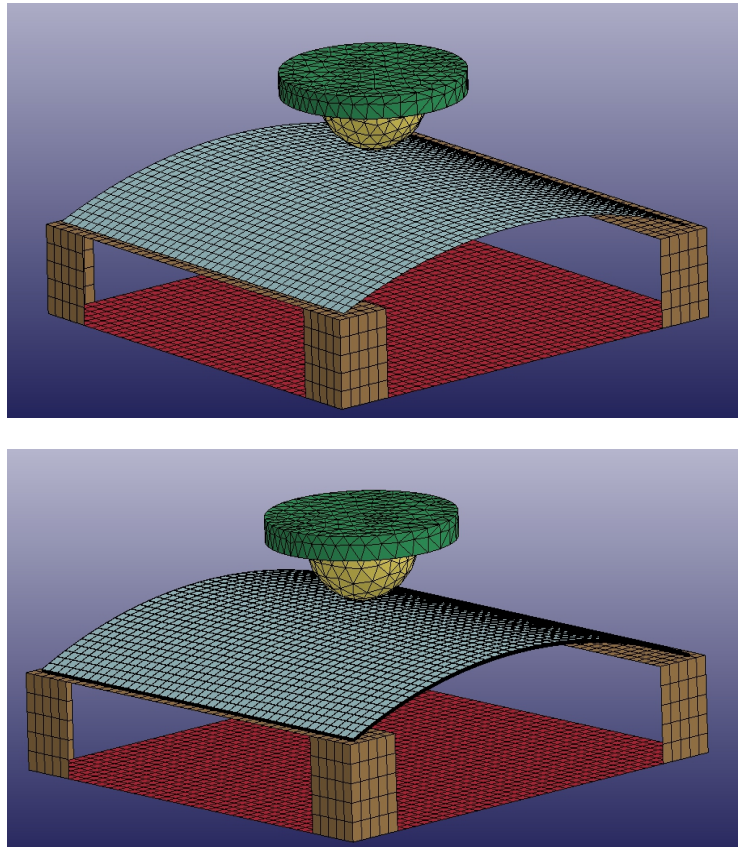

Figure 55 Curved laminate models: The single layer representation above and the stacked shell representation below

Numerical instability was encountered with the stacked shell representation. The problem was found to be the contact interface stiffness k_i. The contact interface stiffness used initially was taken from the flat panel laminate, but had to be scaled down to ensure that the model remained stable. The user controlled parameter f_{si} could not be set to a value higher than 0.1. This further added to the issues brought forth in Section 6.2 regarding insufficient inter laminar stiffness.

9.3. Results

Two events were compared in the case of the curved laminate. A light impact of 42 Joules and a higher impact load of 159 Joules. The 42 Joule impact was achieved by using the empty 6.4 kg trolley and an impact velocity of 3.64 m/s, while the 159 Joule impact was achieved by a trolley weight of 19.3 kg and a velocity of 4.06 m/s.

The force time curves for two evaluated impacts are shown in FiguresFigure 56 andFigure 57. The results of the numerical models do not successfully capture the result of the experimental result taken at the load cell. The experimental result contained much more oscillations in the lower load case, where snap through (a non linear response due to target geometry) was not present for both physical panels and the numerical simulations. For the higher load case where snap through did occur, the force oscillation was excessively present in the numerical models as apparent in Figure 57.

For the stacked shell model the lack of inter laminar stiffness was apparent. This is most easily witnessed by the force trace in Figure 56, where the laminate is only resisting movement of the impactor a few milliseconds after initial contact. This observation suggests that this lack of interlaminar stiffness has a far greater influence during compressive and shear loading during the initial phase of the impact.

On the physical panel damage was observed at the clamping region caused by excessive bending (as in Figures 64 and 65 in Appendix E) and in the central region on the non impact side of the laminate. The damage near the clamping region was predicted by all models on the top layer of the laminate. The stacked shell model experienced complete failure on the upper level of the laminate in this region and the residual strength in the remaining layers was insufficient to curb further displacement of the projectile, causing catastrophic failure of the target panel (Figure 66 in Appendix E). The residual strength in the single element layer models was sufficient as maximum damage parameter values $\omega_1 = 0.9$ and $\omega_2 = 0.9$ were recorded (high parameter values shown in Figures 67 and 68 in Appendix E).

Damage in the central region was not reported with high damage parameter values by any of the models (although isolated elements in the single layer model showed high damage parameter levels, Figure 68 in Appendix E). The resin model allowed for the evaluation of stresses in the resin only areas between the composite layers. Stresses in the resin layers were significantly lower than in the composite layers. This may be explained by the fact that the strain field is continuous and the stiffness of the resin is much lower than that of the laminate. It seems unlikely that this method could be used to predict the central region delamination observed in this test case.
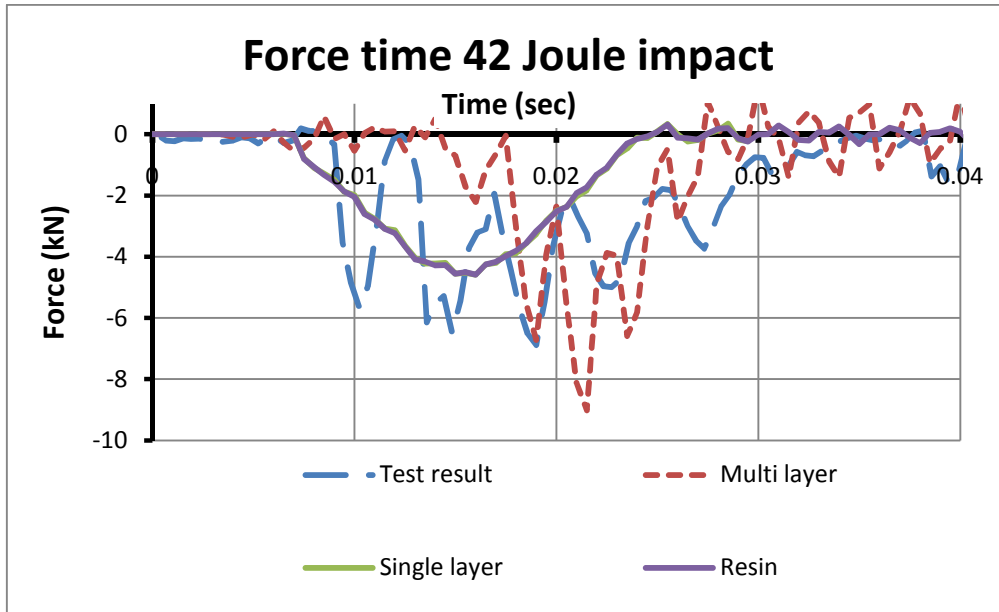
Figure 56 Force time curve for 42 Joule impact. Note the delayed force response from the stacked shell model. The numerical curves are aligned so that the point of impact coincides with the first rise in force from the experimental result
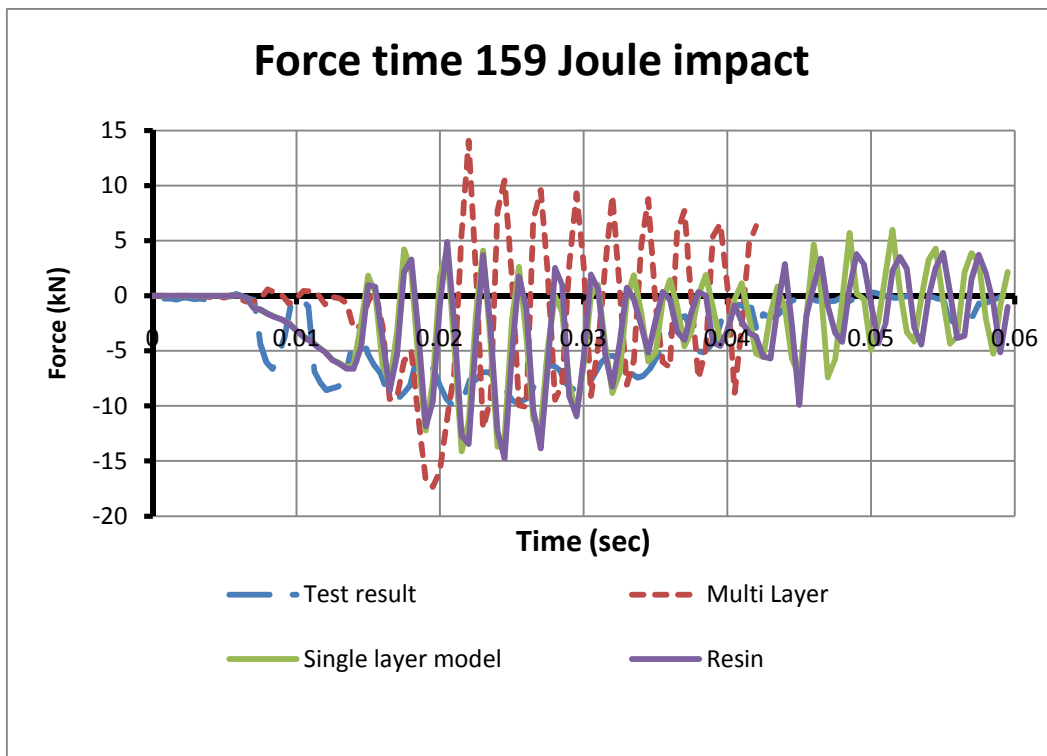

Figure 57 Force time curve for 159 Joule impact. The Stacked shell curve is plotted up to catastrophic failure.

78

Chapter 10 Future work and improvements

Upon review of the results some improvements to the project could be identified as well as many opportunities for future research. These points will be discussed in this section.

The largest improvement to this project could be made in the way the impact load is applied and modelled. Therefore, the first component to be addressed in this project would be to remove the uncertainty resulting from the rubber component. The modelling of the rubber component should be investigated in its own right and a comprehensive test procedure evaluating effects of sample geometry and deformation rates should be performed. In order to evaluate material characteristics, the current study evaluated a cylindrical test piece, 45 mm in length and 50 mm diameter, tested at speeds of 0.5 mm/s to 60 mm/s. The next step would be to investigate a range of aspect ratios and higher strain rates to evaluate further strain rate and geometry effects.

The trolley mounted projectile is not an ideal load application. The deformation of the trolley adds inertial effects which have to be accounted for in the numerical model in some way. The ideal approach would be to change the setup to have a smaller trolley (challenging to achieve if the current drop tower is to be used) or eliminate the trolley all together. This could be done by dropping or firing a high mass rubber projectile at the target, making sure that the impact zone is well defined. Other material models available in LS-DYNA could also be experimented with, even though Blatz-Ko rubber model was termed appropriate for PU rubber.

A further consideration is the mounting of the composite target. The mounting method as used for the flat panels currently is not an ideal method for the evaluation of delamination failure and should be changed if delamination in particular is the failure mode under consideration. This could be achieved by clamping the target circumferentially, allowing for very little deformation in bending (the failure mode dominant in the current flat panel configuration) and allowing the target to delaminate.

Further research should also include more advanced damage detection techniques, especially if delamination forms part of the core focus. Thermographic techniques for instance will allow for the quantification of internal damage to the composite if properly applied.

Although delamination failure could not be captured successfully with the modelling methods applied, more research should be done before the possibility of using only shell elements for this purpose is ruled out. For the stacked shell

approach (possibly the model most likely to predict accurate delamination), other ways of connecting lamina should be considered. One option could be to place Spot Weld elements between nodes or even use thick shell elements for other formulations.

Once the above mentioned improvements have been applied, research could extend into:

- Investigation of lay ups and the effect on out-of-plane impact strength (this has been studied by some research institutes, but not for low speed soft body impacts).
- Comparison of various thermoplastic resins with regards to impact strength, and a further comparison to thermosetting Epoxy resins. Such a study could favourably influence the use of thermoplastic composites for structural components in industry.
- Include more complex target geometries.
- Include an evaluation of LS-DYNA MAT_161 and MAT_162. These material models are purchasable from MSC and include several enhancements over MAT_058 regarding the failure behaviour of composite materials.
- Higher impact velocities could also be considered to evaluate through thickness stress wave effects on the laminate. This would be particularly difficult with shell elements but has been done by others with solid elements to fibre level in literature. [26]

Chapter 11 Conclusion

A thermoplastic composite material was successfully subjected to an impact load from a soft bodied projectile. Load and displacement data were recorded for this event and compared to numerical models.

Curved laminates were also required for impact testing. Additionally, this was an opportunity to demonstrate the reduced cycle times possible with thermoplastic materials, a major advantage in the manufacturing environment. These panels were successfully formed and it was possible to produce a single curvature laminate with a cycle time of less than 5 minutes.

The aim was to attempt modelling the complete response (including failure) of the composite panels using only shell elements. Three methods of modelling the laminates with the use of shell elements were evaluated. The geometry and nature of the projectile necessitated solid elements however. The models were compared to the physical test result with regards to target response and failure.

When the numerical results from the models were compared to the results from the physical event, some discrepancies were encountered. The composite panel deformed more in the physical event than in the model, resulting in lower peak loads and longer contact durations. Investigation of the data revealed that this could be attributed to the fact that the rubber in the numerical model absorbs more deformation energy than in the physical case. A more accurate rubber model would be required for further research and may warrant a study on its own.

Further investigation revealed variance in panel stiffness when a modal test was performed where the numerical model was stiffer than the physical laminate. As a further investigation, manufacturer material properties were evaluated and the panel was found to be even stiffer than the manufacturer quoted, seeming to contradict the result of the modal test. The main reason for this contradiction was reasoned to be the uncertain non-linear shear behaviour of composite materials and the effect thereof on the Eigen value extraction.

A key parameter found to be problematic with the stacked shell model was the contact stiffness between the element layers. The default value used in the contact algorithm was found to be too compliant for the intended use and the upper value thereof was bound by model stability. Attempts at remedying the problem soon rendered the model impractical when the available benefit was compared to computational cost.

For the resin model, the user controlled resin thickness had to be determined. The numerical model did not seem to be sensitive when evaluated with the out-of-plane impact load, but problems were encountered when a modal analysis was performed to confirm panel stiffness. The resin model exhibited unexpected

numerical behaviour, where a very (1e-7 m) thin resin layer would lower the fundamental frequency of the laminate near zero Hz.

In-plane failure was predicted with some success by the standard and resin model formulations. The stacked shell model however did not predict in-plane failure with sufficient accuracy. Delamination failure was not successfully predicted by either model. Some recommendations regarding improvements of the project was made before the suggested modelling strategies could be regarded as unsuitable for complete laminate response prediction.

References

[1.   Abrate, S., *Impact on Composite Structures*. 2005: Cambridge University Press.

2.   Iannucci, L., *Progressive failure modelling of woven carbon composite under impact.* International Journal of Impact Engineering, 2004. **32**: p. 1013-1043.

3.   Sagar P. Rajbhandari, M.L.S., Rodney S. Thomson, Dieter Hachenberg, *An approach to modelling and predicting impact damage in comoposite structures.* ICAS 2002 Congress, 2002.

4.   Campbell, F.C., *Manufacturing processes for advanced composites.* 2003.

5.   Favaloro, M., *Continuous reinforced thermoplastic composites for aircraft applications.* Ticona Engineering Polymers.

6.   Kaw, A.K., *Mechanics of Composite Materials, Second Edition*. 2006: New-York.

7.   A. Matzenmiller, J.L., R.L. Taylor, *A constitutive model for anistropic damage in fiber-composites.* Mechanics of Materials 20 (1995), 1994: p. 125-152.

8.   K. Schweizerhof, K.W., Th. Munz, Th. Rottner, *Crashworthiness Analysis with Enhanced Composite Material Models in LS-DYNA - Merits and Limits.*

9.   Tsai, S.W. and E.M. Wu, *A general theory of strength for anisotropic materials.* Journal of composite materials, 1971. **5**(1): p. 58-80.

10.   Schwartz, R.T., H.S. Schwartz, and D. United States. Air Force Materials Laboratory, Ohio. Nonmetallic Materials Division, *Fundamental aspects of fiber reinforced plastic composites*. 1968: Interscience Publishers.

11.   Hashin, Z., *Failure criteria for unidirectional fiber composites.* Journal of applied mechanics, 1980. **47**: p. 329.

12.   Chang, F.K. and K.Y. Chang, *A progressive damage model for laminated composites containing stress concentrations.* Journal of Composite Materials, 1987. **21**(9): p. 834-855.

13.   Xiaodong, T., et al., *Methodology for residual strength of damaged laminated composites*, in *Archive Set 638*. 1963, American Institute of Aeronautics and Astronautics.

14.   Zhang, X., *Impact damage in composite aircraft structures-experimental testing and numerical simulation.* Proceedings of the Institution of Mechanical Engineers, Part G: Journal of Aerospace Engineering, 1998. **212**(4): p. 245-259.

15.   L. Iannucci, M.L.W., *An energy based damage mechanics approach to modelling impact onto woven composite materials - Part 1: Numerical models.* Composites: Part A 37 (2006), 2005: p. 2041-2056.

16.   Vaziri, R., M. Olson, and D. Anderson, *Finite element analysis of fibrous composite structures: a plasticity approach.* Computers & structures, 1992. **44**(1): p. 103-116.

17.   Kachanov, L.M., *Rupture time under creep conditions.* International journal of fracture, 1999. **97**(1): p. 11-18.

18.   Rabotnov, Y.N. *Creep rupture*. in *Proceedings of the XII international congress on applied mechanics*. 1968.

19.   Frantziskonis, G., *Distributed damage in composites, theory and verification.* Composite structures, 1988. **10**(2): p. 165-184.

20.   corporation, L.s., *LS-DYNA theory manual*. 2003.

21.   Van Hoof, J., et al. *Effects of post-failure modelling on the response of ballistically impacted composites*. in *Proc. 11th Int. Conf. on Composite Materials*. 1999.
22.   Iranthi M. Meththananda, S.P., Mangala P. Patel, Michael Braden, *The relationship between Shore hardness of elastomeric dental materials and Young's modulus.* Dental Materials, 2008. **25**: p. 956-959.
23.   Gent, A., *On the relation between indentation hardness and Young's modulus.* Rubber Chemistry and Technology, 1958. **31**(4): p. 896-906.
24.   Blatz, P.J. and W.L. Ko, *Application of finite elastic theory to the deformation of rubbery materials.* Transactions of the Society of Rheology, 1962. **6**(1): p. 223-251.
25.   corporation, L.s., *LS-DYNA Keyword manual.* 2006.
26.   Duan, Y., et al., *Finite element modeling of transverse impact on a ballistic fabric.* International journal of mechanical sciences, 2006. **48**(1): p. 33-43.

Appendix A. Rubber test data

One Hz displacement data

Ten Hz displacement data
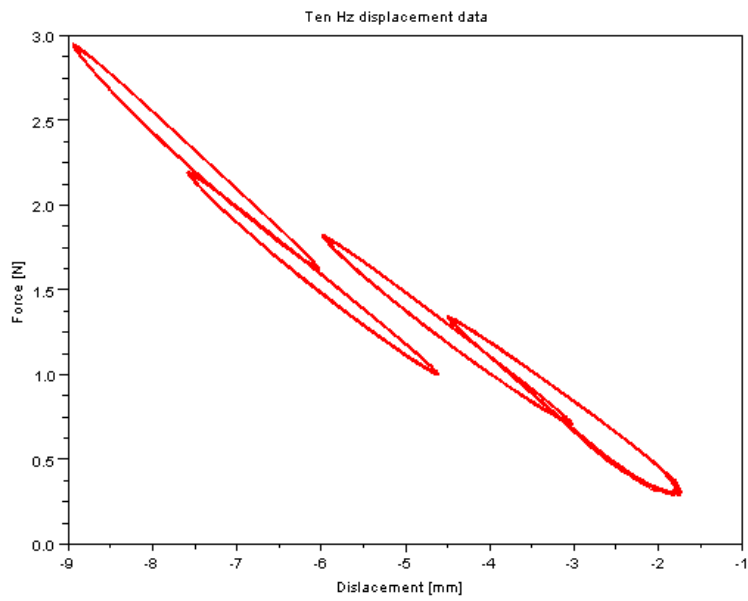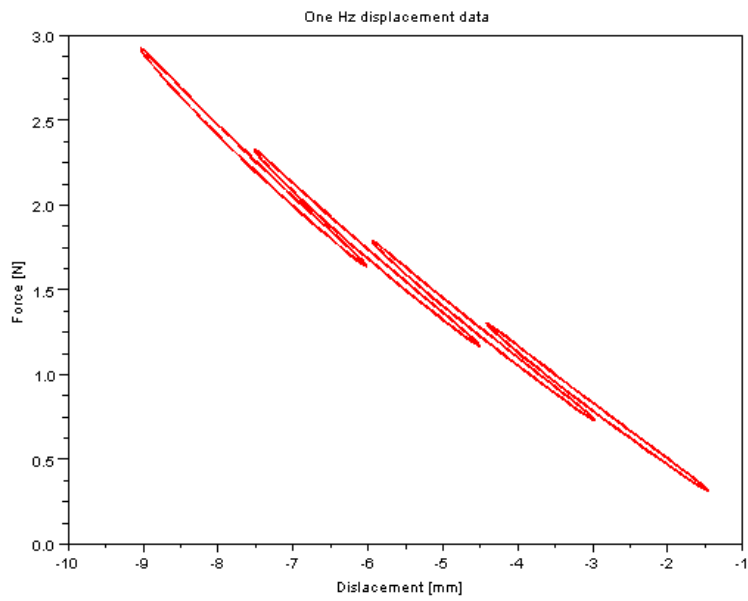
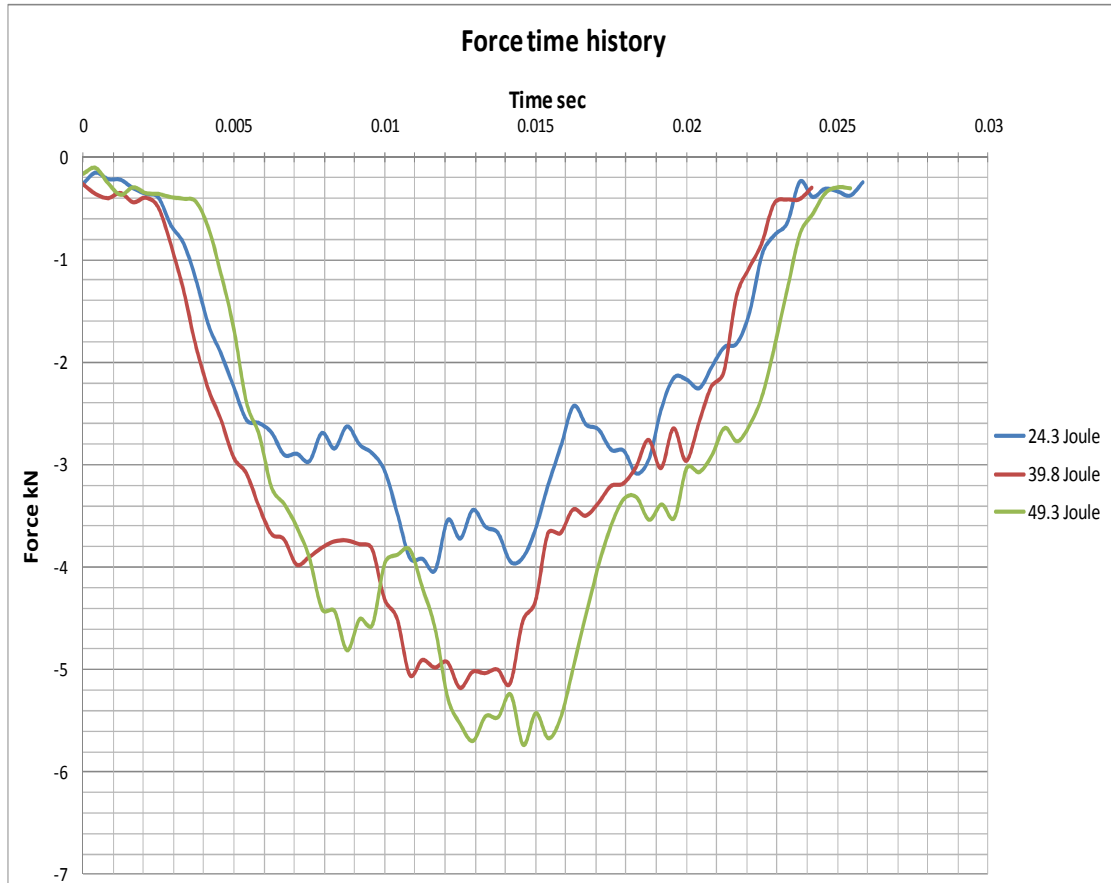# Appendix B. Selected force time data
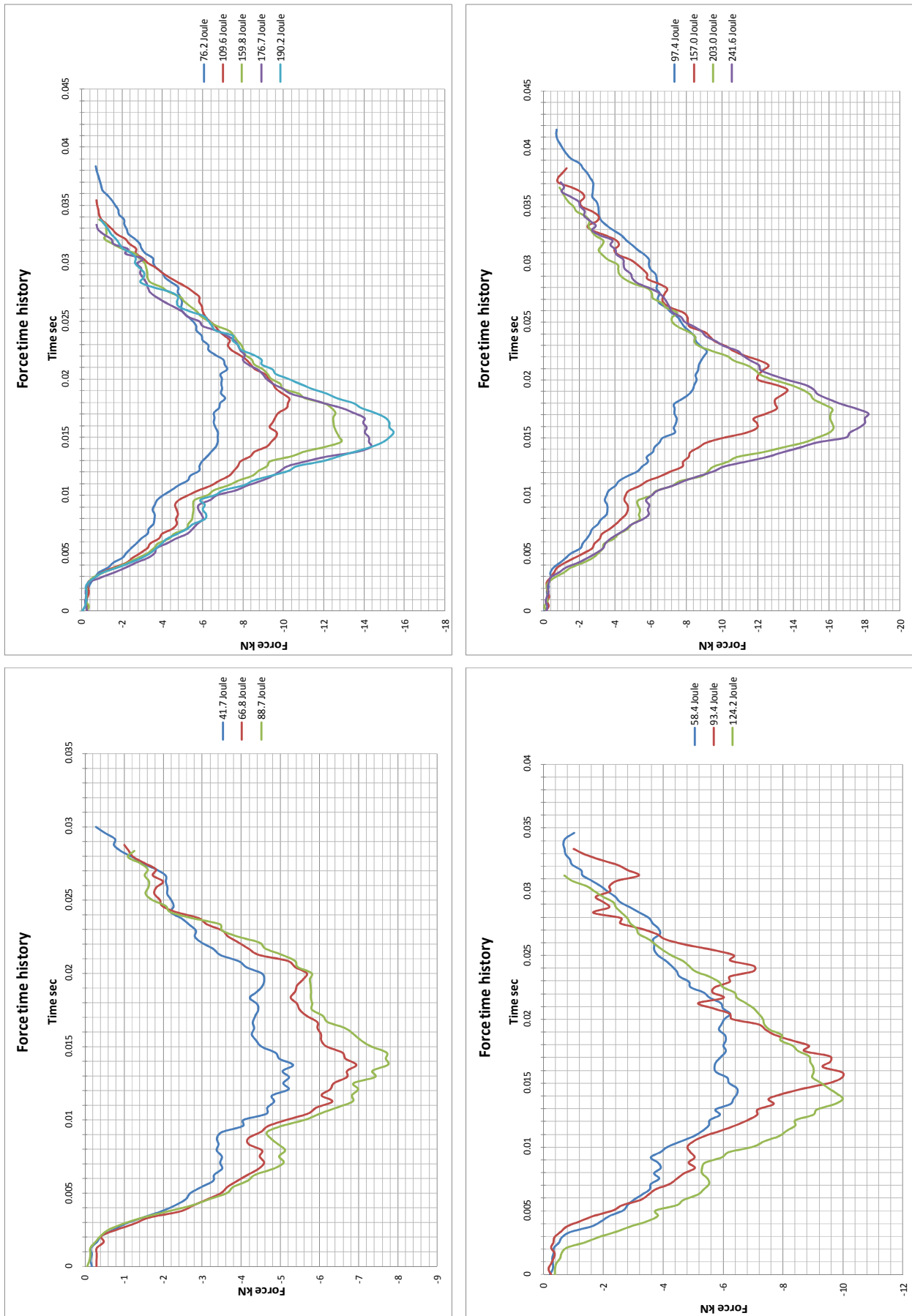

Figure 58 6.4 kg projectile force time history

Figure 59 Force time history: Clockwise from top left projectile 19.3 kg, 24.5 kg, 15 kg, 10.7 kg
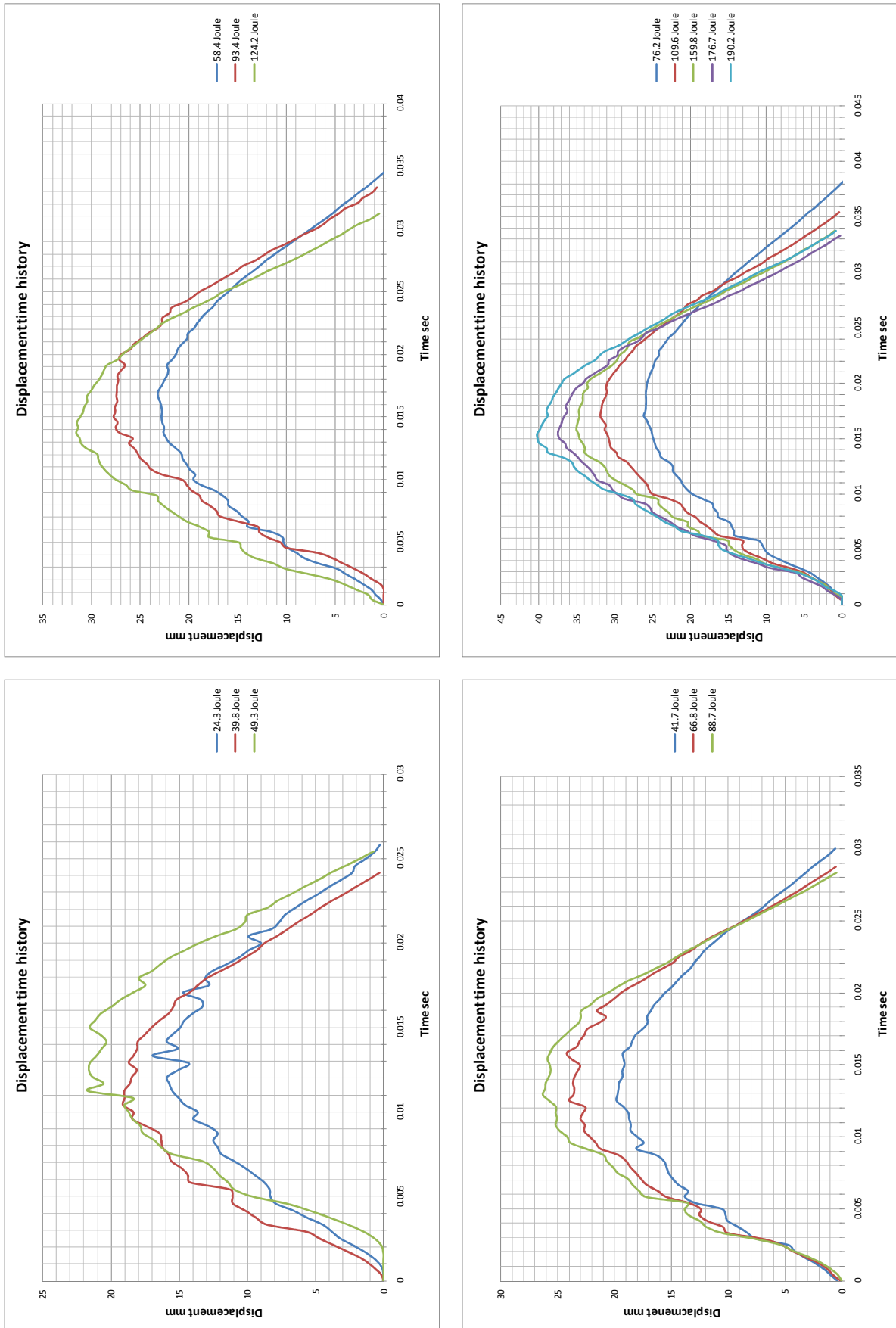
Figure 60 Displacement time history: Clockwise from top left projectile 15 kg, 19.3 kg, 10.7 kg, 6.4 kg
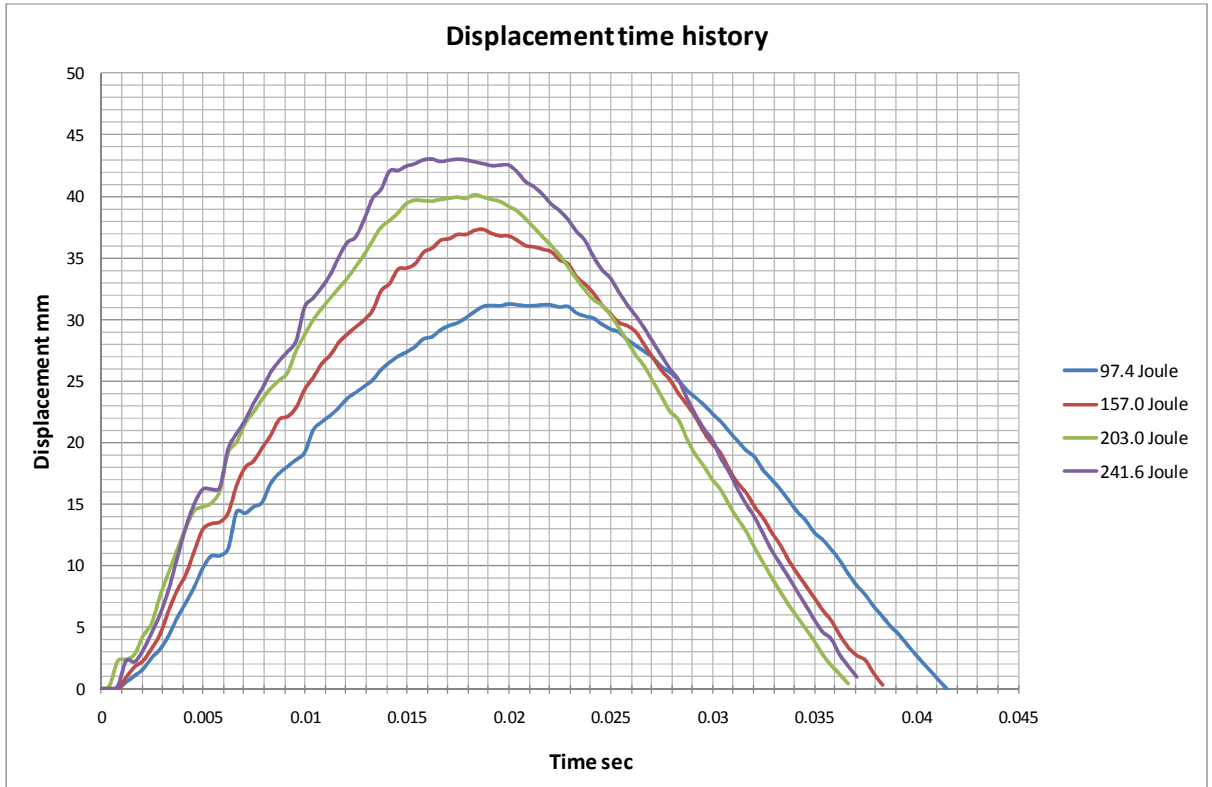
88

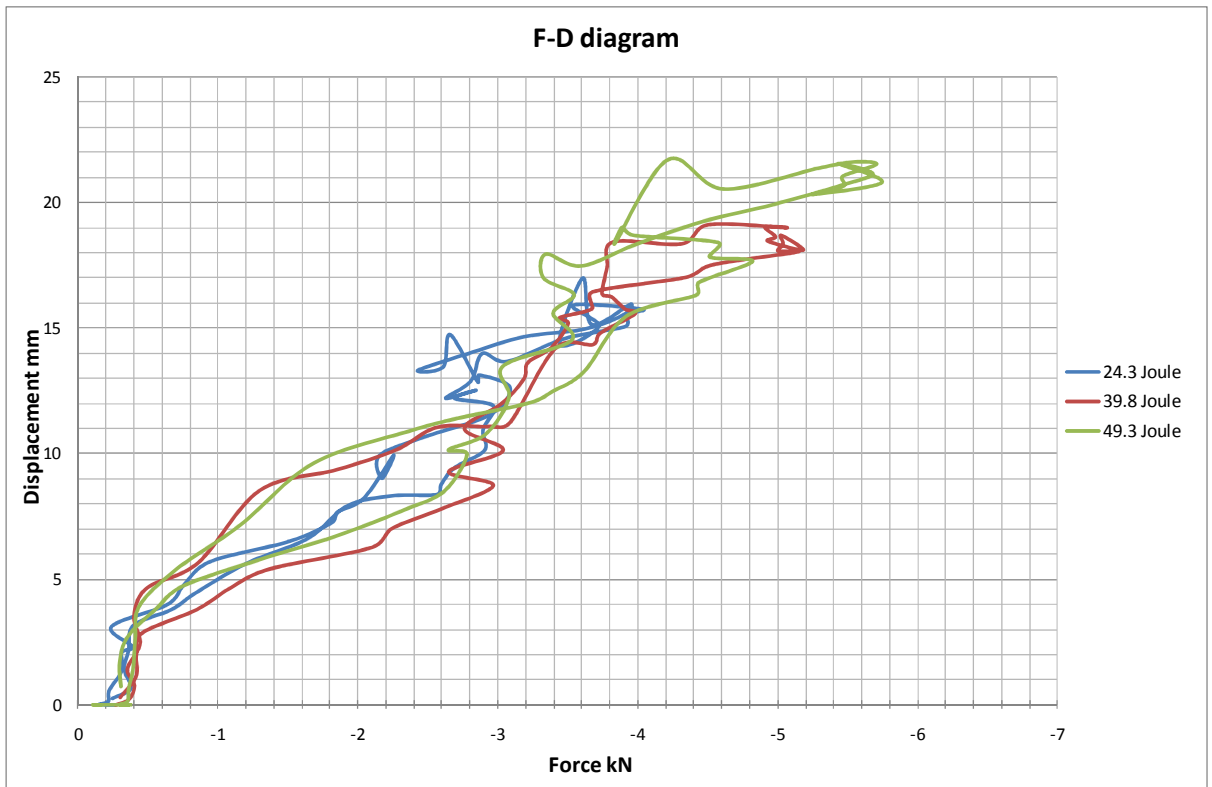Figure 61 Displacement time history projectile 24.5 kg
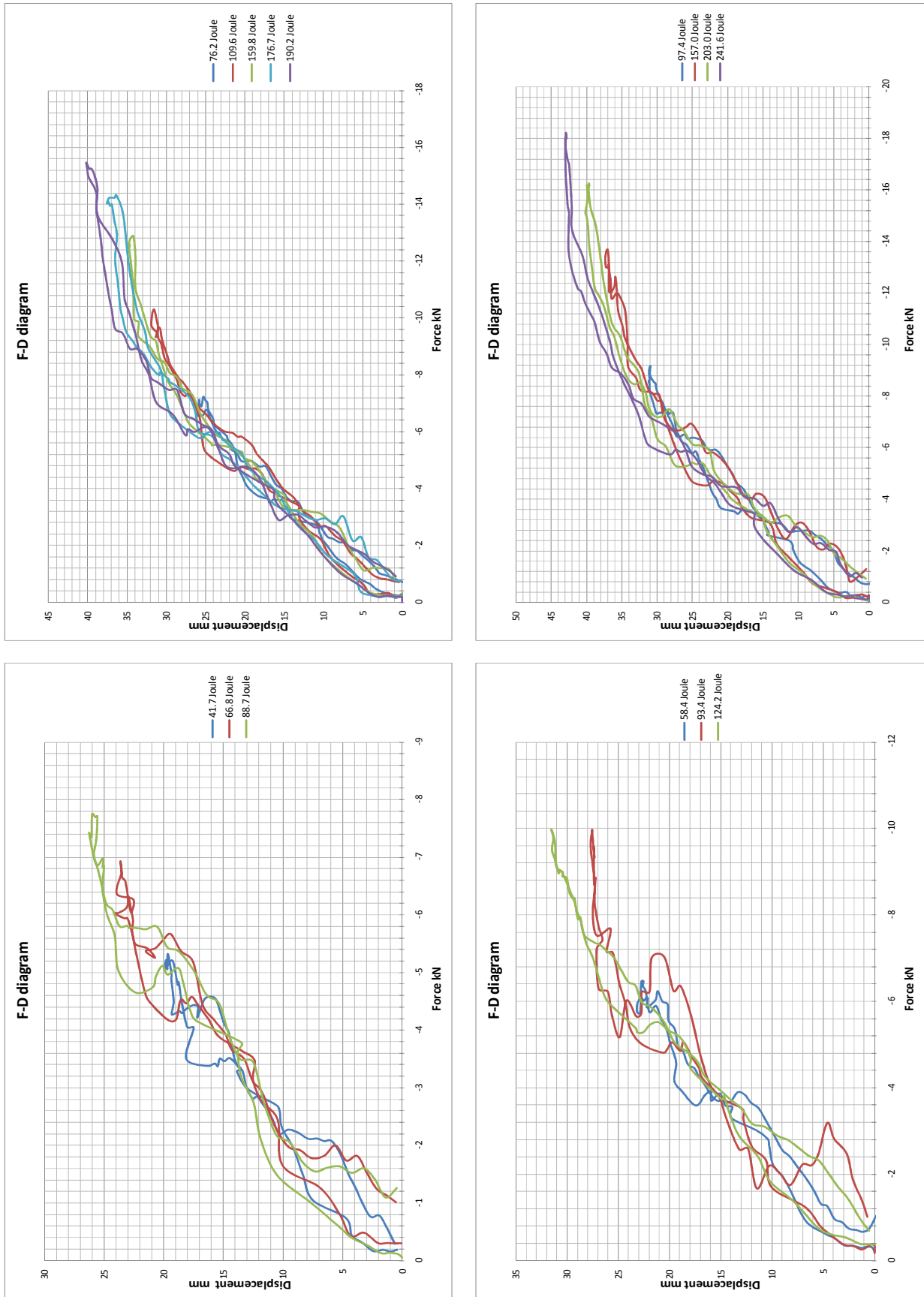

Figure 62 Force-Displacement graph projectile 6.4 kg

Figure 63 Force-Displacement graph clockwise top left projectile 19.3 kg, 24.5 kg, 15 kg, 10.7 kg

Appendix C. Cetex material data

TECHNICAL DATA

TenCate

TENCATE ADVANCED COMPOSITES USA, INC.

CETEX® PPS

PRODUCT TYPE

Polyphenylene Sulfide
Thermoplastic
Resin System

SERVICE TEMPERATURE

212°F (100°C) Continuous

TYPICAL APPLICATIONS

- Primary Aircraft Structures
- Secondary Aircraft Structures
- Engine Nacelles
- Radomes

PRODUCT DESCRIPTION

CETEX® PPS is a semicrystalline polyphenylene sulfide thermoplastic composite offering outstanding toughness and excellent chemical and solvent resistance. The material is inherently flame resistant with low smoke emission. It exceeds 35/35 OSU and is qualified at Airbus and Boeing for multiple structural applications. This material is typically supplied in 12ft by 4ft (3,660mm by 1,220mm) preconsolidated laminates using the customer's designated ply count and orientation. In addition, lightning strike material can be incorporated and the laminates can be textured. By utilizing preconsolidated sheets and avoiding hand lamination, the customer can significantly reduce the cycle time required to produce a finished part. In addition, thermoplastics have the unique capability of allowing parts to be welded, folded, etc., to facilitate lower part count structures.

TYPICAL PROPERTIES OF NEAT RESIN

Property	Value
Specific gravity	1.35 g/cc
Tg	194°F (90°C)
Melt temp	536°F (280°C)
Dielectric constant	3.20 at 1MHz
Loss tangent	0.0013 at 1MHz
Moisture absorption	0.02%
Flammability	V-0
Tensile strength	13.1ksi (90.3MPa)
Tensile modulus	0.551Msi (3,800MPa)
Elongation at yield	3%
Poisson's ratio	0.36
Compression strength	21.5ksi (148MPa)
Compression modulus	0.43Msi (2,965MPa)
Flexural strength	18.1ksi (125MPa)
Flexural modulus	0.54Msi (3,725MPa)
Izod unnotched	94.6ft-lb/in2 (199kJ/m2)
Izod notched	7.4ft-lb/in2 (15.6kJ/m2)
CTE	29ppm/°F (52.2ppm/°C)
Thermal conductivity	0.19 W/m-°K
Outgassing TML	0.04%
Outgassing CVCM	0.00%
WVR	0.00%
Fluid resistance	Excellent

18410 Butterfield Blvd.
Morgan Hill, CA 95037
USA

Tel 408 776 0700
Fax 408 776 0107
www.tencate.com

ISO 9001
AS 9100
Registered

TECHNICAL DATA

TenCate

TENCATE ADVANCED COMPOSITES USA, INC.

CETEX® PPS

Physical/Thermal (nominal values)	T300 3K 5HS/PPS with double sided Amcor foil				7781/PPS			
Mass of fabric	8.26	oz/yd²	280	g/m²	8.85	oz/yd²	300	g/m²
Mass of fabric + resin	14.33	oz/yd²	486	g/m²	14.01	oz/yd²	475	g/m²
Resin content by volume	50	%	50	%	47.5	%	47.5	%
Resin content by weight	43	%	43	%	37	%	37	%
Moisture pick up	0.1	%	0.1	%	0.1	%	0.1	%
Ply thickness	0.0122	in	0.31	mm	0.0098	in	0.25	mm
Specific gravity	96.7	lb/ft³	1.55	g/cm³	119.8	lb/ft³	1.92	g/cm³
Tg (DSC) (amorphous)	194	°F	90	°C	194	°F	90	°C
Tg (DSC) (crystalline)	248	°F	120	°C	248	°F	120	°C
Tm	536	°F	280	°C	536	°F	280	°C

Mechanical properties -67°F (-55°C) Dry

Tensile strength warp	114.5	ksi	790	MPa	65.6	ksi	453	MPa
Tensile strength weft	108.7	ksi	750	MPa	64.8	ksi	447	MPa
Tensile modulus warp	7.7	Msi	53	GPa	3.2	Msi	22	GPa
Tensile modulus weft	7.6	Msi	53	GPa	3.0	Msi	20	GPa
Compression strength warp	98.0	ksi	676	MPa	82.1	ksi	566	MPa
Compression strength weft	101.3	ksi	699	MPa	55.7	ksi	384	MPa
Compression modulus warp	7.2	Msi	49	GPa	3.8	Msi	27	GPa
Compression modulus weft	7.2	Msi	50	GPa	3.6	Msi	25	GPa
Flexural strength warp	151.3	ksi	1043	MPa				
Flexural strength weft	120.9	ksi	834	MPa				
Flexural modulus warp	8.6	Msi	59	GPa				
Flexural modulus weft	6.3	Msi	43	GPa				
In plane shear strength	19.0	ksi	131	MPa	15.8	ksi	109	MPa
In plane shear modulus	642.1	ksi	4428	MPa	711.5	ksi	4907	MPa
Open hole tensile strength	41.4	ksi	286	MPa				
Open hole compressive strength	39.5	ksi	273	MPa				
Compression after impact	32.3	ksi	223	MPa				
Bearing strength yield	71.2	ksi	491	MPa				
Bearing strength ultimate	121.5	ksi	838	MPa				

Mechanical properties -73°F (23°C)/50%RH

Tensile strength warp	109.8	ksi	758	MPa	49.3	ksi	340	MPa
Tensile strength weft	109.4	ksi	755	MPa	48.3	ksi	333	MPa
Tensile modulus warp	8.1	Msi	56	GPa	3.1	Msi	22	GPa
Tensile modulus weft	7.8	Msi	54	GPa	2.9	Msi	20	GPa
Compression strength warp	93.3	ksi	644	MPa	61.6	ksi	425	MPa
Compression strength weft	92.4	ksi	637	MPa	42.8	ksi	295	MPa
Compression modulus warp	7.5	Msi	51	GPa	3.7	Msi	26	GPa
Compression modulus weft	7.5	Msi	51	GPa	3.5	Msi	24	GPa
Flexural strength warp	148.9	ksi	1027	MPa	74.2	ksi	511	MPa
Flexural strength weft	120.5	ksi	831	MPa	56.6	ksi	390	MPa
Flexural modulus warp	8.7	Msi	60	GPa	3.3	Msi	23	GPa
Flexural modulus weft	6.5	Msi	45	GPa	2.9	Msi	20	GPa
In plane shear strength	17.2	ksi	119	MPa	11.6	ksi	80	MPa
In plane shear modulus	585.8	ksi	4040	MPa	538.5	ksi	3714	MPa
Open hole tensile strength	40.4	ksi	278	MPa	23.0	ksi	158	MPa
Open hole compressive strength	37.1	ksi	256	MPa	26.5	ksi	183	MPa
Compression after impact	31.2	ksi	215	MPa	24.8	ksi	171	MPa
Bearing strength yield	65.8	ksi	454	MPa	46.1	ksi	318	MPa
Bearing strength ultimate	122.4	ksi	844	MPa	74.8	ksi	516	MPa

18410 Butterfield Blvd.
Morgan Hill, CA 95037
USA

Tel   408 776 0700
Fax 408 776 0107
www.tencate.com

ISO 9001
AS 9100
Registered

TECHNICAL DATA

✕ TENCATE

TENCATE ADVANCED COMPOSITES USA, INC.

CETEX® PPS

Physical/Thermal (nominal values)	T300 3K 5HS/PPS with double sided Amcor foil				7781/PPS			
Mechanical Properties 80°C Dry								
Tensile strength warp	105.9	ksi	730	MPa	40.5	ksi	280	MPa
Tensile strength weft	93.6	ksi	646	MPa	40.7	ksi	281	MPa
Tensile modulus warp	8.2	Msi	57	GPa	2.9	Msi	20	GPa
Tensile modulus weft	7.6	Msi	53	GPa	2.7	Msi	19	GPa
Compression strength warp	80.9	ksi	558	MPa	43.0	ksi	297	MPa
Compression strength weft	76.3	ksi	526	MPa	29.4	ksi	203	MPa
Compression modulus warp	7.5	Msi	51	GPa	3.2	Msi	22	GPa
Compression modulus weft	7.4	Msi	51	GPa	2.9	Msi	20	GPa
Flexural strength warp	138.4	ksi	955	MPa				
Flexural strength weft	115.1	ksi	794	MPa				
Flexural modulus warp	8.4	Msi	58	GPa				
Flexural modulus weft	6.5	Msi	45	GPa				
In plane shear strength	15.7	ksi	108	MPa	8.6	ksi	60	MPa
In plane shear modulus	384.4	ksi	2651	MPa	247.3	ksi	1705	MPa

Mechanical properties 176°F (80°C) conditioned at 158°F (70°) and 85%RH

Tensile strength warp	109.6	ksi	756	MPa	41.9	ksi	289	MPa
Tensile strength weft	101.2	ksi	698	MPa	41.8	ksi	289	MPa
Tensile modulus warp	8.2	Msi	56	GPa	3.0	Msi	21	GPa
Tensile modulus weft	7.6	Msi	53	GPa	2.8	Msi	19	GPa
Compression strength warp	83.8	ksi	578	MPa	33.4	ksi	230	MPa
Compression strength weft	77.5	ksi	535	MPa	22.6	ksi	156	MPa
Compression modulus warp	7.5	Msi	52	GPa	3.1	Msi	22	GPa
Compression modulus weft	7.4	Msi	51	GPa	2.9	Msi	20	GPa
Flexural strength warp	141.7	ksi	977	MPa				
Flexural strength weft	107.2	ksi	739	MPa				
Flexural modulus warp	8.7	Msi	60	GPa				
Flexural modulus weft	6.4	Msi	44	GPa				
In plane shear strength	15.1	ksi	104	MPa	9.8	ksi	68	MPa
In plane shear modulus	434.7	ksi	2998	MPa	208.4	ksi	1437	MPa
Open hole tensile strength	39.1	ksi	270	MPa	19.6	ksi	135	MPa
Open hole compressive strength	33.7	ksi	232	MPa	16.0	ksi	110	MPa
Compression after impact	31.6	ksi	218	MPa	0.0	ksi		MPa
Bearing strength yield	59.9	ksi	413	MPa	26.7	ksi	184	MPa
Bearing strength ultimate	121.6	ksi	839	MPa	55.6	ksi	384	MPa

Mechanical properties 212°F (100°C) conditioned at 158°F (70°) and 85%RH

Tensile strength warp					35.7	ksi	246	MPa
Tensile strength weft					39.6	ksi	273	MPa
Tensile modulus warp					2.8	Msi	20	GPa
Tensile modulus weft					2.6	Msi	18	GPa
Compression strength warp					24.4	ksi	169	MPa
Compression strength weft					16.9	ksi	117	MPa
Compression modulus warp					2.9	Msi	20	GPa
Compression modulus weft					2.5	Msi	18	GPa
In plane shear strength					9.1	ksi	63	MPa
In plane shear modulus					109.0	ksi	752	MPa

Average results according to Mil-R-17; test methods vary

FLAMMABILITY PROPERTIES

	OSU		Flammability			SMOKE (4 min)		TOXICITY						
	Heat Release	Release Rate	Burn Length	After Flame	Drip Flame	Non-flaming	Flaming	HCN	CO	NOx	SO2	HF	HCl	HBr
5 plies of 7781/PEI	14	21	1.9 mm	0sec	N/D									
4 plies of 3k PW/PPS							9.03	9		1	17	1	1	

Flammability & Heat Release - FAR 25.853
Smoke Density & Toxicity - ATS 1000.001

All data given is based on representative samples of the materials in question. Since the method and circumstances under which these materials are processed and tested are key to their performance, and TenCate Advanced Composites USA, Inc. has no assurance of how its customers will use the material, the corporation cannot guarantee these properties. Rev Mar 2009

18410 Butterfield Blvd.
Morgan Hill, CA 95037
USA

Tel 408 776 0700
Fax 408 776 0107
www.tencate.com

ISO 9001
AS 9100
Registered

Appendix D. MAT_058 Parameters

Table 13 MAT_058 adjusted parameters

| Factor	Value	Motivation
RO	1550	Data sheet
EA	56 Gpa	Data sheet
EB	54 Gpa	Data sheet
PRBA	0.28	Data sheet
GAB	4.04 GPa	Data sheet
GBC	4.04 GPa	Data sheet
GCA	4.04 GPa	Data sheet
AOPT	-1	Local material coordinate system
ERODS	0.03	Data sheet
FS	1	Recommended for laminates
E11C	644 MPa	Data sheet
E11T	758 MPa	Data sheet
E22C	637 MPa	Data sheet
E22T	755 Mpa	Data sheet
SC	119 Mpa	Data sheet

Appendix E. Curved panel images
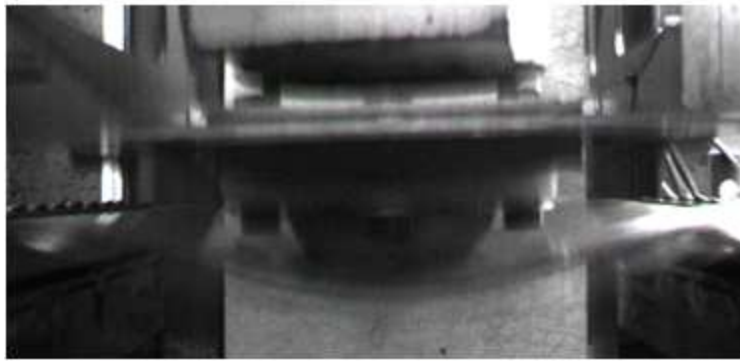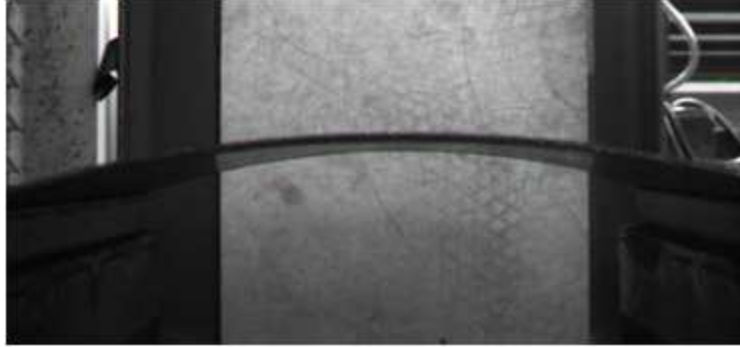
Figure 64 Snap through condition. Note excessive bending of laminate

Figure 65 Damage on curved laminate. Picture taken from the underside of the panel. Note damage at clamping region and delamination area as indicated.
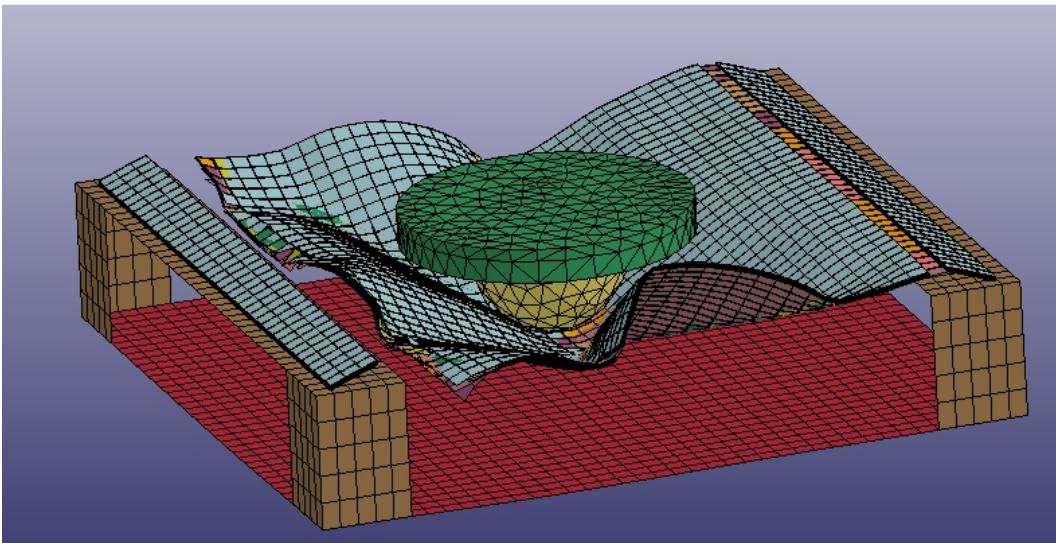
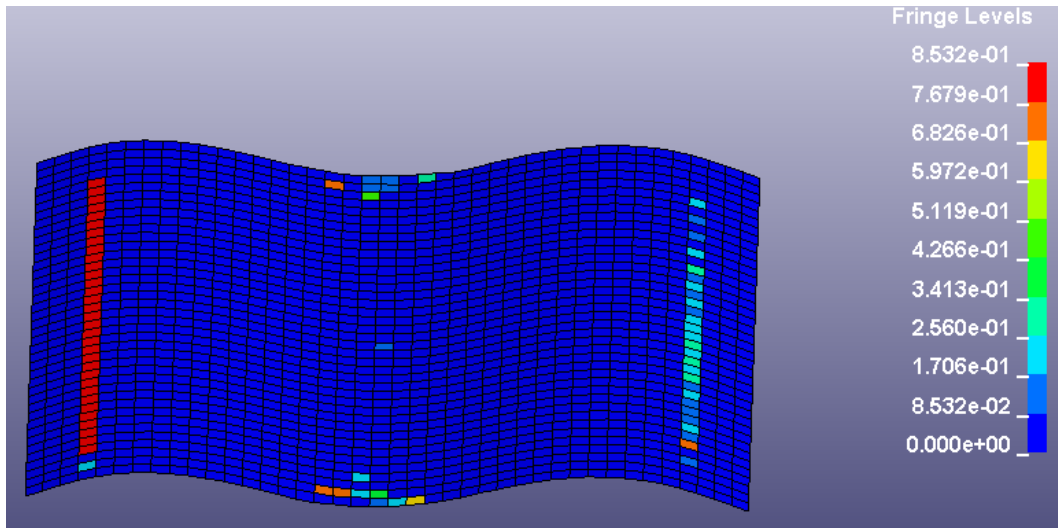

Figure 66 Catastrophic failure of the stacked shell model

Figure 67 Damage parameter ω_2 visualization for the resin model.
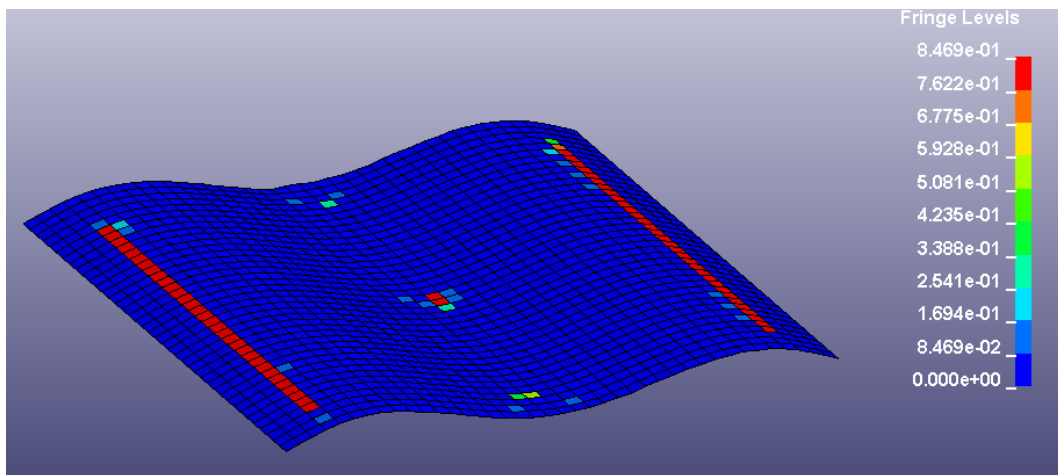

Figure 68 Damage parameter ω2 visualization for the single layer model. Note some fibre failure predicted in the central region.